

Recent advances in potentiometric Scanning Electrochemical Microscopy

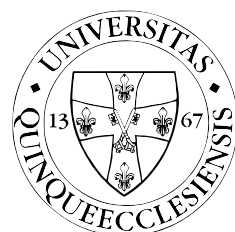
PhD Dissertation Draft

Author:
ANDRÁS KISS

Doctoral School of Chemistry
Department of General and Physical Chemistry

Doctoral Supervisor:
Prof. Dr. GÉZA NAGY
Department of General and Physical Chemistry

Head of Doctoral School:
Prof. Dr. FERENC KILÁR
Department of Analytical and Environmental Chemistry



University of Pécs

March 10, 2017

Contents

Preface	v
Acknowledgements	ix
Motivation	1
1 Introduction	4
2 Theory and principles	7
2.1 Microelectrodes	7
2.1.1 Pioneers of using microelectrodes	7
2.1.2 Glass-based electrodes and microelectrodes	10
2.1.3 Liquid ion exchanger membrane based microelectrodes	13
2.1.4 Ionophore based microelectrodes	14
2.1.5 Metal/metal-oxide pH microelectrodes	17
2.1.6 The potentiometric measurement	17
2.1.7 Response characteristics	20
2.1.8 On the use of the expression „equilibrium”	23
2.2 Scanning Electrochemical Microscopy	24
2.2.1 Origins of the technique	24
2.2.2 Potentiometric SECM	26
2.2.3 Distortion and image processing in SECM	27
3 Materials and Methods	29
3.1 Ion-selective microelectrodes	29
3.1.1 Preparation of the microelectrodes	29
3.1.1.1 Metal/metal-oxide electrodes	29
Antimony pH-sensitive microelectrode	29
Antimony pH-sensitive combined macroelectrode	30
Tungsten pH-sensitive microelectrode	30

3.1.1.2	Micropipette ion-selective electrodes	31
	Liquid-contact ion-selective microelectrodes	33
	Solid-contact ion-selective microelectrodes	33
	Preparation of the solid contact	33
3.1.2	Instrumentation for the microelectrodes	35
3.1.2.1	Home-made, Arduino based DAQ	36
3.1.3	Characterization of the microelectrodes	39
3.1.3.1	Calibration	39
3.1.3.2	Internal resistance	39
3.1.3.3	Response time	40
3.1.3.4	RC time constant	41
3.2	SECM targets	42
3.2.1	Magnesium- and potassium-ion source pipette model targets .	42
3.2.2	Moulded model targets	42
3.2.2.1	Iron – magnesium galvanic couple	44
3.2.2.2	Iron – AZ63 galvanic couple	45
3.2.2.3	Carbon steel	45
3.2.2.4	Graphite model target	45
3.3	SECM routines	46
3.3.1	For the comparison of solid and liquid contact microelectrodes	46
3.3.2	Optimization of scanning patterns and algorithms	46
3.3.2.1	Cartesian coordinate-system based patterns and al- gorithms	46
3.3.2.2	Circular, polar-coordinate system based patterns and algorithms	46
3.3.3	SECM routines for the deconvolution study	48
3.3.3.1	Linescans	48
3.3.3.2	2D scans	48
3.3.4	Backlash compensation	49
3.4	Deconvolution of potentiometric SECM images	49
3.5	Simulation of the SECM measurements	52
3.5.1	3D numerical simulation of diffusion from a disk source . . .	52
3.5.2	SECM scan simulation	53
3.6	Scanning Electrochemical Microscope	53
3.6.1	Homemade SECM	53
3.7	Measuring corrosion current between a galvanic couple	55
3.8	Estimating ion-flux based on approaching curves	55

4 Results and Discussion	57
4.1 Using solid-contact electrodes as potentiometric SECM probes	59
4.1.1 Electrode characterization and SECM images of a model system	59
4.1.2 Applications	61
4.1.2.1 Investigation of galvanic and homogeneous corrosion of magnesium	61
4.1.2.2 Estimation of corrosion current based on vertical SECM scans	62
4.2 Optimization of scanning algorithms	66
4.2.1 SECM simulations	66
4.2.2 Experimental SECM images	66
4.3 Signal processing in potentiometric SECM	70
4.3.1 Deconvolution of measurements performed with metal/metal- oxide microelectrodes	70
4.3.1.1 Minimal working example: deconvolution of a step response	71
4.3.1.2 Investigation of possible surface processes	74
4.3.1.3 Linescans with the antimony microelectrode	76
4.3.1.4 2D scans with the antimony microelectrode	77
4.3.1.5 2D scans with the tungsten microelectrodes	77
4.3.2 Experiments with ion-selective micropipettes	79
4.3.2.1 Linescans with a magnesium ion-selective micropipette Measuring R and C	79
Linescans	80
4.3.2.2 2D scans with the magnesium ion-selective micropipette	81
4.3.2.3 2D scans with the potassium ion-selective micropipette	81
4.3.3 Application: investigation of the corrosion of carbon steel . . .	81
4.3.4 Possibility of „blind deconvolution”	84
4.4 The effect of electric field on potentiometric SECM images	88
5 Conclusions	93
List of Figures	95
List of Tables	97
List of Abbreviations	99

Appendix	112
5.1 Diffusion and SECM scan simulation	112
5.2 Deconvolution program in Fortran	118

Preface

The work presented here was performed mainly at the *Department of General and Physical Chemistry* in the *Doctoral School of Chemistry* at the *University of Pécs*, during the years 2011-2016, under the supervision of Professor Géza Nagy. Some of the work was done at the *Department of Physical Chemistry* of the *La Laguna University* in Tenerife, Spain, under the joint supervision of Professor Géza Nagy, and Professor Ricardo M. Souto. This thesis is based almost entirely on the following publications, which are referred to in the text by their Roman numerals.

I. András Kiss, Ricardo M. Souto, Géza Nagy

Investigation of Mg/Al alloy sacrificial anode corrosion with Scanning Electrochemical Microscopy

Periodica Polytechnica Chemical Engineering 57, no. 1-2 (2013): 11-14.

IF.: 0.30, cited by: 2

II. Javier Izquierdo, András Kiss, Juan José Santana, Lívia Nagy, István Bitter, Hugh S. Isaacs, Géza Nagy, Ricardo M. Souto

Development of Mg^{2+} ion-selective microelectrodes for potentiometric scanning electrochemical microscopy monitoring of galvanic corrosion processes

Journal of The Electrochemical Society 160, no. 9 (2013): C451-C459.

IF.: 3.27, cited by: 14

III. Ricardo M. Souto, András Kiss, Javier Izquierdo, Lívia Nagy, István Bitter, Géza Nagy

Spatially-resolved imaging of concentration distributions on corroding magnesium-based materials exposed to aqueous environments by SECM

Electrochemistry Communications 26 (2013): 25-28.

IF.: 4.85, cited by: 20

IV. András Kiss, Géza Nagy

New SECM scanning algorithms for improved potentiometric imaging of circularly symmetric targets

Electrochimica Acta 119 (2014): 169-174.

IF.: 4.50, cited by: 5

V. András Kiss, Géza Nagy

Deconvolution in Potentiometric SECM

Electroanalysis 27, no. 3 (2015): 587-590.

IF.: 2.14, cited by: 1

VI. András Kiss, Géza Nagy

Deconvolution of potentiometric SECM images recorded with high scan rate

Electrochimica Acta 163 (2015): 303-309.

IF.: 4.50, cited by: 3

Contribution statement

Publications **I**, and **IV-VI** are entirely my own work, done under the guidance of my doctoral supervisor, Professor Géza Nagy, in Pécs, at the Department of General and Physical Chemistry of the University of Pécs. Publications **II** and **III** are mostly my work. The work published therein was done at the University of La Laguna, Tenerife, under the supervision of Professor Ricardo M. Souto and Professor Géza Nagy. In **II** and **III**, I prepared the electrodes, did the electrode characterization and the majority of the SECM scans.

Not included in the thesis

- (a) Zsuzsanna Őri, **András Kiss**, Anton Alexandru Ciucu, Constantin Mihailciuc, Cristian Dragos Stefanescu, Livia Nagy, Géza Nagy

Sensitivity enhancement of a „bananatrode” biosensor for dopamine based on SECM studies inside its reaction layer

IF.: 4.10, cited by: 4

Sensors and Actuators B: Chemical 190 (2014): 149-156.

- (b) Javier Izquierdo, Bibiana M Fernández-Pérez, Dániel Filotás, Zsuzsanna Őri, **András Kiss**, Romen T Martín-Gómez, Lívia Nagy, Géza Nagy, Ricardo M Souto

Imaging of Concentration Distributions and Hydrogen Evolution on Corroding Magnesium Exposed to Aqueous Environments Using Scanning Electrochemical Microscopy

IF.: 2.471

Electroanalysis (2016).

- (c) A. El Jaouhari, Dániel Filótás, **András Kiss**, M. Laabd, E. A. Bazzaoui, Lívia Nagy, Géza Nagy, A. Albourine, J. I. Martins, R. Wang

SECM investigation of electrochemically synthesized polypyrrole from aqueous medium

IF.: 2.223

Journal of Applied Electrochemistry, (2016).

Published prior PhD

András Kiss, László Kiss, Barna Kovács, Géza Nagy

Air Gap Microcell for Scanning Electrochemical Microscopic Imaging of Carbon Dioxide Output. Model Calculation and Gas Phase SECM Measurements for Estimation of Carbon Dioxide Producing Activity of Microbial Sources

Electroanalysis 23, no. 10 (2011): 2320-2326.

IF.: 2.14, cited by: 1

Published in non-refereed journal

Lívia Nagy, Gergely Gyevai, **András Kiss**, Ricardo Souto, Javier Izquierdo, Géza Nagy

Speciális célra szolgáló mikroelektródok kifejlesztése és alkalmazása

Magyar Kémiai Folyóirat 119, 2-3. (2013): 104-109.

Book chapter

Ricardo M. Souto, Javier Izquierdo, Juan J. Santana, **András Kiss**, Lívia Nagy, Géza Nagy

Progress in Scanning Electrochemical Microscopy by coupling Potentiometric and Amperometric Measurement Modes

Current Microscopy Contributions to Advances in Science and Technology (A. Méndez-Vilas, Ed.), Formatex, (2012): 1407-1415.

Presentations

Posters

Acknowledgements

I wish to express my sincere gratitude to Professor Géza Nagy for introducing me to the fascinating field of electrochemistry, and for the continuous support and guidance during the work.

I am truly grateful to Barna Kovács for the enlightening discussions about micro-electrode electronics. I am grateful to Lívia Nagy for the help received during the years of my PhD studies.

Many thanks are due to all my colleagues and friends with whom I have worked during my years as an undergraduate and doctoral student.

I am thankful to Professor Johan Bobacka, Ricardo M. Souto, Frank-Michael Matysik, Petr Skládal and Mohammed Bazzaoui for welcoming me in their laboratories.

I am also thankful to all the anonymous referees who gave meaningful feedback about my work as part of the peer review process.

Pécs, May, 2016.

András Kiss

Motivation

I started my doctoral studies at the Department of General and Physical Chemistry at the University of Pécs in 2011 under the supervision of Professor Géza Nagy. By that time, I've already spent 3 years there as an undergraduate student, culminating in my MSc thesis, which I successfully defended in 2011. The original title of my PhD research was „*Application of potentiometric microelectrodes in Scanning Electrochemical Microscopy to study the corrosion of magnesium and its alloys*”. I started the work with great enthusiasm, but soon discovered, that the potentiometric SECM had one major limitation which prevented me from pursuing my studies in corrosion science. The method was too slow to complete a relevant portion of scan before the system has completely changed. Corrosion is highly localized, and the location and size of the anodic and cathodic spots are quick to change. On the other hand, when one increases scanning speed, the image becomes distorted. This is because the time allowed for the potentiometric cell to reach equilibrium potential is getting closer to RC, the time constant of the cell, or more specifically $4 \times RC$, which is the least amount of time necessary to reach equilibrium potential to a reasonable extent. In order to use SECM more effectively in corrosion studies, one has to speed up the method, *and* lower, or at least not increase imaging distortion.

Efforts have already been made at the Department of General and Physical Chemistry to lower the resistance of the electrodes used as SECM measuring probes. By using novel solid contact instead of the conventional liquid contact as interface between the metallic conductor and the ion selective cocktail, resistance, and therefore the RC time constant could be decreased by a factor of ten. Building on the new electrodes, several papers have been published about successful research collaborations with neurophysiologists, botanists, and in particular, corrosion scientists.

I joined the research in the hopes of a worthwhile contribution to the technique of potentiometric SECM, which eventually might lead to new possibilities in corrosion science and other areas. My PhD research was slowly turning into a methodological study, exploring ideas to improve the technique.

In 2012 I was lucky enough to be able to participate in the biggest conference of „SECM and related techniques” held annually, which in 2012, was held in Ein

Gedi, Israel. I've realized, that other research groups are also struggling with the difficulties of potentiometric SECM, and the problem is not limited to corrosion science. In fact, most of the studies are done in amperometric mode, which, based on discussions with participants, might be exactly due to these difficulties. Also in 2012 I was able to spend a month at the Department of Physical Chemistry of the La Laguna University in Tenerife under the supervision of Professor Ricardo M. Souto. We used the very same solid contact magnesium-ion selective electrodes I prepared in Pécs to map magnesium-ion concentration above corroding magnesium and magnesium alloy samples. They worked unexpectedly well, and we were able to take high-speed, low distortion images of the samples for the first time. We published the results. I was very happy with the two papers done in cooperation between our research groups, and the methodological aspect of them fitted nicely in my research topic.

When I returned home, I immediately started working on a new idea I had when I was in Tenerife. Since the majority of the targets in SECM studies are, or can be made circular, it makes sense to use a scanning pattern based on the polar coordinate system instead of the conventional 2D raster based on the Cartesian coordinate system. With new scanning patterns and algorithms, I managed to further decrease distortion and increase scanning speed at the same time.

While working on the final touches of the paper about the new scanning algorithms, I had another idea. The transient response of the potentiometric cell due to concentration changes is described by a relatively simple function. It's not necessary to wait $4 \times RC$ to find out the equilibrium potential at a given sampling point. From the initial potential, and the potential at time t , it's possible to calculate it. One has to know the response characteristics of the cell, but that can be easily measured. I managed to increase scanning speed even further. My PhD thesis is about these three improvements to the potentiometric SECM.

In May 2016, I was lucky enough to be invited to the Analytica 2016 conference in München, by Professor Frank-Michael Matysik. I presented my work, and got precious feedback from the audience, including two of the most prominent researchers working in the field; Professors Michael Mirkin and Eric Bakker. The discussions with them shed some light on a few issues I faced writing my thesis. Unfortunately however, I couldn't perform additional experiments based on the advices I received, since I planned to submit my thesis only a few days later.

The author hopes that he managed to contribute to the field of Scanning Electrochemical Microscopy with this thesis. Please forgive the rather lengthy discussion about the role of biologists in the development of microelectrodes, but the author graduated as a biologist himself, and takes pride in the achievements of the early

pioneers of electroneurophysiology.

Chapter 1

Introduction

Since the invention of Scanning Tunnelling Microscopy (STM) in 1981 by Binnig and Rohrer, surface analysis has seen tremendous growth. As an indication of the importance of their pioneering work, they received the Nobel Prize in 1986, only five years later. STM was but the first of a family of techniques, called Scanning Probe Microscopy (SPM), with many more to come in the following years. Their basic element is a local experiment, which is repeated sequentially at the pre-defined points of a raster grid. The most important advantage of them over the conventional optical microscopy is their incredible resolution. Even individual atoms can be „seen”, because they are not limited by Abbes’ formula. Modifications of the original STM followed quickly. Atomic Force Microscopy was invented in 1982 by the same researchers.

In 1989, not long after the introduction of the STM, electrochemists invented the Scanning Electrochemical Microscope (SECM), the electrochemical version of SPM. It is based on the same concept, except the scanning probe is a microelectrode. With this technique, highly resolved chemical information can be gathered about a wide range of surfaces. One of the biggest disadvantages of the SPM techniques in general is their low speed, due to the scanning process. The entire image is recorded with the same measuring tip, as opposed to optical techniques, where there is usually a sensor matrix. As a consequence of this, the more data points are in an image, the longer it will take to record it. This is especially a problem in the potentiometric operation mode of the SECM. The response time of the measuring cell is determined by the RC time constant, which in turn, depends mainly on the resistance of the measuring microelectrode. Due to the small size of the microelectrodes, their resistance can even reach the $G\Omega$ range, resulting in imaging times that can be measured in minutes.

Other SPM techniques have received significant improvement during the last few decades, and their imaging speed can even reach video rates. Low speed, however, is an often overlooked limitation of the SECM, and prevents the quick recording of

highly resolved images. That is, one has to choose between high resolution and quick imaging. The image will either be quickly completed but distorted, or high quality but hard to evaluate, because the points of the image will not only have different spatial, but different temporal coordinates as well.

My thesis is mostly devoted to the investigation of this problem, and three possible solutions to it:

1. Use of novel, low-resistance solid contact electrodes instead of conventional ones. Based on publications [I-III](#).
2. Optimization of scanning patterns and algorithms. Based on publication [IV](#).
3. Deconvolution of distorted potentiometric SECM images recorded with high scanrate. Based on publications [V-VI](#).

The first approach I took is to lower the resistance of the measuring microelectrode. By using a conducting polymer based solid internal contact instead of the conventional liquid contact, electrode resistance, therefore RC time-constant of the entire potentiometric circuit can be decreased. Conducting polymers have been used in macroelectrodes before, but never where it is crucial to have a small resistance despite the small probe diameter: SECM investigation of corroding surfaces.

The second approach is to optimize scanning patterns. Many studied systems have a certain symmetry which can be exploited to achieve lower distortion. I chose a simple, yet very common symmetry, the radial symmetry, and came up with optimized scanning patterns and algorithms.

The third technique is image processing. The relationship between cell potential difference and time is relatively simple, and by measuring some basic parameters of the microelectrode and the potentiometric cell, a deconvolution function can be obtained. With this, the equilibrium potential can be calculated for each data acquisition point of the raster grid, and distortion can be removed from the image.

To test out these techniques, I've used simple model systems, then, I've applied them in corrosion studies as an example where they can be useful. During collaborations with colleagues, I used these techniques on several occasions, and I've included some of those results in my thesis.

Additionally, I investigated the undesired effect of electric field generated in certain SECM experiments. In some cases, where there is a potential difference between two points in the electrolyte, a relatively strong electric field can be formed. For instance during galvanic corrosion there is a large potential difference between the surfaces of the metals constituting the galvanic couple. The local electric field at the tip of the measuring electrode might influence the measured potential. I investigated

this contribution to the measured value, and tried to isolate the effect of the electric field.

Chapter 2

Theory and principles

2.1 Microelectrodes

2.1.1 Pioneers of using microelectrodes

In this section I look at the motivation behind electrode miniaturization, and the difficulties the researchers encountered during the early development of microelectrodes. By decreasing electrode diameter, new challenges had to be faced. The problem associated with these challenges always lead to a compromise between several competing desired properties, which can never truly be solved, only alleviated to a certain point, to make a particular study possible. Researchers that first used microelectrodes faced the same problems as todays researchers, the difference lies in the severity of the compromise. The fundamental problem of potentiometry with microelectrodes hasn't changed. Therefore, I reviewed the literature going back to the first appearances of such electrodes in an effort to better understand the reasons and potential solutions of some of the problems in microelectrode potentiometry.

For the first few decades, the development of microelectrodes was related closely, almost exclusively to neurophysiology. The main merit of the work of the early pioneers from the standpoint of the electrochemist, is the foundation of the micropipette techniques, including the preparation, instrumentation, and basic characterization of micropipette electrodes.

First efforts to miniaturize electrodes originally were made by biologists, electrophysiologists in particular. Microelectrodes were necessary to carry out experiments at the cellular level on single neurons. Even though the largest possible neuron cells (*Loligo forbesii* or veined squid, *Architeuthis spp.* or giant squid) were used in the early days of neurophysiology, the electrodes of those days in the early 1930's weren't small enough for single cell experiments. This initiated the miniaturization of electrodes. The first successful experiments were done by the famous

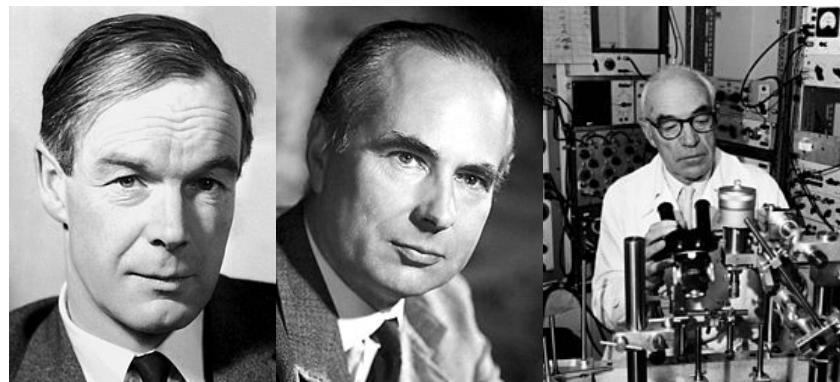


Figure 2.1: *Sir Alan LLOYD Hodgkin, Sir Andrew Huxley and Sir John Eccles*, the pioneers of electrophysiology, first to use microelectrodes.

pioneers of the field, *Sir Alan LLOYD Hodgkin, Sir Andrew Huxley and Sir John Eccles* (Fig. 2.1), who were awarded the Nobel Prize in Physiology and Medicine „*for their discoveries concerning the ionic mechanisms involved in excitation and inhibition in the peripheral and central portions of the nerve cell membrane*”, in 1963.

They have found that the best subject for electroneurophysiological studies is the giant squid axon. The large diameter of the axon provided a great experimental advantage for Hodgkin and Huxley as it allowed them to insert voltage clamp electrodes inside the lumen of the axon. But as Graham and Gerard writes [1]:

„*The giant fiber, up to a millimeter in diameter is admirable for internal exploration with a microelectrode, since this can be inserted longitudinally and the tip pushed far from the region of penetration and damage. These fibers are available, however, only at restricted seasons and localities and after painstaking preparation.*”

Interestingly, the Second World War might have accelerated the miniaturization of the microelectrodes, because it restricted the availability of the giant squid. Webb and Young wrote in their 1940 paper [2]:

„*Unfortunately the work was terminated by the outbreak of war, which rendered the capture of further squids impossible, so that the number of fibres dealt with is much smaller than might have been wished.*”

Another species, the much more accessible longfin inshore squid (*Loligo paelii*) had to be used, which has much smaller axons. In order to carry out voltage clamp

experiments on neurons of this species, the intracellular microelectrodes had to be miniaturized further.

The basic experimental setup for an early neurophysiological study employed several electrodes. Usually, there was an intracellular and an extracellular electrode to measure the potential difference across the cell membrane. This technique has been used to measure the resting potential in the axon of the squid [3, 4]. A microelectrode consisting of a long glass capillary was inserted at one end of the fibre and was pushed in for a distance of 10-30 mm. Great care had to be taken at this step to avoid damaging the cell membrane. The small size of most nerve and muscle fibres made it difficult to use this technique. The breakthrough came when Graham and Gerard showed that a very small electrode can be inserted transversely into a muscle fiber without causing damage or twitch [1, 5]. In order to obtain successful results, the microelectrodes should have had an external diameter of less than 0.5 μm . This small diameter however introduced additional difficulties caused by the high resistance of such electrodes. From that point on, the further development of microelectrodes depended on the development of the recording apparatus. At that time, the state of the art amplifiers were of valve types. A few years later, advances in electronics and the technique in general made it possible to record both action, and resting potentials with these kind of electrodes [6, 7].

In 1950, Ling and Gerard published their findings in *Nature* about the dependence of resting membrane potential on external potassium ion concentration [8]. The resulting plot resembled the calibration plots of ion-selective electrodes that will come a few years later.

The next big advancement in the development of microelectrodes was the introduction of the so-called *patch-clamp* technique by *Erwin Neher* and *Bert Sakmann* [9, 10]. They received their Nobel Prize in 1991 „*for their discoveries concerning the function of single ion channels in cells*”, also in Physiology and Medicine. With this technique, the function of single ion channels was possible to observe. The problem that had to be solved in order to be able to conduct these experiments was the large background noise. Eher and Sakmann wrote in their original Nature paper [9]:

„*Clearly, it would be of great interest to refine techniques of conductance measurement in order to resolve discrete changes in conductance which are expected to occur when single channels open or close. This has not been possible so far because of excessive extraneous background noise.*”

Their solution was to limit the membrane area from which current is measured to

a small patch, and thereby decrease background membrane noise. This was achieved by applying closely the tip of a glass micropipette, 3 – 5 μm in diameter, on to the muscle surface, thus isolating electrically a small patch of membrane. With this technique, the two conductive states of a single ion channel – closed and open – were possible to distinguish. Eher and Sakmann were able to reveal discrete changes in conductance of the ion-channel associated with the acetylcholine receptor in the neuromuscular junction, that show many of the features that have been postulated for single ion-channels.

2.1.2 Glass-based electrodes and microelectrodes

Analytical potentiometry started with the discovery and development of the glass pH-electrode. It is the best electrochemical sensor, and one of the best sensor ever made, with a linear response over more than 13 orders of magnitude, and excellent selectivity. Because of its importance, and because pH measurement is used throughout the work described in this thesis, the basic concepts of pH measurement will be introduced through the example of the glass electrode.

It was in 1906, when a botanist named Max Cremer discovered that the potential difference across a thin glass membrane is a function of pH when opposite sides of the membrane are in contact with solutions containing different concentrations of H_3O^+ [11, 12]. Three years later, in 1909, Sørensen introduced the concept of pH [13]. He defined it as the negative logarithm of the concentration of H_3O^+ :

$$\text{pH} = -\lg c_{\text{H}_3\text{O}^+} \quad (2.1)$$

This however, is not entirely true, because pH depends on the *activity* of H_3O^+ , rather than its concentration:

$$\text{pH} = -\lg a_{\text{H}_3\text{O}^+} \quad (2.2)$$

And since pH is dimensionless, a better way to define pH is:

$$\text{pH} = -\lg(\gamma_{\text{H}_3\text{O}^+} m_{\text{H}_3\text{O}^+} / m^\theta) \quad (2.3)$$

or

$$\text{pH} = -\lg(\gamma_{\text{H}_3\text{O}^+} c_{\text{H}_3\text{O}^+} / c^\theta) \quad (2.4)$$

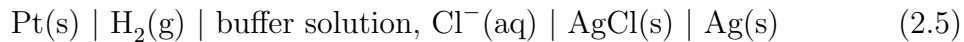
where $m^\theta = 1 \text{ mol}\cdot\text{kg}^{-1}$ and $c^\theta = 1 \text{ mol}\cdot\text{dm}^{-3}$ are the standard states, and $\gamma_{\text{H}_3\text{O}^+}$ is the activity coefficient of H_3O^+ .



Figure 2.2: The Gold Standard of pH measurement, the Harned cell (at the Danish National Metrology Institute).

The current, internationally accepted definition of pH is an instrumental definition, based on an electrochemical cell without transference using the hydrogen gas electrode, known as the *Harned Cell* [14] (Fig. 2.2). To measure the pH in such a cell, a conventional procedure was developed at NBS (National Bureau of Standards) [15] and recommended at present by the last IUPAC (International Union of Pure and Applied Chemistry) Recommendations [16]. NIST (National Institute of Standards and Technology) in the U.S. and PTB (Physikalisch-Technische Bundesanstalt) in Germany have presented pH values using the Harned Cell.

pH measurement using the Harned Cell is carried out by measuring the potential difference of the following cell, containing certified standard buffer solution and chloride ions, added in order to use the silver/silver-chloride electrode:



To calculate the potential of any half-cell, the *Nernst-equation* can be used:

$$E = E^\theta - \frac{RT}{z_i F} \ln a_i \quad (2.6)$$

where E^θ is the standard potential difference of the cell, R the universal gas constant, F the Faraday constant, T the thermodynamic temperature, z_i is the valence and a_i is the activity of ion species i . The potential difference E of the

cell 2.5 (corrected to 101.325 kPa partial pressure of hydrogen) is described by the *Nernst-equation* as:

$$E = E^\theta - \frac{RT \ln 10}{F} \lg \left(\frac{a_{\text{H}_3\text{O}^+} m_{\text{Cl}^-} \gamma_{\text{Cl}^-}}{m^\theta} \right) \quad (2.7)$$

which can be rearranged to give the pH:

$$\text{p}(a_{\text{H}_3\text{O}^+} \gamma_{\text{Cl}^-}) = -\lg(a_{\text{H}_3\text{O}^+} \gamma_{\text{Cl}^-}) = \frac{E - E^\theta}{(RT/F) \ln 10} + \lg \left(\frac{m_{\text{Cl}^-}}{m^\theta} \right) \quad (2.8)$$

where γ_{Cl^-} is the molal activity coefficient of the chloride ions at the molality m_{Cl^-} .

The acidity function value at zero chloride molality $\text{p}a_0 = -\lg(a_{\text{H}^+} \gamma_{\text{Cl}^-}) m_{\text{Cl}^- \rightarrow 0}$ is determined by linear extrapolation of the acidity function values obtained by fitting by least square method. Calculation of trace activity coefficient of chloride ions $\gamma_{\text{Cl}^- \rightarrow 0}$ at $m_{\text{Cl}^- \rightarrow 0}$ according to the Bates-Guggenheim convention [17]:

$$\lg \gamma_{\text{Cl}^- \rightarrow 0} = \frac{AI^{1/2}}{1 + 1.5I^{1/2}} \quad (2.9)$$

where A is the Debye-Hückel temperature-dependent limiting slope and I the ionic strength of the buffer solution. If ion molar concentration is c_i , number of electric charges is z_i , then $I = (1/2)\sum c_i z_i^2$.

Haber and Klemensiewicz gave a full account of the response of the glass electrode in their 1909 paper [18, 19]. The next advance towards the microelectrodes was the miniaturization of the glass electrode by Caldwell in 1954 [20]. He used it to measure intracellular pH in crab muscle fibers. Hinke created ion-selective electrodes for potassium and sodium using the respective sensitive glasses developed by Eisenmann, Rudin and Casby two years earlier [21], based on the work of Lengyel [22] published in 1934. He used them to show the correlation between sodium ion concentration in blood, and blood pressure [23, 24]. Also, similarly to what Caldwell did with the glass electrode, Hinke created sodium and potassium ion-selective microelectrodes in 1959 [25] using the same type of ion selective glasses. With his revolutionary *ion-selective microelectrodes* (Fig. 2.3), Hinke was able to perform the first true intracellular ion-selective measurements, and determined the potassium and sodium ion concentration in the muscle cells of the propodite of crab and lobster (*Carcinus mænus* and *Homarus vulgaris*). His microelectrodes originally had a tip cross section of $20 \mu\text{m} \times 150 \mu\text{m}$, with a wall thickness of 1 - 4 μm , and a resistance of $10^{10} - 10^{11} \Omega$.

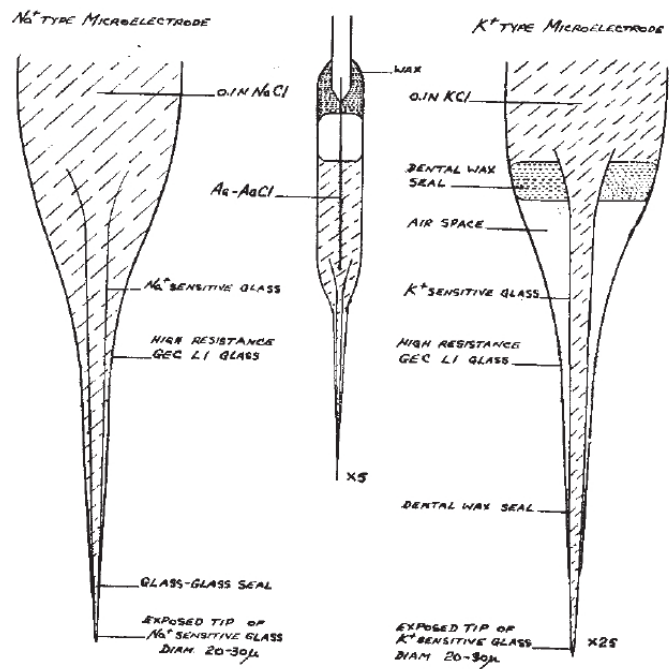


Figure 2.3: The first true ion-selective microelectrodes, created by Hinke to measure intracellular sodium, and potassium ion concentration. As published in his 1959 *Nature* paper [25].

2.1.3 Liquid ion exchanger membrane based microelectrodes

While Hinke was able to eventually decrease the tip diameter of his ion-selective microelectrodes to 1 μm or less, the sensitive area was on the order of 10 μm in length with a diameter of 5 μm or more at the top of this area. In order to measure intracellular ion activity, the entire sensitive part had to be pushed into the cell, causing significant damage. In addition to the problem of size, they were difficult to fabricate.

By that time, liquid ion exchangers have been used in liquid-liquid ion extraction processes in industry and, as models for biological membranes [26, 27]. Sandblom, Eisenmann and Walker published two papers in 1971 about a rather exhaustive theoretical treatment of such liquid ion exchanger (LIX) membranes [28, 29]. Also in 1971, Walker was able to prepare a miniaturized version of the electrodes based on the LIX membranes [30]. He writes in [30]:

„A liquid ion exchanger is composed of an organic electrolyte dissolved in a water-immiscible solvent, usually an organic solvent with a low dielectric constant. Owing to the low dielectric constant of the exchanger, inorganic ions have a very low solubility in the exchanger and, consequently, a membrane made of a liquid ion exchanger is much more permeable to ions whose valence sign is opposite to that of the organic ion than to ions of the same valence sign because of ion pair formation with the organic ion.“

Walker also added a crucial step to the fabrication of these microelectrodes: the silanization of the inner surface of micropipette. The surface of the freshly pulled pipette is highly hydrophilic, and the sensing membrane in the pipette tip is hydrophobic. To improve the adhesion of the two, and to prevent the electrolyte from creeping along the pipette wall from either side, Walker silanized the surface. This improved stability and life-time of these microelectrodes drastically.

He used the new LIX ion-selective microelectrodes to measure chloride, and potassium ion activity in *Aplysia* neurons. He estimated the resistance for his electrodes from the charging time of the input of the operational amplifiers in the range of 10^9 to $10^{10} \Omega$. He also performed selectivity measurements on the microelectrode, using the Nicolsky-equation [31]:

$$E = E^\theta + \frac{RT}{z_i F} \ln \left[a_i + \sum_j \left(k_{ij} a_j^{z_i/z_j} \right) \right] \quad (2.10)$$

where E is the emf, E^θ the standard electrode potential, z the ionic valency including the sign, a the activity, i the ion of interest, j the interfering ions and k_{ij} is the selectivity coefficient. The smaller the selectivity coefficient, the less is the interference by j . These microelectrodes were surpassed by the following generation of ion-selective microelectrodes, based on the ionophores.

2.1.4 Ionophore based microelectrodes

The ion-selective microelectrodes used today are based on the ionophores. These are carriers for specific ions, and act as complexing ligands. Štefanac and Simon published their work concerning the use of nonactin, a lipophilic antibiotic, as ionophore in ion-selective membranes [32, 33]. Their cell consisted of the following elements:



The inner solution was 0.1 M in the chlorides of all cations tested in one set of experiments and was buffered to pH 8 with acetic acid and triethanolamine. They dissolved nonactin and nonactin homologs in carbon tetrachloride, and transferred onto sintered glass discs to form a membrane. Their cell showed a selectivity for certain cations, especially potassium ion.

For quite some time after the discovery that ionophores can be used in ion-selective electrodes, the LIX membrane based ion-selective microelectrodes were used instead. The reason for this is the relatively high resistance of the membranes employing the neutral carrier ionophores. They had however, a great advantage over the

LIX membranes: their selectivity. In cases, as Amman writes in his 1987 paper [34] it reached a factor of 5000:

„[With the valinomycin based microelectrodes ...] extremely high K⁺ selectivities are obtained, e.g. a rejection of Na⁺ by a factor of 5000 and of acetylcholine by a factor of 3400. At a constant background of 140 and 500 mM Na⁺, the detection limit of the K⁺ sensor is at 1.6×10^{-5} and at 2.5×10^{-5} M K⁺, respectively.”

and

„Valinomycin-based microelectrodes will find increasing application only if their electrical resistances can be further reduced without inducing a loss in K⁺ selectivity.”

Oehme and Simon did a comparison of the two types much earlier, in 1976 [35], and already realized the major difference between the two. A slightly improved version by Wuhrmann [36] found only limited use in physiology. In both of these papers, valinomycin based microelectrodes with a very high resistance ($R = 10^{11} \Omega$) are described. Such high resistances of course result in very long response times ($\tau > 30s$).

The big breakthrough came when Ammann realized, that the resistance of neutral carrier-based membranes can be lowered drastically if both lipophilic salts and polar membrane solvents are used to form the membrane phase [34]. With this improvement, he lowered the resistance and essentially got the same as the LIX membranes had at the time, but managed to maintain the extremely high selectivity.

The first synthesized ionophores were introduced in 1969 by Kimura and co-workers [37]. Since then, many research groups synthesized ionophores for many different ions.

pH and blood gases have been measured routinely since Severinghaus and Bradley developed the blood gas analyzer for CO₂ and O₂ in 1958 [38]. These are not based on ionophores, but will be described here briefly because they are related closely to the metal/metal-oxide microelectrodes used in this dissertation. To measure oxygen, they used Clarks electrode [39], and for carbon-dioxide, they developed a gas gas sensor, which since has been known as the „Severinghaus-electrode”. It is based on pH measurement in a thin membrane on the surface of a glass pH-electrode. Carbon-dioxide diffuses to the membrane, dissolves in the thin film, and lowers the pH. The

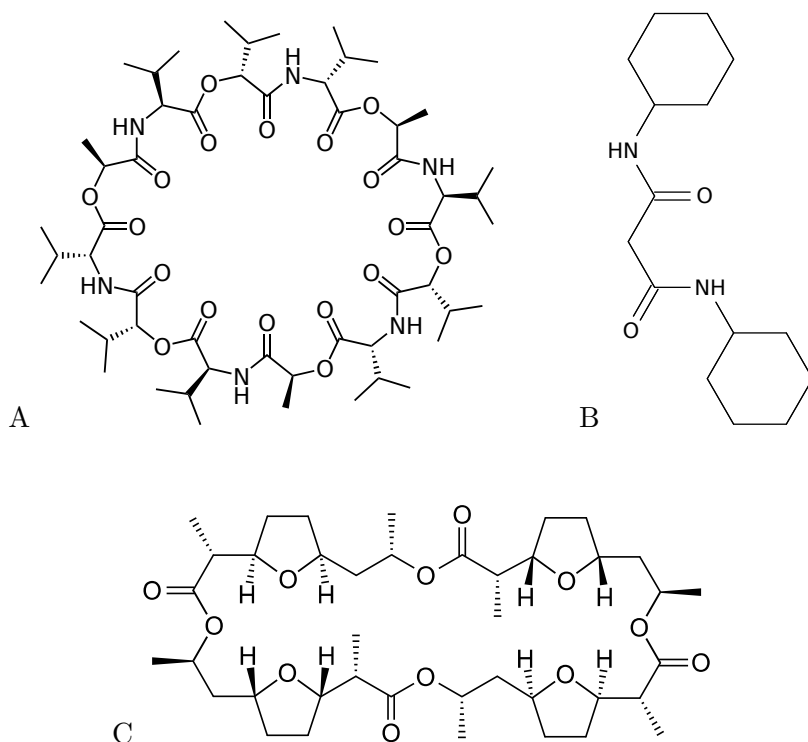


Figure 2.4: (A) Valinomycin, (B) bis-N,N-dicyclohexyl-malonamide, and (C) nonactin, ionophores for potassium, magnesium, and ammonium ions, respectively.

cell has been miniaturized by several research groups [40–44]. The cited papers are all using an improved, miniaturized, microelectrode version of the original electrode. I used a similar, antimony based miniaturized Severinghaus–electrode in my masters thesis, and published spatially resolved CO₂ measurements – with the same electrode – of living yeast colonies in [45].

A big advancement in the field of ion-selective electrodes was the elimination of the internal filling solution from the conventional ion-selective electrodes. This resulted in the so-called *solid-contact* electrodes. The first of these were unstable, because there was no reversible and fast ion-to-electron transducer [46]. Solid-contact electrodes had already been around since the 1970s with the invention of the coated-wire electrode (CWE) [47]. The instability was solved by the electropolymerization of a thin layer of conductive polymer onto the solid contact, that showed a mixed electronic and ionic conductivity, thereby providing a stable ion-to-electron interface [48–51]. A wide range of conductive polymers are used, including polypyrroles [52], polythiophenes [53], and polyanilins [54]. In this thesis, the ion-to-electron interface in the solid-contact ion-selective microelectrodes is PEDOT (poly(3,4-ethylenedioxythiophene)), first used for this purpose by Johan Bobacka and coworkers [53]. Solid-contact electrodes were used in the work done in our lab-

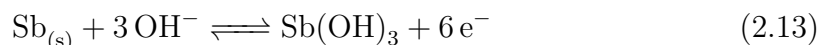
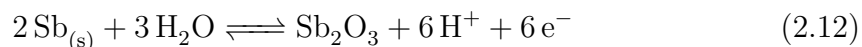
oratory earlier [55–57].

An interesting application of solid-contact microelectrodes is described in [58]. An array of electrochemical sensors, including 27 microelectrodes were used to determine the concentration of certain ions in the martian soil.

The lower limit of detection of ion-selective electrodes has usually not been lower than 10^{-6} M. Several research groups have achieved better results recently by optimizations [59]. Lower limit can be achieved by drastically reducing zero-current ion fluxes from the membrane in the direction of the sample [60]. Such fluxes have historically deteriorated the detection limits and observed selectivities of such sensors by many orders of magnitude [61].

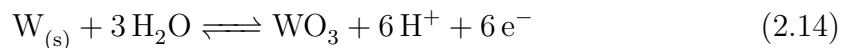
2.1.5 Metal/metal-oxide pH microelectrodes

Since the glass electrode cannot be effectively miniaturized due to the reasons detailed in the previous sections, intensive research has been conducted for several decades to improve metal/metal-oxide electrodes. One of the most often used type of these is the Ir/IrO₂ electrode [44]. The oldest is certainly the Sb/Sb₂O₃ electrode, its initial characterization dating back to 1923 [62]. It is based on the equilibrium between antimony and the antimony-oxide on its surface. It is pH sensitive because hydrogen ions participate in the equilibrium:



The main reason this particular electrode is so popular is that the melting point of antimony and borosilicate glass are similar ($T_{m,\text{Sb}} = 630.63$ °C, $T_{m,\text{glass}} \approx 700$ °C), and manufacturing them is relatively easy with standard glass blowing techniques.

Another very popular metal/metal-oxide electrode used for pH measurements is the tungsten electrode. Its function is also based on the equilibrium between the metal and its oxide:



2.1.6 The potentiometric measurement

The generation and measurement of the voltage in the potentiometric cell are closely related. Unfortunately, as with any other technique, the measurement itself influences the investigated system, and therefore the measured value. This effect is especially strong in potentiometry. Fig. 2.5 shows the circuit diagram of the generation

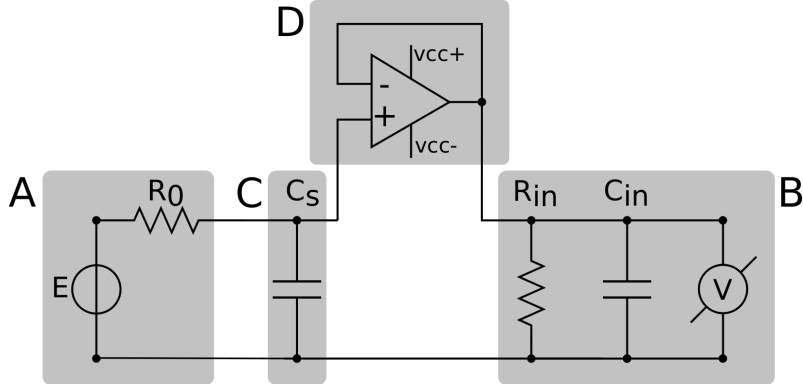


Figure 2.5: The model of the potentiometric measurement. The circuit is constituted by 4 parts: (A) voltage source, the potential difference between the reference and the measuring electrodes with an R_0 output resistance. (B) The measuring circuit, which can be split into 3 elements: a voltmeter, a resistance R_{in} to account for current flowing through the terminals of the voltmeter, and an input capacitance C_{in} . (C) The electrical connection between the voltage generator and the measuring circuit, with a capacitance C_s . (D) Unity gain current buffer built from an operational amplifier in the non-inverting voltage follower configuration.

and measurement of the voltage. First it will be discussed as if the amplifier wasn't present in the circuit. Without the amplifier, it can be split into three parts [63]:

(A) *Source of the voltage.* The potential difference V is developed across the output of an ideal voltage source E in series with a large output resistance R_0 . In the potentiometric cell, R_0 is the resistance of the measuring electrode, and E is the potential of the measuring electrode with respect to the reference electrode. Although E is regarded perfect in this model, and its voltage is independent of the current drawn, the output voltage V is smaller than E , because of the ohmic drop $iR_0 = E - V$. Since the resistance of a microelectrode can be in the range of mega-, or even gigaohms, very large errors may result from very small currents.

(B) *The measuring circuit* consist of three elements. The first element is the voltmeter V with infinitely large input impedance. It draws no current, since $i = U/\infty = 0$. It doesn't have any input capacitance (C_{in} is modeled separately), therefore it responds to the input voltage without any delay. The second element is a resistance R_{in} to account for the imperfection of real voltmeters, the current flowing through its terminals as a consequence of the potential difference between them. The third element is the input capacitance of the voltmeter, modeled by the capacitor C_{in} . The current flowing through R_{in} is $i_{R_{in}} = V/R_{in}$. It equals to the difference between the input and the output of the circuit, the error of the measurement of E :

$$E - V = i_{R_{in}} R_0 = \frac{R_0 V}{R_{in}} \quad (2.15)$$

The ratio of the two can be calculated by the formula for the voltage divider:

$$\frac{V}{E} = \frac{R_{in}}{R_0 + R_{in}} \quad (2.16)$$

Input resistance R_{in} of a typical voltmeter is in the range of $1 - 10 \text{ M}\Omega$. This relatively low resistance can cause a large distortion, because $R_{in}/(R_0 + R_{in})$ approaches 1 only if R_{in} approaches infinity, or R_0 approaches zero. Since R_0 is a given property of the circuit, the only way the error can be lowered is by increasing R_{in} . For example, the input resistance of a microelectrode amplifier is about $10^{12} \Omega$, and of a pH meter $\sim 10^{14} \Omega$. Based on Eq. 2.15 it is very important that $R_{in} \gg R_o$ to minimize the error in potential measurements. The effect of input capacitance C_{in} is discussed in the next section (*Response characteristics*).

(C) The connection between the voltage source E and the measuring instrument V . This element influences the measurement in two ways. First, it delays the voltage across V compared to E , the effect which is detailed in the next section (*Response characteristics*). The other effect is a consequence of a very small current, induced by stray capacitance. The cable between E and V acts as the plate of a capacitor. The other plate can be anything in the environment. If the capacitance of the element constituted by these two plates changes – by objects moving around in the environment, or charge transfer occurring – small current will flow through the cable. Since the overall resistance of the circuit is quite high due to the measuring microelectrode, even if very small currents are induced by the stray capacitance, large amount of noise can be added to V , because $V = iR_0$. This effect can be minimised by using shielded cables to decrease stray capacitance, and using as short connections between the high impedance elements and the amplifier as possible. Stray capacitance of a typical shielded (braided) cable is $\sim 100 - 200 \text{ pF/m}$.

(D) Operational amplifiers are used to solve several of the issues described above. They are introduced between the measuring electrode and the measuring circuit as seen in Fig. 2.5. The operational amplifier is used as a *unity gain current buffer*. It is achieved by connecting the output of the amplifier to the inverting input. In this configuration, the output is tied back to the inverting input, while the potential to be measured (with respect to ground) is connected to the non-inverting input. Since the operational amplifier does everything it can to keep the two inputs at the same voltage, and one of the output is fed back to one of the inputs, the output will be the same as the other input. The name of this circuit is *non-inverting voltage follower*. It comes from the fact that the output V_{out} follows V_{in} , and the sign of the two equal, as opposed to the inverting configuration, when $V_{out} = -V_{in}$. In other words, the circuit has unity ($\times 1$) gain: it does not amplify potential difference. The reason this circuit is used as an interface between the high impedance source and

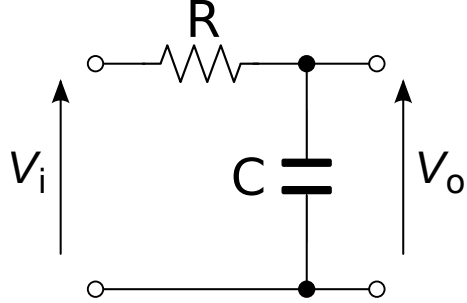


Figure 2.6: The series RC circuit.

the low impedance measuring circuit is that because of its high input impedance, it draws no current from the source. Therefore there is no loading error on its high impedance side. On the other hand, they have a low output impedance, and can drive the measuring instrument, with minimal R_0 of their own, and therefore there is no loading error on the low impedance side either. The input impedance of a typical opamp used for this purpose is around 1–10 T Ω , so $R_{in}/(R_{in} + R_0)$ is unity, and the measured V is almost identical to the source E , because V/E is also 1.

2.1.7 Response characteristics

Because the RC time-constant plays a central role in my thesis, I give a detailed derivation of it here. The potentiometric cell can be modeled as a series RC circuit (Fig. 2.6). Kirchhoff's second law states that the directed sum of the electrical potential differences (voltages) around any closed network is zero [64]:

$$\sum_{k=1}^n V_k = 0 \quad (2.17)$$

where n is the total number of voltages measured across the loop. This must be true for the energy to be conserved. Using Ohm's law to express the voltage across the resistor as iR and Kirchhoff's second circuit law on the series RC circuit, we get:

$$V_{in} - iR - V_{out} = 0 \quad (2.18)$$

where i is the current flowing through any two points of the circuit clockwise. Since i is nothing but the change of charge in time, $i = dq/dt$, and $V_{out} = q/C$, Eq. 2.18 can be rewritten as

$$V_{in} - \frac{dq}{dt}R - \frac{q}{C} = 0 \quad (2.19)$$

This can be rearranged to

$$\frac{dq}{dt} = \frac{1}{R} \left(V_{in} - \frac{q}{C} \right) \quad (2.20)$$

After cross multiplication we get

$$\frac{dq}{V_{in} - \frac{q}{C}} = \frac{dt}{R} \quad (2.21)$$

Rearranging it leads to

$$\frac{dq}{q - CV_{in}} = -\frac{dt}{RC} \quad (2.22)$$

To get q as a function of t , we need to integrate. At $t = 0$ the capacitor is not charged, so $q = 0$. Then, as we apply the voltage V_{in} , the capacitor slowly starts charging, until we arrive at a charge q :

$$\int_0^q \frac{dq}{q - CV_{in}} = \int_0^t -\frac{dt}{RC} \quad (2.23)$$

or

$$\ln(q(t) - CV_{in}) \Big|_0^q = -\frac{t}{RC} \Big|_0^t \quad (2.24)$$

After solving we get

$$\ln \left(\frac{q(t) - CV_{in}}{-CV_{in}} \right) = -\frac{t}{RC} \quad (2.25)$$

If we raise both sides to the natural exponent, we get

$$\frac{q(t) - CV_{in}}{-CV_{in}} = e^{-t/RC} \quad (2.26)$$

Solving for $q(t)$:

$$q(t) = CV_{in}(1 - e^{-t/RC}) \quad (2.27)$$

Since the voltage across the capacitor is $V_{out} = q/C$, dividing both sides by C leads us to

$$V_{out}(t) = V_{in}(1 - e^{-t/RC}) \quad (2.28)$$

This is the general expression to the voltage across a charging capacitor at any time instance t . To find the expression for the voltage when the capacitor is dis-

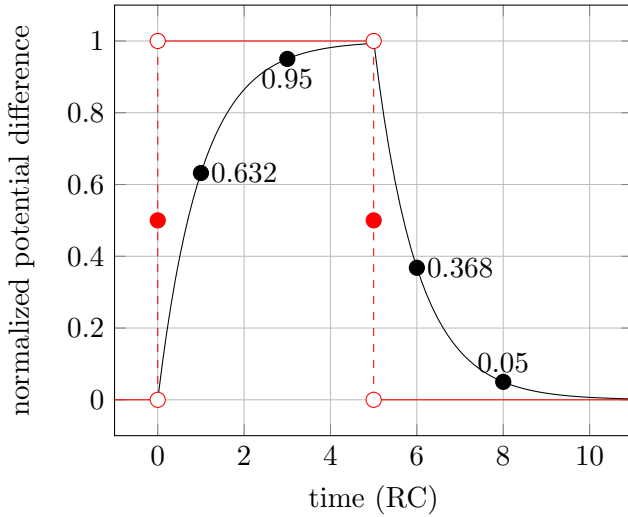


Figure 2.7: Charging and discharging the series RC circuit. Red: normalized input voltage (V_{in}) to the series RC circuit, two consecutive *Heaviside step functions*, the second one is inversed and shifted $5RC$ to the right. Black: normalized output voltage (V_{out}) of the series RC circuit.

charging, very much the same way we get:

$$V_{out}(t) = V_{in}e^{-t/RC} \quad (2.29)$$

RC is the time constant of the series RC circuit, denoted as τ in general. Observing Eqs. 2.28-2.29, it is the time that it takes to charge the capacitor by 63.2% ($1 - e^{-1} = 0.632$), or to discharge it by 36.8% ($e^{-1} = 0.368$). Fig. 2.7 shows the response to a *Heaviside step-function* input. After about $5 \times RC$, the output voltage practically reaches the input voltage (99%). It is useful to note the relation between the 95% response time $t_{95\%}$ and the time constant. In $3 \times RC$ time, the capacitor is charged by about 95%, therefore $t_{95\%} \approx 3 \times RC$.

To make Eqs. 2.28-2.29 useful in electrochemistry, we need to further modify them. In potentiometry, the important parameter is the potential of the measuring electrode. We always speak in terms of electrode potential, but it must be born in mind that it is measured with respect to the reference electrode, hence it is always a potential difference. But since we will take the difference between these differences as well, we just use the expression *potential* to refer to the state of the potentiometric cell at any time instance t . In the generalized expression we substitute V_{out} for $E_{cell}(t)$, and V_{in} for $E_{cell}(\infty)$. Also, it is useful to generalize it for changes starting, and ending at any potential value, not just 0 or E_{out} . After these generalizations, from both equations we get:

$$E_{cell}(t) = E_{cell}(\infty) + [E_{cell}(0) - E_{cell}(\infty)]e^{-t/RC} \quad (2.30)$$

This equation [65] will be modified later in the thesis to estimate $E_{cell}(\infty)$ based on the other variables.

2.1.8 On the use of the expression „equilibrium”

Throughout my dissertation I use the expression *equilibrium* to describe a steady potential difference between the two terminals of the cell, the electrical contact of the measuring and the reference electrodes. However, this state of course cannot be regarded an equilibrium, since given enough time, the potential difference will reach zero eventually. The resistance of the whole cell is finite, and if there is a potential difference between any two points in the cell, current will flow. Two phenomena have to be distinguished. The first is the electrochemical process, which is in equilibrium *only* if cell potential difference have reached zero, i.e. the cell is depleted. The other process is the charging or discharging of a capacitance modeled by C in Fig. 2.6. This is the total capacitance of the measuring system, including the capacitance of the cables, and the amplifier input as well. If we accept the model described in the previous section, this can be regarded a purely physical process, which is in true equilibrium if the voltage across the capacitor C is the same as the voltage of the input ($V_i = V_o$). This state is what I refer to by equilibrium.

It must be kept in mind however, that the source of the potential difference in fact *does* change over time for a given electrolyte composition as a consequence of the very small current flowing through the cell (fA range). Therefore it is not an equilibrium, only a steady state.

2.2 Scanning Electrochemical Microscopy

2.2.1 Origins of the technique

Scanning Electrochemical Microscopy (SECM) is a branch of the Scanning Probe Microscopic techniques (SPM), of which the first was the Scanning Tunnelling Microscopy (STM), invented by Binnig and Rohrer in 1982 [66] building on their previous studies of controlled vacuum tunnelling published in 1981 [67, 68]. They received the Nobel Prize in 1986 „*for their design of the scanning tunneling microscope*”. It was a revolutionary technique, the first of its kind, and a pioneer for the other scanning techniques that followed. STM is capable of incredible resolution, down to the atomic scale. Optical techniques cannot reach this level of resolution, since they are limited by the wavelength of photons [69]. The wavelength of visible light is more than 1000 times bigger than an atom, so light cannot be used to „see” an atom. The STM probe tip is an extremely sharp – just one or two atoms at its point. There is a small electric voltage on the probe tip and depending on the height of different parts of the surface, more or less current will flow from the tip to the surface. By noting the changes in current, it is possible to recreate an image of the surface at the atomic level.

The next SPM technique, the Atomic Force Microscopy (AFM), was introduced not long after, in 1986 by Binnig [70, 71]. He writes in [70]:

„The atomic force microscope is a combination of the principles of the scanning tunneling microscope and the stylus profilometer. It incorporates a probe that does not damage the surface. Our preliminary results in air demonstrate a lateral resolution of 30 Å and a vertical resolution less than 1 Å. ... We envision a general-purpose device that will measure any type of force; not only the interatomic forces, but electromagnetic forces as well.”

Indeed, since its invention, AFM has found many applications, and became an invaluable tool of surface analysis. After these two techniques were established, many more SPM variants followed in a relatively quick succession. Here a few are mentioned:

- MFM, magnetic force microscopy (1988) [72]
- SICM, scanning ion-conductance microscopy (1989) [73]
- BEEM, ballistic electron emission microscopy (1990) [74]

- EFM, electrostatic force microscopy (1991) [75]
- KPFM, kelvin probe force microscopy (1991) [76]
- SHPM, scanning Hall probe microscopy (1992) [77]
- SThM, scanning thermal microscopy (1994) [78]
- SVM, scanning voltage microscopy (1998) [79]

The electrochemical version of SPM, the Scanning Electrochemical Microscope (SECM¹) was introduced in 1989 by Allen J. Bard [80], „*the father of modern electrochemistry*”, main author and editor of the monography about SECM [81]². It must be mentioned however, that the notion of spatially resolved chemical information was first proposed by Engstrom, three years earlier, in 1986. He published a paper about measurements with a microelectrode in the diffusion layer of another electrode, using a bipotentiostat and a micro-manipulator [83]. He writes in 1989 [84] referring to his 1986 paper [83]:

„*The concept behind what has come to be called SECM was first demonstrated in 1986, when microelectrodes were used to amperometrically detect chemical species produced at a specimen electrode.*”

But the term „*Scanning Electrochemical Microscope*” was coined by Allen J. Bard, and he and his coworkers generalized the idea to three dimensions, and layed down the foundations and theory of the technique.

The two main variants of the technique are the amperometric and the potentiometric modes. For the first few years, the SECM was only used in amperometric mode. The next step towards obtaining true chemical information, not just surface topography and conductivity, was the combination of potentiometry and the SECM. Although several papers have been published already about spatially resolved potentiometric scans, the first potentiometric SECM images appeared on the pages of the paper of Horrocks and Bard written in cooperation with my doctoral supervisor, Professor Géza Nagy [85]. I used very similar antimony microelectrodes as SECM probes to measure local pH throughout my work, and prepared them in the same way as described in that paper.

¹The abbreviation „*SECM*” is used interchangeably for both the technique (Scanning Electrochemical Microscopy) or the instrument (Scanning Electrochemical Microscope).

²Recently, a new version of the book has been published [82].

2.2.2 Potentiometric SECM

The potentiometric probe is passive, it does not generate or collect, and it can be described as „*substrate generates / substrate collects – tip detects*” staying with the original naming scheme. In this mode, similar to the other modes, the probe is scanned through the points of a raster grid (Fig. 2.8). But instead of an amperometric measurement, the potential of the probe is measured against a reference electrode, immersed in the same electrolyte at a fixed location. For the reasons detailed in the section „The potentiometric measurement”, a voltage follower is introduced between the electrometer and the measuring electrode. The first complete work featuring potentiometric SECM images were published in 1993 [85]. In that work, the authors successfully measured pH on a microscale with an antimony microelectrode.

Later, potentiometric SECM found an application in corrosion science. Researchers in that field are curious about the concentration of certain ions in the electrolyte adjacent of the corroding sample. Ion-selective electrodes and the SECM are good tools to study the dissolution of these ions. Concentration profiles of zinc [86], magnesium [87–89] and hydrogen ions [87] were recorded by several research groups.

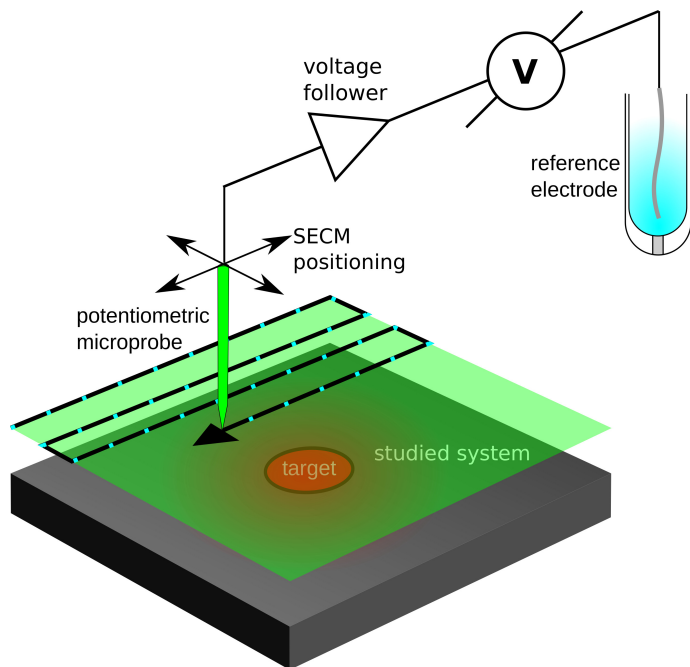


Figure 2.8: A typical potentiometric SECM setup. The probe is scanned through the points of a 2D raster at a constant height above the studied surface. The probe is stopped at every sampling points (here blue dots), and the potential against a reference electrode is recorded. For potentiometric microelectrodes, the use of a voltage follower is necessary to avoid loading error and reduce noise.

2.2.3 Distortion and image processing in SECM

Signal processing techniques has been widely used in optical microscopy [90], and in scanning probe microscopy to decrease imaging distortion. Distortion is any difference between the obtained image and reality. It is caused by the imperfection of the measuring system, which can be modeled as a measurement transfer function, or convolution function F , such that the output $y(t)$ can be written as a function of the input x as

$$y(t) = F(x(t)) \quad (2.31)$$

If F is known, the inverse function F^{-1} can be found and used as deconvolution function.

There are many sources of SPM imaging distortion. In atomic force microscopy, and scanning tunnelling microscopy, it is usually a consequence of the tip-sample interaction, causing the various artefacts [91]. Broadening of nanometer-scale features by up to three times is a common occurrence in STM [92]. The deconvolution function in this case is closely related to the geometry of the tip and its angle compared to the sample. If these are known, image restoration is possible by deconvoluting in the spatial domain [93–95]. Time, and frequency domain deconvolution is also commonly used in SPM techniques to remove time-dependent image artefacts, usually caused by the relatively long response time compared to scanning speed [96].

Deconvolution of images obtained with the scanning electrochemical microscope has also been reported by the Bard group [97]. In that work, amperometric images have been restored (deblurred) by a linear combination of Laplacian and Gaussian filtering. The main source of distortion in amperometric SECM imaging is the feature broadening caused by diffusion. The deconvolution function was derived from Fick's law of diffusion, and used as a calculation kernel to cycle through the data points of the 2D raster and obtain the deblurred image.

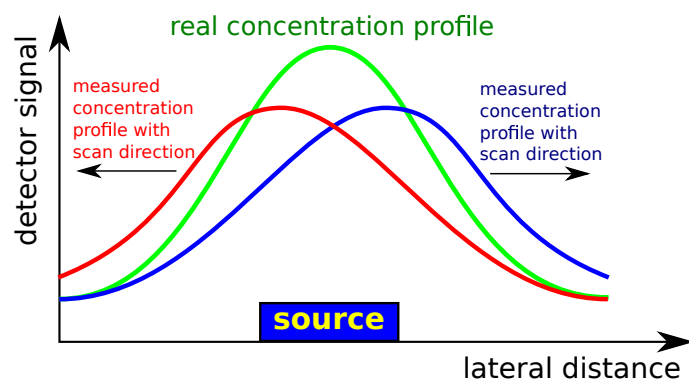


Figure 2.9: The distortive effect of potentiometric SECM imaging when scanning at relatively high speed. The effective speed of the probe is too high, and therefore the time available for the potentiometric cell is too short to reach equilibrium before recording the potential difference at a given point. The image is blurred along the scan line in the direction of the scan.

Chapter 3

Materials and Methods

3.1 Ion-selective microelectrodes

I used two kinds of ion-selective microelectrodes in my thesis: metal/metal-oxide microelectrodes and ion-selective micropipette electrodes. To measure pH on a microscale, metal/metal-oxide type microelectrodes are widely used. They are based on the equilibrium between the metal and their oxide. Hydrogen ions participate in the equilibrium, therefore the electrode potential will shift when pH changes. The ion-selective micropipettes on the other hand, are based on the ionophores, which are specific to certain ions, ensuring their selectivity. If an ion-exchange membrane is prepared with a particular ionophore, the crossmembrane potential depends only on the activity of the particular ion which the ionophore is selective to. I used several types of ion-selective microelectrodes as SECM measuring tips. For pH-microscopy, I used an antimony and tungsten microelectrodes. To map local K^+ and Mg^{2+} ion concentration, I used ion-selective micropipette electrodes with the appropriate ion-selective cocktails. I used traditional liquid-contact micropipettes, and new, low resistance solid contact micropipettes as well.

3.1.1 Preparation of the microelectrodes

3.1.1.1 Metal/metal-oxide electrodes

Antimony pH-sensitive microelectrode The antimony microelectrode fabrication process is based on the original work of Bard [85]. Antimony powder (Szkarabéusz, Pécs, Hungary) was melted, then pulled into a relatively thick walled borosilicate glass tube ($d_i=2$ mm, $d_o=10$ mm) by applying vacuum on the backside of the tube. In this way, a continuous column of solid antimony was sealed into the glass tube. Then, the glass tube with the antimony inside was melted again. Since the melting points of antimony and borosilicate glass are very similar, they could be pulled

together with standard glass blowing techniques, using tweezers. With this method, very fine, glass-sealed antimony microwires can be obtained. After this step, the diameter of the antimony wires was typically around 30 μm . If it was necessary, the microwires were pulled even further with a vertical puller (Sutter Instrument, 1 Digital Dr, Novato, CA 94949). After the pulling stage, the wires were broken into pieces with a length of 3 – 4 centimeters. Then, they were investigated under an optical microscope to select pieces with a continuous antimony wire. Due to the fragile nature of these microelectrodes, several of them were used through the course of my work. The diameter of the antimony microelectrode used in a particular experiment is always specified in the discussion of that experiment. To make electrical contact between the measuring instruments and the antimony microwires, a thin copper wire was glued to the glass shielding of antimony wire with conductive silver-epoxy (Amepox Microelectronics, Ltd. 90-268 Lodz Jaracza, Poland), making sure that the epoxy also covered the exposed antimony wire. After curing for 1 hour at a temperature of 200 °C, the antimony microelectrodes were ready. All electrodes were tested before usage by calibration in three buffer solutions ($\text{pH} = 4, 7, 10$).

Antimony pH-sensitive combined macroelectrode Antimony/silver combined macroelectrodes were used to study the effect of stirring on the delay in potentiometric measurements with antimony electrodes in general. To make these electrodes, copper wires were soldered to one end of a ~ 5 mm long silver and antimony wires ($d = 1$ mm). Antimony wires with such diameter were made by sucking molten antimony into a $d_i = 1$ mm glass capillary. Then, the glass was broken to acquire the antimony wire, which was then trimmed to ~ 5 mm length. Both solder joints were strengthened mechanically by small segments of heatshrink tubes. The obtained electrodes were carefully pushed down into a glass tube ($d_o = 5$ mm, $d_i = 4$ mm) until they both reached the end of the glass tube. Then, the remaining space in the tube was filled with epoxy resin. Finally, after the resin was cured, the end plate was sanded down to 4000 grit, and polished on three different fiber cloths (Buehler), containing alumina slurry with decreasing particle size; 1 μm , 0.3 μm and finally 0.05 μm .

Tungsten pH-sensitive microelectrode Since tungsten has the highest melting point of all the elements (3422 °C), the method described in the previous paragraph cannot be used. Instead, tungsten microwire with a diameter of 30 μm (Element-explorer, Montreal, Canada) were sealed into a borosilicate glass capillary ($d_i=1.12$ mm, $d_o=2$ mm, no filament, World Precision Inc., Sarasota, Florida, USA). To seal the microwire, one end of the capillary was closed with flame. Then, a 1 cm long



Figure 3.1: Antimony/silver pH-sensitive combined macroelectrodes. Left side: top view of two examples, right side: front view, displaying the antimony and silver electrodes. This type of electrode was used to investigate the effect of buffer stirring on response time.

tungsten microwire was inserted from the other end, and pushed down to the sealed end. The sealed end was melted again while vacuum was being applied from the open end. The capillary was kept in the flame until 4-5 mm, about half of the microwire was sealed into the glass. To make electrical contact between the microwire and the measuring instruments, a small piece of solder was inserted into the capillary. The solder was melted in flame, and pushed down to the sealed end of the capillary. While the solder was still melted, a copper wire was inserted into the solder. Microelectrodes with 30 µm tungsten filaments from a 100 W Tungsram incandescent lightbulb were also prepared, using the same method. Fig. 3.2 shows the tip of the finished tungsten microelectrodes.

3.1.1.2 Micropipette ion-selective electrodes

Ion-selective microelectrodes were prepared using micropipettes pulled from borosilicate glass capillaries B100-50-10 (Sutter, Novato, CA, USA). The glass capillaries were first soaked in „piranha solution”, then thoroughly washed with twice deionized water and ethanol, and dried in oven at 105 °C. Micropipettes were pulled from the capillaries by using a pipette puller (Sutter Instruments, type P-30, Novato, CA, USA). The inner wall of the pipette tips were hydrophobized by exposing them to a solution of dimethyldichlorosilane in carbon tetrachloride through capillary action, and baking them at 200 °C for 30 minutes in a closed petri dish. The ionophore cocktail was filled into the micropipette tip under vacuum. Two kinds of ionophores were used. Bis-N,N-dicyclohexyl-malonamide and valinomycin for Mg²⁺, and K⁺, respectively. Bis-N,N-dicyclohexyl-malonamide was synthesized at the Budapest University of Economics and Technology [98]. Selectivity coefficients of this ionophore toward Na⁺ and H⁺ ions are available in [98]. The composition of the ion-selective cocktail is given in Table 3.1. All the components in the ionophore cocktail were supplied by Sigma-Aldrich (St. Louis, MO), except the home-made ionophore.

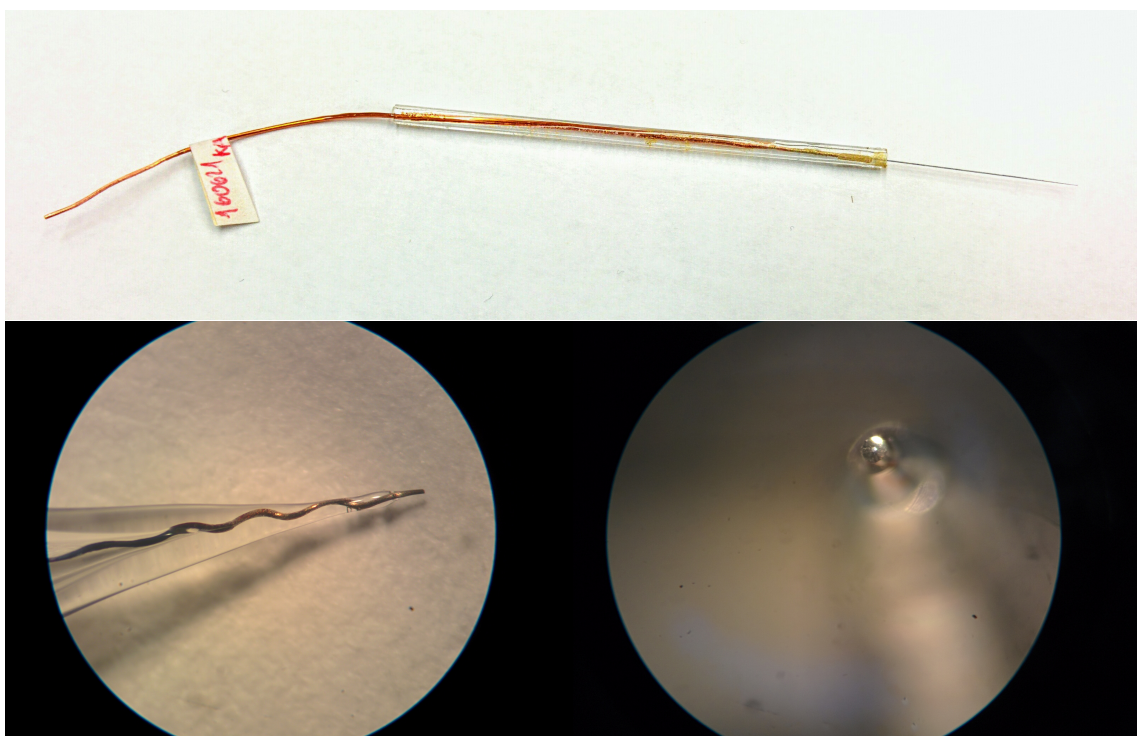


Figure 3.2: Antimony and tungsten microelectrodes for local pH measurements. Side view of the microelectrodes prepared from commercial 30 μm tungsten microwires (C) and from 100 W Tungsram filaments (D). Front view of the same electrodes (C and D).

Table 3.1: Composition of the mixture employed to produce the cocktail for the Mg^{2+} and K^+ ion-selective microelectrodes. Either bis-N,N-dicyclohexyl-malonamide or valinomycin was used.

Component	Quantities for 200 μL of the mixture	
	Content	wt%
Tetrahydrofuran (THF)	100 μL	-
Poly(vinyl chloride) (PVC)	7.68 mg	5.06
bis-N,N-dicyclohexyl-malonamide	2.23 mg	1.47
valinomycin	2.23 mg	1.47
Potassium tetrakis(4-chlorophenyl)-borate (PTCB)	2.13 mg	1.40
2-nitrophenyl octyl ether (oNPOE)	139.79 mg	92.07

The ionophore cocktail was cured for 24 hours, to allow the THF to be evaporated.

Liquid-contact ion-selective microelectrodes For the liquid contact version, an internal solution was backfilled with the assistance of a microsyringe. The internal filling solution was 10 mM $MgCl_2$ and 0.25 M KCl in the case of a Mg^{2+} ion-selective electrode, and 10 mM KCl for a K^+ ion-selective electrode. The internal reference electrode for both liquid contact electrodes was a chlorinated silver wire. To chlorinate silver wires, they were submerged into 1 M $FeCl_3$ solution for a few seconds, and cleaned from traces of Fe^{3+} with cc. HCl. The internal solution and the reference electrode were confined in the micropipette with hot glue. A sketch and micrograph of the liquid-contact ion-selective microelectrode are shown in Fig. 3.3A.

Solid-contact ion-selective microelectrodes The solid-contact ion-selective microelectrodes were built using the same components employed for the fabrication of the conventional ISME, except in this case instead of the internal solution and chlorinated silver wire, the internal contact was provided by a PEDOT (poly(3,4-ethylenedioxythiophene)) coated 33 μm diameter carbon fiber cut to 35 mm length. The modified carbon fiber was pushed from the back opening of the pipette as close to the orifice as possible to minimize the thickness of the membrane between the solid contact and the sample, and therefore electrode resistance [55]. The top opening of the micropipette electrode was sealed using hot glue. A micrograph of the resulting microelectrode is depicted in Fig. 3.3B.

Preparation of the solid contact A copper wire was attached to the carbon fiber using silver-epoxy adhesive, to provide electrical contact. The portion of the fiber to be in contact with the ionophore cocktail was then coated with PEDOT conductive polymer in an electrochemical cell composed of the carbon fiber as working electrode,

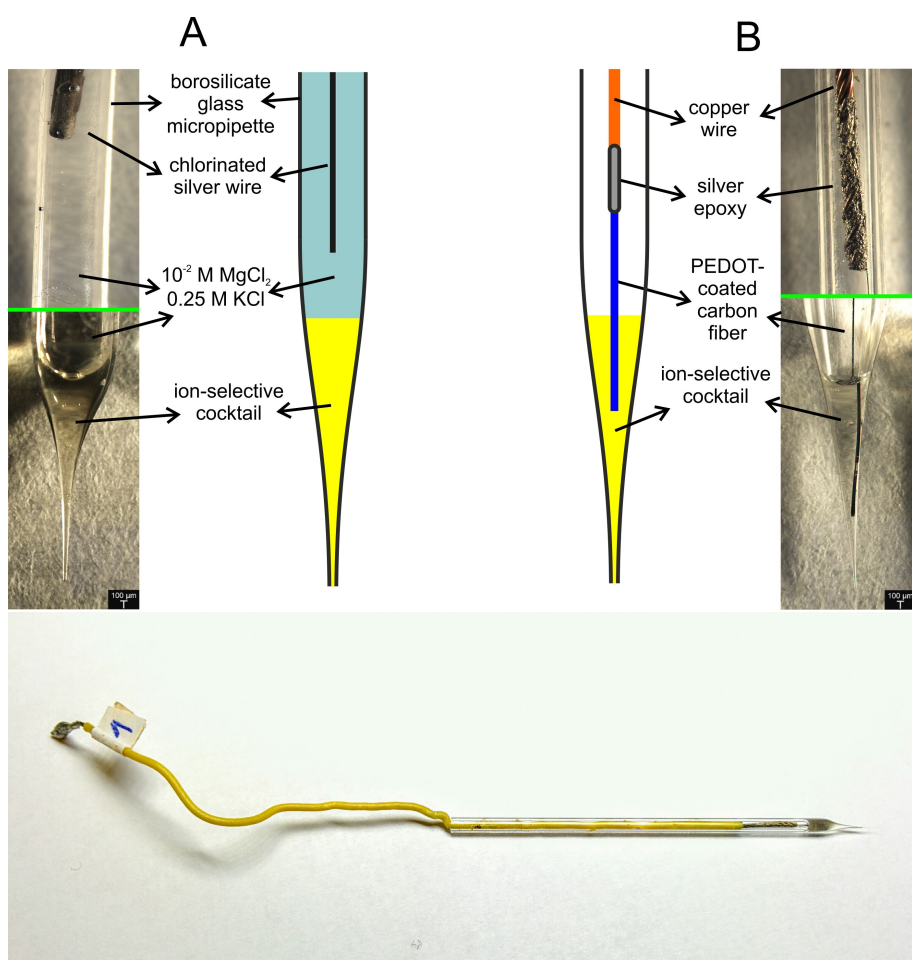


Figure 3.3: Sketches and micrographs of the micropipette electrodes fabricated for the selective detection of Mg^{2+} ions: (A) liquid-contact, and (B) solid-contact ISME's. The K^+ solid contact micropipettes were identical in construction, except the composition of the ion-selective cocktail and the internal filling solution for the conventional electrodes, which was valinomycin, and 10^{-2} M KCl, respectively.

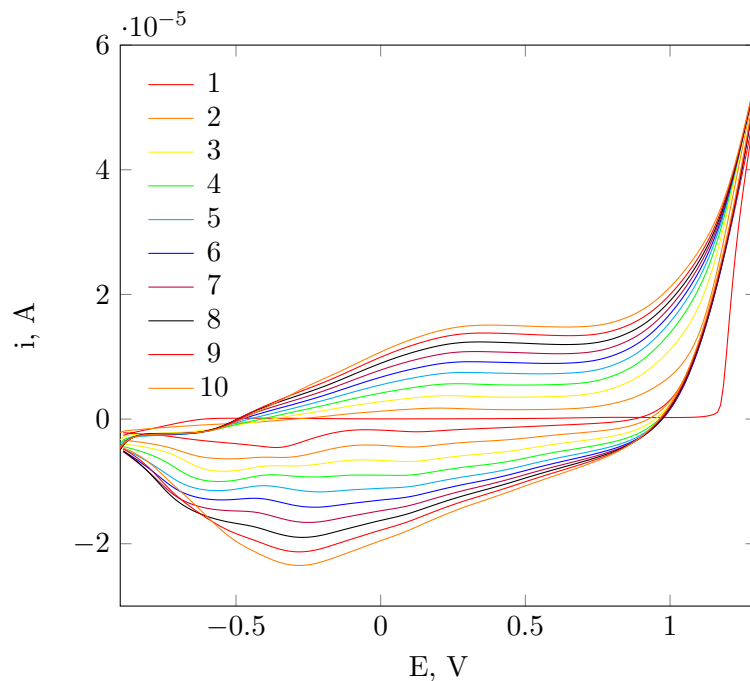


Figure 3.4: Cyclic voltammetric electropolymerization of PEDOT onto the carbon fiber to create the solid internal contact for the ion-selective microelectrodes. Top left inset indicates the order of the consecutive cycles.

an Ag/AgCl wire immersed in the electrolyte as quasi-reference electrode, and a platinum wire as the auxiliary electrode. The monomer was 3,4-ethylenedioxythiophene dissolved in $\text{BMIM}^+\text{PF}_6^-$ (1-butyl-3-methylimidazolium hexafluorophosphate) ionic liquid [55]. Oxygen was purged from the EDOT-solution with nitrogen gas before and during the polymerization. Then, PEDOT was polymerized with 10 consecutive cycles from -1.0 V to 1.5 V with a scanrate of 100 mV/s (Fig. 3.4).

3.1.2 Instrumentation for the microelectrodes

Microelectrodes have high resistance, therefore, to avoid loading error, some sort of impedance matching is necessary. This is also crucial to minimize noise caused by stray capacitance. Where the measuring apparatus lacked the high input impedance, a TL082 operational amplifier (Texas Instruments, Texas, USA) based unity gain voltage follower was used between the microelectrode and the measuring apparatus. To record the potential difference between the measuring microelectrode and the reference electrode, either of these instruments were used:

- MeTeX Instruments M-3640D 3 1/2 Digit digital multimeter with the TL082 voltage follower,

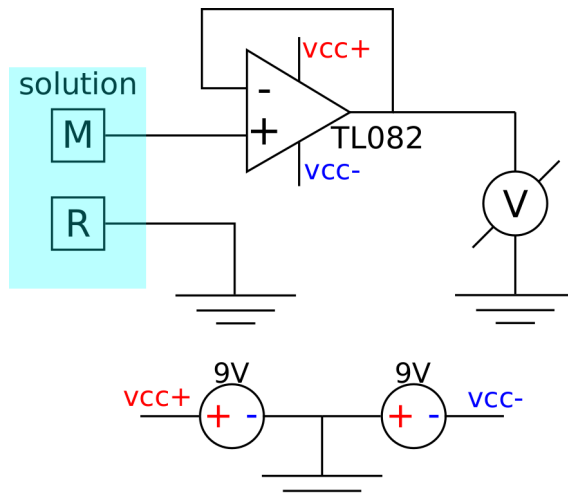


Figure 3.5: The potentiometric cell with the TL082 voltage follower. M: measuring electrode, R: reference electrode, V: voltage meter, $vcc+$ and $vcc-$: positive and negative rail of the power supply for the operational amplifier.

- Autolab Electrochemical Workstation (Metrohm, Herisau, Switzerland) with the TL082 voltage follower,
- eDAQ Ecoder 402 Electrochemical Workstation with the eDAQ pH/ISE isoPod (eDAQ Pty Ltd, Australia),
- eDAQ pH/ISE isoPod USB (eDAQ Pty Ltd, Australia),
- Home made, Arduino based DAQ.

A 25 cm long shielded coaxial cable was used between the amplifier and the microelectrode. Unshielded cable length was always minimized to less than a centimeter, excluding the length of the microelectrode itself. Connection was always provided by BNC connectors. The TL082 operational amplifier was powered by two 9V batteries, providing $\pm 9V$, and a convenient ground node (Fig. 3.5).

3.1.2.1 Home-made, Arduino based DAQ

The instrument is based on an DIP30 Arduino Nano, with an ATmega328 microcontroller (5V, 16MHz, Arduino AG, 2016, www.arduino.cc). A Texas Instruments ADS1115 16 bit analog-digital converter was connected to the microcontroller board through I²C interface. A virtual ground between 0 and 5 V was established by a voltage divider circuit. The virtual ground was driven by an OPA342 low voltage, rail-to-rail, high input impedance operational amplifier, provided by Texas Instruments as a generous gift. The virtual ground was connected to the reference electrode, and

one of the differential inputs of the AD1115. The measuring electrode was connected to the other differential input through a TI Tl082 high input impedance operational amplifier. The recommended supply voltage for this amplifier is $\pm 18V$, but it worked surprisingly well with the $\pm 2.5 V$ provided by the split 5 V of the USB port. The microcontroller ran the following program, a modified version of [99]:

```
#include <Wire.h>
#include <I2Cdev.h>
#include <ADS1115.h>

ADS1115 adc0(ADS1115_ADDRESS_ADDR_GND);
float scalefactor = 0.03125;
float time;

uint16_t currentADCreadings;

void setup(void)
{
    Serial.begin(115200);
    Wire.begin();
    adc0.initialize();
    // initialize ADS1115 16 bit A/D chip
    adc0.showConfigRegister();
    adc0.setRate(ADS1115_RATE_860);
    // 860 samples/sec
    adc0.setMode(ADS1115_MODE_CONTINUOUS);
    // continuous sampling

    adc0.setGain(ADS1115_PGA_1P024);
    // 4x gain, +/- 1.024 V, 1 bit = 0.03125 mV, 2.4 MOhm

    adc0.setMultiplexer(ADS1115_MUX_P0_N1);
    // sets mux to differential
}

void loop(void)
{
    time = 0.001 * millis();
    currentADCreadings=adc0.getConversion();
```

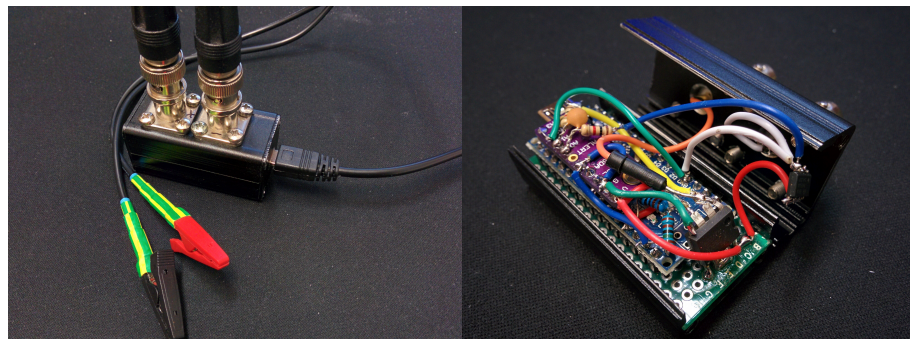


Figure 3.6: The home-made, Arduino based DAQ.

```

Serial.print(time,4);
Serial.print(' ');
Serial.println(adc0.getMilliVolts(),4);
}

```

While on the PC side (Debian Linux 9.x) the serial port was continuously monitored for incoming data, which was stored in the file *data.dat*:

```

screen -d -m -S ads /dev/ttyUSB0 115200
screen -S ads -X logfile data.dat
screen -S ads -X log

```

The file was plotted live with the help of GNUPlot:

```

#!/bin/sh
echo set grid
while true; do
    echo set yrang [-1000:1000]
    echo set xlabel "time, s"
    echo set ylabel "E, mV"
    echo plot <>(tail -n -1000000 &&
        data.dat | sed -e '$d' &&
        sed -e '1d' >)&&
        with lines lc rgb "red" notitle
    sleep 1
done

```

The GNU tools *sed*, and *tail* was used to plot the last 1000000 data points only, ignoring the last data point, which could be incomplete at the time the plotting command is issued.

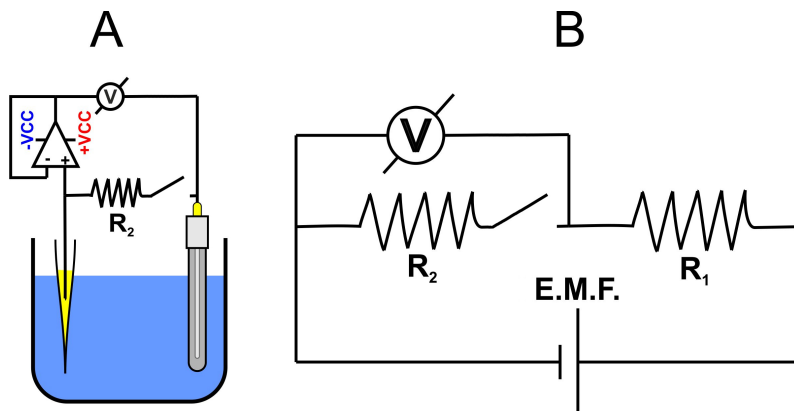


Figure 3.7: Voltage divider circuit to measure electrode resistance. The connection between the measuring and the reference electrodes through R_2 could be turned on and off with a switch.

3.1.3 Characterization of the microelectrodes

3.1.3.1 Calibration

For the micropipette ion-selective electrodes, calibration was performed in MgCl_2 and KCl dilution series, ranging from 10^{-6} M to 10^{-1} M . The measuring and reference electrodes were submersed sequentially in each solution from lowest to highest concentration. Potential was continuously measured against an $\text{Ag}/\text{AgCl}/3\text{M KCl}$ reference electrode with a high input impedance eDAQ pH/ISE isoPod USB (eDAQ Pty Ltd, Australia).

Metal/metal-oxide microelectrodes were calibrated by measuring their potential in nine buffer solutions. The typical calibration procedure was performed by introducing the microelectrode in a sequence of buffer solutions initiated with the most alkaline solution. In this way, the tip was exposed to solutions of increasing acidity.

3.1.3.2 Internal resistance

The voltage divider method was used to measure the resistance of the microelectrodes using $1 \text{ mM MgCl}_2 + 1 \text{ mM NaCl}$ solution. The electrochemical cell consisted of an $\text{Ag}/\text{AgCl}/3\text{M KCl}$ reference electrode and a freshly prepared microelectrode. The measuring electrode was connected to the voltage follower as shown in Fig. 3.7. After a steady reading was achieved, a precision resistor R was interconnected between the inputs of the voltage follower. The experiment was performed with two different precision resistors, namely 0.5 and $1.0 \text{ G}\Omega$.

The resistance of the antimony microelectrodes were also measured directly by attaching one probe of a high precision multimeter to the microelectrode, while submersing the other probe and the tip of the microelectrode into a beaker containing



Figure 3.8: The hanging drop method to measure response time. The tip of the measuring electrode is touching the ceramic frit of the reference electrode. They are both in contact with a small drop of solution that is hanging from the reference electrode. In this way, the potentiometric cell is intact even while the solution is being exchanged, and a sudden activity step can also be realized.

mercury.

3.1.3.3 Response time

The response time of the microelectrodes was measured by recording the response to a sudden change in ion activity. The method is based on a modified version of the dual drop cell method [88], called the „*hanging drop method*”. The tip of the measuring electrode was positioned in the close vicinity of the ceramic frit of the reference electrode. Both electrodes are in contact with the same drop of solution, that is hanging from the reference electrode. This arrangement is depicted in Fig. 3.8.

When the equilibrium potential was reached, the first solution was removed, and the surface of the second solution was slowly approached to the drop of the first solution hanging from the reference electrode, with the help of a laboratory stand with an adjustable height. When the surface of the second solution reached the drop of the previous solution, a sudden jump in ion activity was realized, corresponding to the difference between the ion activities between the first, and the second solution. This method was employed in the response characterization of the antimony microelectrodes.

To characterize the Mg^{2+} ion selective electrodes, they were immersed in a solu-

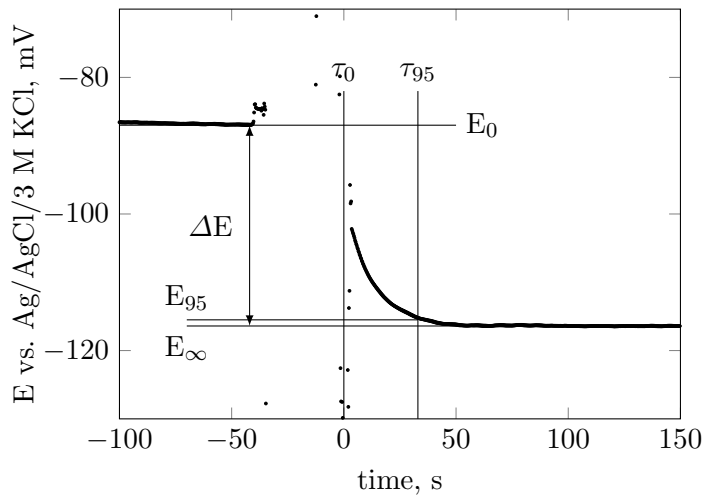


Figure 3.9: Illustration of the quantities used for the determination of response time. E_0 : electrode potential prior to change in the activity (of the measured ion), E_{eq} : equilibrium electrode potential after the change in activity. ΔE : total difference between E_{eq} and E_{eq} , E_{95} : electrode potential when 95% of the total change has occurred. τ_0 : time instance when the change occurs, τ_{95} : time instance when E_{95} is reached. $\Delta\tau_{95}$: difference between τ_{95} and τ_0 .

tion of 0.1 M MgCl₂ + 1 mM NaCl and then moved to the second solution of 0.01 M MgCl₂ + 1 mM NaCl after a stable potential was reached in about 3 minutes. The time needed to reach 95% of the total potential change caused by the change in Mg²⁺ ion concentration was regarded as response time τ_{95} (Fig. 3.9).

3.1.3.4 RC time constant

RC time constant was determined with two different methods. For the antimony and tungsten pH-electrodes, *RC* time constant was measured directly from the response curve using the activity step method. The transient response curve of the potentiometric cell was recorded while the buffer was changed from pH 6 to pH 4, then Eq. 4.2 was fitted on the curve. In the fitted function, *RC* is the only variable parameter, and can be directly obtained.

For the micropipette electrodes, a different method was used. Resistance and capacitance of the potentiometric circuit was measured individually. Resistance of the measuring electrode was determined with the voltage divider method described in the previous section. In this case however, an $R = 50 \text{ M}\Omega$ 1% precision resistor was inserted between the measuring and reference electrodes, then the cell potential difference was continuously measured in 10⁻² M MgCl₂ solution. After arriving at equilibrium potential difference, the resistor was removed, and the measurement was continued until a new equilibrium signal was reached. Electrode resistance can be

calculated with the formula

$$R_{ISME} = R \frac{E_{OCP} - U_R}{U_R} \quad (3.1)$$

where R_{ISME} is the resistance of the ion-selective microelectrode, R is $50\text{ M}\Omega$, E_{OCP} is the open circuit potential difference, and U_R is the potential difference between the electrodes while the resistor is introduced in the circuit.

The capacitance of the circuit is mainly due to the capacitance of the input amplifier, and the capacitance of the cable leading from the electrodes to the amplifier input. The capacitance of the amplifier input was measured by applying a low impedance -1.5 V step between the inputs of the amplifier through a $50\text{ M}\Omega$ resistor, and the time necessary to reach 63% of the total change in potential difference ($\tau = R \times C$) was measured. Then, the input capacitance could be calculated with the $C = \tau / 50\text{ M}\Omega$ formula.

3.2 SECM targets

With the exception of the micropipette ion source, the model targets were created by embedding graphite rods or metal wires or ribbons in an Epofix (Struers, Ballerup, Denmark) disk-shaped ($d \approx 3\text{ cm}$) epoxy resin sleeve.

3.2.1 Magnesium- and potassium-ion source pipette model targets

Spherical Mg^{2+} and K^+ ion concentration distribution was created in 10^{-3} M NaCl supporting electrolyte using simple model systems. They consisted of an embedded micropipette target facing upwards with a pore diameter of $d = 100\text{ }\mu\text{m}$, and filled with 0.1 M MgCl_2 and 0.1 M KCl aqueous solutions respectively, with an addition of 10^{-3} M NaCl and 4 % agar-agar to hinder diffusion (Fig. 3.10).

3.2.2 Moulded model targets

The model targets described here are prepared by moulding the samples with Epofix resin. The mould was prepared from cut-off portion of a Falcon-tube. The samples were placed upside down into the empty mould, then the resin was poured in. After curing, the front side – which was facing downwards during the curing process – was sanded off until the sample surfaces were exposed. Then, the surface was polished with sandpapers with increasingly higher grit, from 600 to 4000. Then polishing was continued with alumina slurry on wet polishing cloth. Alumina particle size was 1 μm , 0.3 μm and 0.05 μm . Finally, the surface was cleaned and degreased with absolute ethanol. Fig. 3.11 depicts a sketch of the model targets prepared with

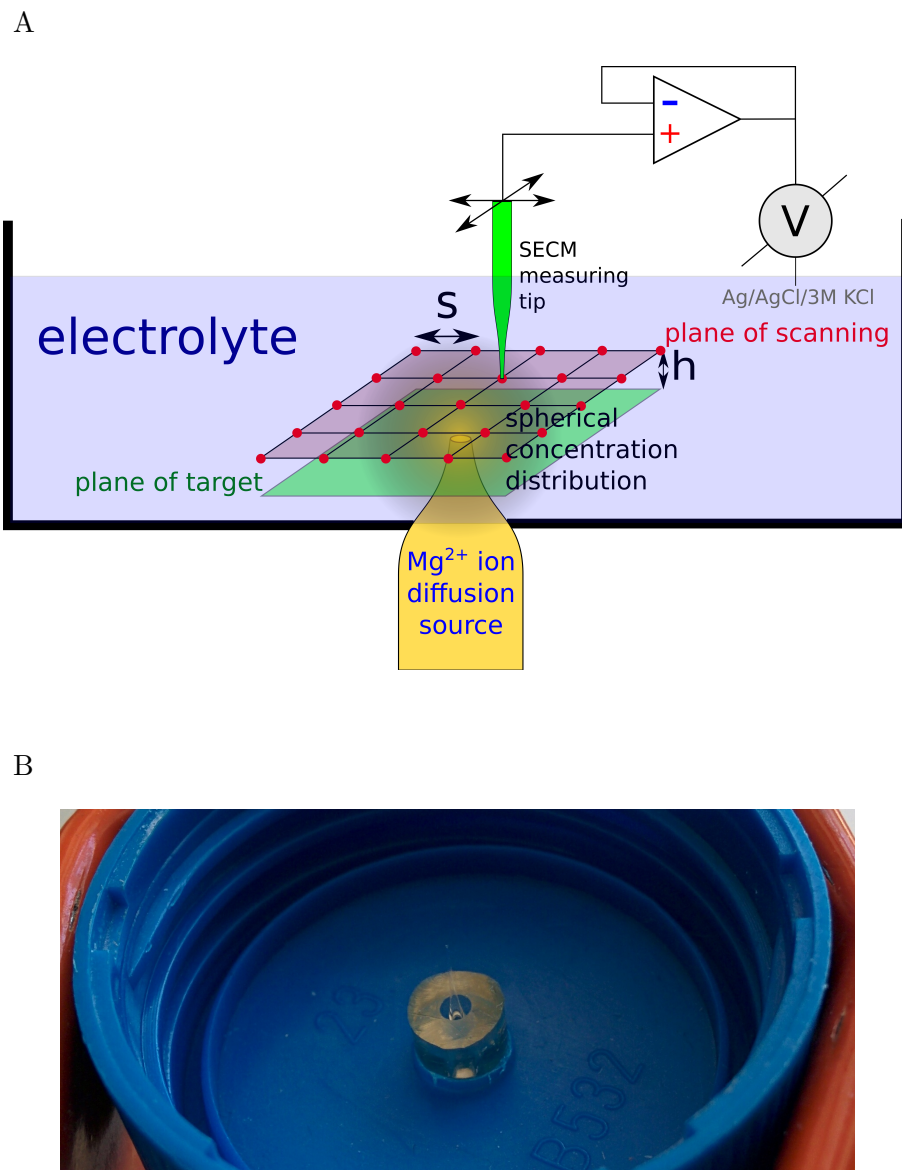


Figure 3.10: Sketch (A) and photo (B) of the model system with the embedded glass pipette Mg²⁺ or K⁺ ion diffusion source, and the SECM scan setup. "h" is height of scan, the distance between the plane of the target (pipette orifice) and the SECM tip. "s" is the step size, that is the distance between two neighbouring data aquisition points. Red dots indicate the data aquisition points of the 2D raster scan pattern. Not drawn to scale.

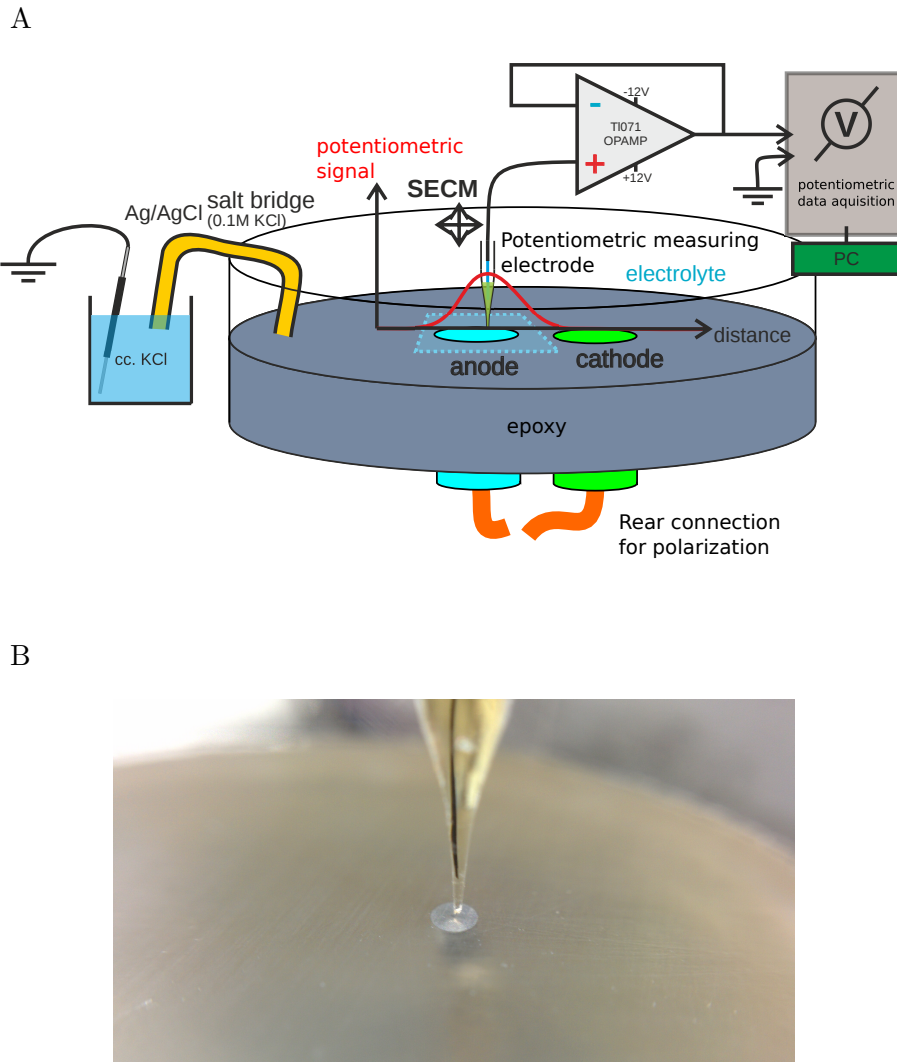


Figure 3.11: (A) Sketch of the moulded model targets and the SECM scan setup used for these targets. (B) Close-up photograph of the Mg^{2+} ion selective microelectrode above the AZ63 sample.

this method, and the SECM setup used with these targets. While scanning, the front side of the mount faced upwards, and was surrounded laterally by a PVC plastic tubing, creating a small container holding about 5 mL of test electrolyte solution, and a Ag/AgCl/3M KCl reference electrode. In this way, only the well-defined cross section of the samples were exposed to the electrolyte.

3.2.2.1 Iron – magnesium galvanic couple

A magnesium - iron galvanic couple was used as model corroding system. An iron wire with a diameter of 760 μm and a magnesium ribbon with a cross section of 200 $\mu m \times 800 \mu m$ were embedded in the Epofix resin disk. Corrosive electrolyte

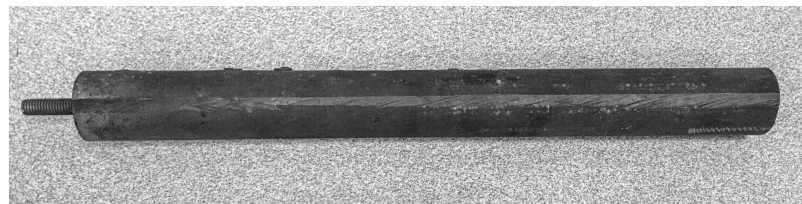


Figure 3.12: The water heater sacrificial anode made of the AZ63 magnesium-aluminium-zinc alloy. The sample was prepared from such an anode by a precision lathe.

was 1 mM NaCl.

3.2.2.2 Iron – AZ63 galvanic couple

Scans were also performed on an epoxy resin sleeve holding 760 µm diameter wires of pure iron and AZ63 magnesium alloy, manufactured from a boyler sacrificial anode with a high-precision lathe. The composition of the alloy was determined (in wt.%) by colleagues from the *University of La Laguna, Spain*, by emission spectrometry (ICP-OES): Al 5.74, Zn 2.88, Cu < 0.005, Fe < 0.005, Ni < 0.005, Si < 0.005, Mg balance. Tests were conducted in 1 mM NaCl solution, naturally aerated, and at ambient temperature.

3.2.2.3 Carbon steel

The embedded sample in this case was a carbon steel ($A \approx 0.2 \text{ cm}^2$) JIS G3131 SPHC specimen with the composition, C: 0.04%, Mn: 0.15%, P: 0.026%, S: 0.005%, and Si: 0.02%.

3.2.2.4 Graphite model target

To demonstrate and compare the new scanning algorithms, images of pH-dependent potential profiles were recorded $h = 100 \mu\text{m}$ above a graphite disc electrode, set to 2 V versus another, identical graphite electrode. $d = 350 \mu\text{m}$ mechanical pencil leads (Rotring, Hamburg, Germany) were used as graphite electrodes. They were both embedded in the epoxy resin sleeve. At this potential difference, pH of the electrolyte will decrease at the anode, and increase at the cathode, as a consequence of water electrolysis. Electrolyte was unbuffered 10^{-3} M NaCl solution. Potential image was recorded after 10 minutes of electrolysis. During the imaging, the electrolysis cell was disconnected to avoid the electric field generated by the applied voltage affecting the image. In this way a spherical concentration distribution is being generated above the target.

3.3 SECM routines

3.3.1 For the comparison of solid and liquid contact microelectrodes

2D scans were performed 100 μm above the micropipette and the magnesium ribbon target. Scanrate was 12.5 $\mu\text{m}/\text{s}$ in both cases. Step size in X and Y direction was 25 and 50 μm . Scanned area was 1000 $\mu\text{m} \times$ 1500 μm ($X \times Y$). Scanning probes were liquid and solid contact Mg^{2+} ion-selective micropipettes. A Sensolytics SECM system was used, potential was recorded with an Autolab Electrochemical workstation. The TL082 voltage based follower was inserted between the measuring microelectrode and the Autolab. Reference electrode was an $\text{Ag}/\text{AgCl}/3\text{ M KCl}$ electrode.

3.3.2 Optimization of scanning patterns and algorithms

3.3.2.1 Cartesian coordinate-system based patterns and algorithms

The three conventional scanning algorithms are the meander, the comb, and the fast comb. In meander, the probe travels through all of the raster coordinates without repetition and wasted movement, by alternating the X scan direction from line to line, resulting in a characteristic „meander” pattern. In the comb pattern, the probe sweeps through each scan line twice, back and forth, then the two scans are averaged. The fast comb algorithm scans only in one direction, and before advancing in the Y direction, the probe travels back to the beginning of the scan line without measuring or stopping at all.

In the meander, fast-comb, and comb algorithms, total scanned area was 2000 $\mu\text{m} \times$ 2000 μm , resolution was 100 $\mu\text{m} \times$ 100 μm , and consequently $21 \times 21 = 441$ raster points altogether.

Both in the experimental and simulated SECM scans, for each point, 1 second was split between probe movement, resting period, and signal sampling. One measurement was performed at every point after the resting period, before positioning the probe to the next point. Probe movement speed was 312.5 $\mu\text{m}/\text{s}$. The starting position was $x = -1000\text{ }\mu\text{m}$, $y = -1000\text{ }\mu\text{m}$.

3.3.2.2 Circular, polar-coordinate system based patterns and algorithms

The two new scanning patterns proposed in this thesis are called the „web” and the „arc” patterns. In the web pattern, sampling points are located on concentric circles with regularly increasing radius. On each circle, there are equal number of points. The first point in each circle has the angular coordinate of 0° , which increases at regular intervals with the rest of the points. Using this pattern, resolution

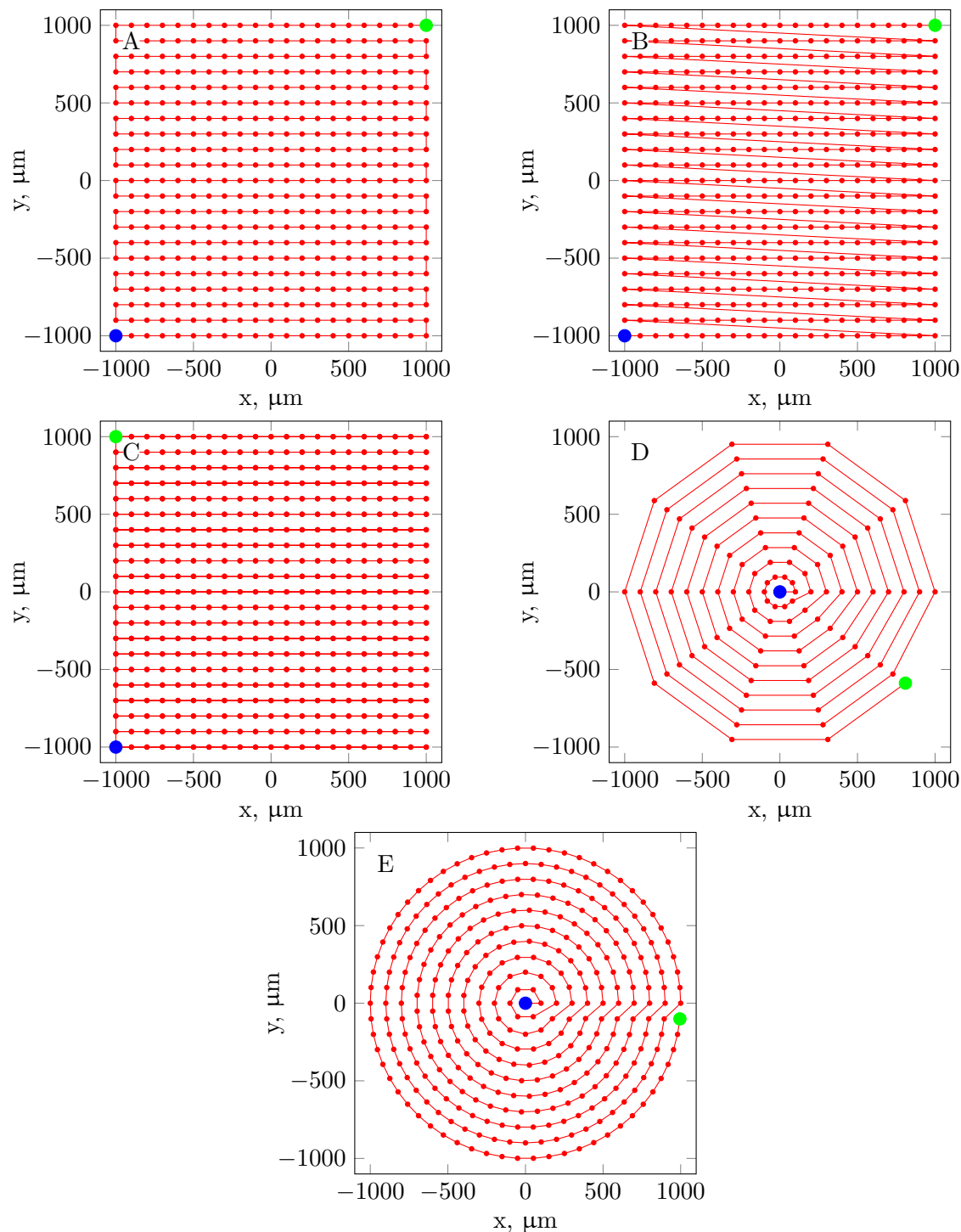


Figure 3.13: The conventional (A) meander, (B) fast comb and (C) comb, and the new, proposed (D) web, and (E) arc SECM scanning patterns for circularly symmetric targets. Red dots indicate sampling points, red line shows the probe path. Blue and green dots indicate starting and finishing positions, respectively.

decreases as radius increases. The arc pattern is very similar, except that the points on the circles are separated by equally long arcs, so that with increasing radius, the number of points increases, and resolution is maintained. The scanning patterns can be seen in Figure 3.13.

In the web algorithm, the radius of the scanned area was $r = 1000 \mu\text{m}$, with $\Delta r = 100 \mu\text{m}$, and $\Delta\alpha = 2\pi/10$ radians, resulting in 10 points on each circle, and a total of 110 points. In the arc pattern r and Δr was the same as in the web pattern, arc distance between adjacent points along the circles was $100 \mu\text{m}$, with a total of 341 points.

Starting position was $x = 0 \mu\text{m}$, $y = 0 \mu\text{m}$ relative to the target center for both algorithms.

The images obtained with the two polar coordinate-based algorithms were interpolated to the grid points of the 2D raster used by the other algorithms to allow similar visualization.

3.3.3 SECM routines for the deconvolution study

3.3.3.1 Linescans

To examine the effect of equilibration interval length on the image distortion, and for easy comparison of raw and deconvoluted data, line scans were recorded with three different time intervals allocated for each data acquisition point: 0.5 s, 2 s, and 5 s. Probe movement speed was $1000 \mu\text{m/s}$, and therefore probe movement interval was 0.1 s, resulting in equilibration interval lengths (t_e) of 0.4 s, 1.9 s, and 4.9 s, respectively. Step size was $100 \mu\text{m}$, scan distance was $2000 \mu\text{m}$ with the source center in the middle. 8 consecutive line scans (4 forward and 4 reverse scans) were performed in each case to confirm repeatability.

3.3.3.2 2D scans

To confirm the effect of deconvolution on 2D image quality, 2D raster scans were performed with four different equilibration interval lengths (4.9 s, 1.9 s, 0.9 s, 0.4 s), and two different scanning algorithms; the meander and the fast comb. In meander, the probe travels through all of the raster coordinates without repetition and wasted movement, by alternating the X scan direction from line to line, resulting in a characteristic „meander” pattern. The fast comb algorithm scans only in one direction, and before advancing in the Y direction, the probe travels back to the beginning of the scan line without measuring or stopping at all (paper IV).

Starting position was $X = -1000 \mu\text{m}$, $Y = -1000 \mu\text{m}$. Both algorithms used horizontal scanning. Initial scan direction for the meander algorithm, and scan di-

rection for the fast comb algorithm was left to right. Step size was 100 μm , scanned area was 2000 $\mu\text{m} \times 2000 \mu\text{m}$, resulting in overall scanning times of 2205 s, 882 s, 441 s, and 220.5 s.

In the experiments with the micropipette sources, the $X = 0 \mu\text{m}$, $Y = 0 \mu\text{m}$ reference position was established by positioning the measuring tip 100 μm above the orifice center of the diffusion source, with the aid of a camera. Then, the tip was positioned at the starting coordinates, and the electrolyte was introduced to the cell. 10 minutes later, the scan was started.

3.3.4 Backlash compensation

To rule out additional distortion caused by the SECM apparatus, backlash of the linear stages was measured and found to be below 1 μm after software compensation. To measure backlash, a microscope slide with a micrometer scale was fixed on the linear stage, then the stage was moved 1000 μm to one direction, to make sure the momentary backlash in that direction is zero. After taking a photo, the stage was moved 100 μm to the same direction, and another photo was taken. Then, the stage was moved 100 μm to the opposite direction, and a photo was taken again. The difference between the first and last photo is the backlash of the particular stage. Fig. 3.14 shows the photos for each stage of the home-made SECM.

3.4 Deconvolution of potentiometric SECM images

The potentiometric signal-time response function to change in analyte activity can be characterized with the time constant. It is the time required for the cell potential difference to change from its initial value by the fraction $1 - e^{-1} = 0.63$ of the final value [100]. The cell can be modeled as a simple RC low-pass filter arranged serially between the signal input and the output [63]. In this case, time constant is $\tau = RC$, where R is the resistance of the cell with the largest contribution from the measuring electrode, and C is the capacitance of the cell with the largest contribution from the input amplifier and the cable between the amplifier and the electrodes.

Eq. 4.2 describes the transient cell response when the measuring electrode is brought to contact with a solution of different analyte activity.

$$E_{cell}(t) = E_{cell}(\infty) + [E_{cell}(0) - E_{cell}(\infty)]e^{-t/RC} \quad (3.2)$$

where $E_{cell}(t)$ is the cell potential difference at time t , $E_{cell}(\infty)$ is the equilibrium cell potential difference, $E_{cell}(0)$ is the cell potential difference prior to the change.

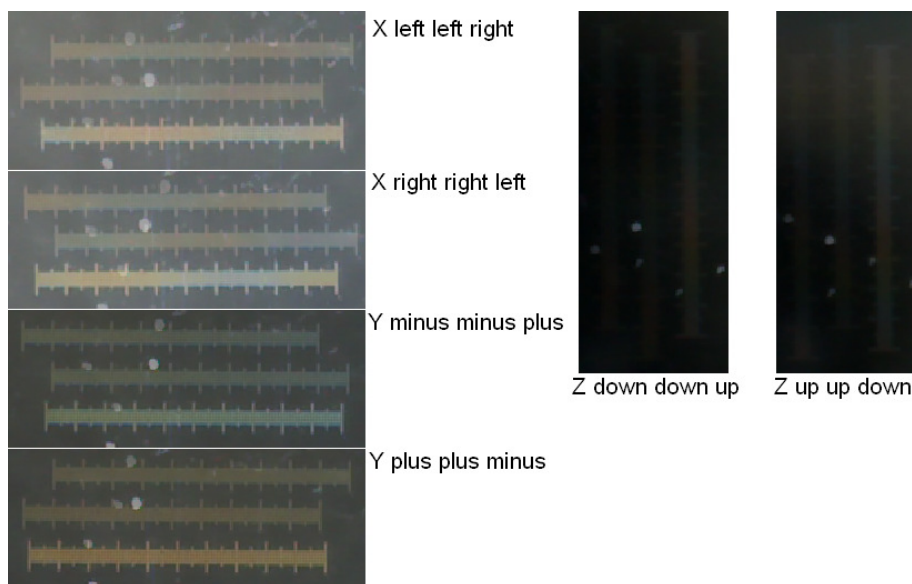


Figure 3.14: Microphotos for the backlash compensation measurements for the home-made SECM. The photos show a microscope slide with a micrometer scale fixed on the microelectrode holder. Labels ("left", "right") indicate the direction of the slide unit movement prior to taking the microphoto. First, the slide unit was moved 1000 µm, then a photo was taken. Then, it was moved 100 µm in the same direction, and another photo was taken. Finally, it was moved in the opposite direction 100 µm, and a photo was taken. The difference between the second and the third photo is the backlash, which was compensated through the control software.

From this, $E_{cell}(\infty)$ can be expressed as:

$$E_{cell}(\infty) = \frac{E_{cell}(t) - E_{cell}(0)e^{-t/RC}}{1 - e^{-t/RC}} \quad (3.3)$$

This can be used as a deconvolution function for potentiometric SECM images, substituting the time that elapses between two consecutive measurements in the SECM scan for t to calculate each equilibrium $E_{cell}(\infty)$ from the respective observed $E_{cell}(t)$ potential difference values.

When the tip advances from the i th data acquisition point to the $(i + 1)$ th, cell potential difference changes from the initial $E_{cell}(t, i)$ to $E_{cell}(t, i + 1)$. Therefore, for every point, $E_{cell}(0, i)$ will be equal to $E_{cell}(t, i - 1)$. To deconvolute the raw image, the following calculation kernel was cycled through the data matrix points in the same order as they were recorded in the scan:

$$E_{cell}(\infty, i) = \frac{E_{cell}(t, i) - E_{cell}(t, i - 1)e^{-t/RC}}{1 - e^{-t/RC}} \quad (3.4)$$

RC time constant in Eq. 3.3 was substituted with the value calculated from $R \times C$, obtained in the measurements described in the previous subsection. A FORTRAN program was written to perform the deconvolution:

```

program deconvolution
implicit none
integer :: i, j, stat
real rc, e0, conv
real t
rc=0.85
open(1, file='data.txt')
open(2, file='data_deconvoluted.txt')
read(1, *) i, j, e0
do
  read(1, *, iostat=stat) i, j, conv
  if (stat /= 0) exit
  write(2, *) i, j, ((conv - e0*rc)/(1-rc))
  e0=conv
end do
close(1)
close(2)
end program deconvolution

```

3.5 Simulation of the SECM measurements

3.5.1 3D numerical simulation of diffusion from a disk source

For the diffusion simulation, the „*point*” variant of the finite difference method was used as described in [101]. In potentiometric SECM, the tip is a passive probe, it does not generate or collect, therefore it does not alter the concentration profile of the species generated at the substrate. The model target can be implemented in simulation by a disk surface with a constant flux of the generated species, H_3O^+ . Since the probe is passive, the concentration profile is only affected by the magnitude of the flux, and the diffusion coefficient of the species. The time dependent diffusion problem is described by Fick’s Second Law of Diffusion:

$$\frac{\partial c}{\partial t} = D \nabla^2 c \quad (3.5)$$

where c is the concentration, t is time, D is the diffusion coefficient. For three dimensions, Equation 3.5 can be expressed in discrete form for solving with the finite difference method as

$$\frac{c'_{i,j,k} - c_{i,j,k}}{\delta t} = \frac{D}{h^2} (c_{i,j+1,k} + c_{i-1,j,k} + c_{i+1,j,k} + c_{i,j-1,k} + c_{i,j,k-1} + c_{i,j,k+1} - 6c_{i,j,k}) \quad (3.6)$$

where h is the distance between the adjacent points in space, $c_{i,j,k}$ is the concentration at the grid point with the coordinates of i, j, k , and $c'_{i,j,k}$ is the same, but in the previous cycle, at the time instance $t - \delta t$. This can be solved numerically for a given time instance by iterating Equation 3.6 on every point of a 3D matrix, which represents the diffusion system.

The simulation model consisted of a cubic diffusion field with an edge length of 20 mm, and a resolution of 10 μm on all three axes. The top and side faces had Dirichlet boundary condition with $c = 0$, representing the bulk solution. The bottom face had a disc shaped source with a diameter of $d = 350 \mu\text{m}$, with Neumann boundary condition, to model the graphite anode, where H_3O^+ was being generated. The rest of the bottom surface had Neumann boundary condition with a constant $j = 0$ flux, modeling epoxy resin which embedded the graphite electrolysis electrode. A FORTRAN program was written to calculate the potential profile for $t = 600$ s. A 2D section of the solved 3D diffusion matrix was taken at $h = 100 \mu\text{m}$, and it was normalized to c_{max} . This was the input matrix for the SECM scanning simulation.

3.5.2 SECM scan simulation

The SECM scan simulations were performed on a normalized 2D section of the solved 3D diffusion matrix. The following calculation kernel was cycled through the data points using the same scanning algorithms as in the experimental SECM scans:

$$C_i = c_i + (C_{i-1} - c_i) \times T \quad (3.7)$$

where C_i and c_i are the values of the i -th point in the output, and input matrices, respectively, C_{i-1} is the value at the previous point, at $i - 1$, and T is a constant, equivalent of expression $e^{-t/RC}$ in Equation 4.2. A value of 0.7 was set for T . For $i = 1$, C_i was set to c_i , assuming the potentiometric cell was in equilibrium in the beginning of the scan simulation.

3.6 Scanning Electrochemical Microscope

Throughout my work, I used three different SECM. One was supplied by Sensolytics (Bochum, Germany). The instrument was built around an Autolab (Metrohm, Herisau, Switzerland) electrochemical interface, controlled with a personal computer. Amperometric, potentiostatic and potentiometric operations were available in this configuration. A voltage follower based on a $10^{12} \Omega$ input impedance operational amplifier (TL082, Texas Instruments) was introduced in the measuring circuit. The cell voltages were measured with an electrometer and collected by the PC through the electrochemical interface. The scanning system (Applicable Electronics Inc, New Haven, CT, USA) used a 3D micropositioner driven by precision stepping motors. The distance between the scanning tip and the substrate was usually established by allowing the probe to gently touch the sample, and subsequently the probe was generally retracted to operation distance $100 \mu\text{m}$ with the aid of the Z-positioning motor. A video camera was used to further assist positioning of the tip close to the surface. Raster scanning was employed to record the consecutive scan lines composing the XY grid.

The other two SECM were custom built at the University of Pécs. While using these microscopes, potential was measured against an Ag/AgCl/3M KCl reference electrode with a high input impedance eDAQ pH/ISE isoPod USB (eDAQ Pty Ltd, Australia).

3.6.1 Homemade SECM

Two microscopes out of the three I used during my work are homemade. The first one was built from 3 Newport M-MFN25PP linear stages equipped with UE166PP

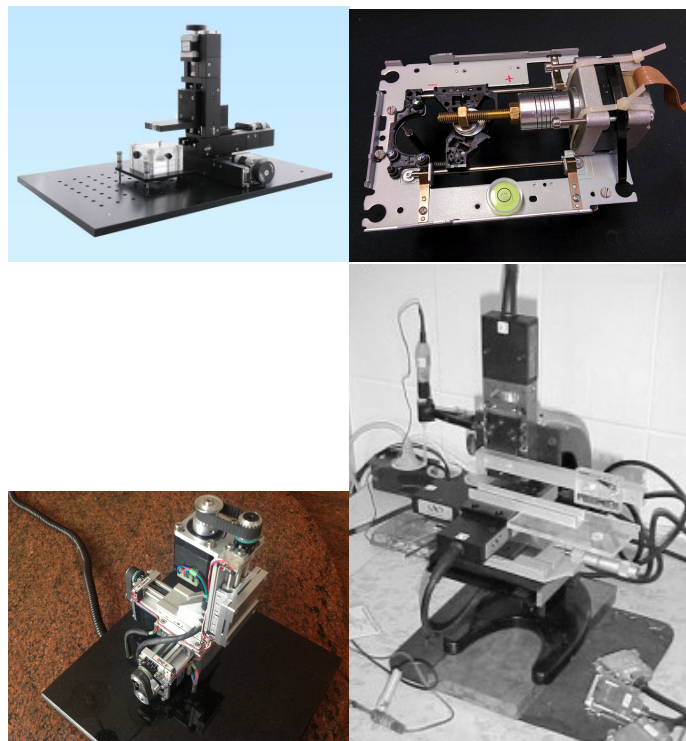


Figure 3.15: The Scanning Electrochemical Microscopes I used in my work. (A) Sensolytics SECM, (B) home-made SECM using Newport slide units, (C) home-made SECM using Domiline slide units driven with Nema 17 stepper motors, and (D) low cost, home-made 1D SECM using a slide unit from a DVD burner, driven by a stepper motor taken from a 5.25" floppy drive.

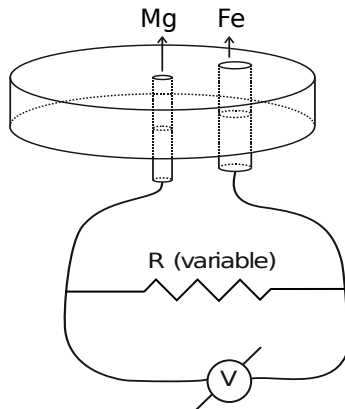


Figure 3.16: Circuit for measuring corrosion current between a galvanic couple.

stepper motors. Controller and driver was home-made from parts available in the local electronics store. The other SECM was built from Domiline 15 linear stages. Stepper motors for these were 3 Nema 17. Motors were coupled to the shafts by ribbed belts. It was controlled by a SD4DX USB Controller (Peter Norberg Consulting, Inc. 117 South Clay Ave. Ferguson, MO, USA), and driven by a Gecko step-and-direction driver board (Geckodrive, Inc. 14662 Franklin Ave, Santa Ana, CA.). The control software was written in Java.

3.7 Measuring corrosion current between a galvanic couple

Corrosion current can't be measured directly, since the measurement itself would alter the current. However, it is possible to calculate it by measuring the voltage drop on the two sides of a variable resistor, which connects the Mg and Fe samples together (Fig. 3.16). Plotting the voltage over the resistance (E/R) with respect to resistance, the "y," interception will be $1 / i$ at $R = 0$, after reciprocating, corrosion current is obtained. Using Faraday's law of electrolysis, Mg^{2+} ion flow rate from the Mg/Al sample was estimated.

3.8 Estimating ion-flux based on approaching curves

To estimate the flux of Mg^{2+} ions from the AZ63 sample, fixed height lateral scans and retracting scans were performed above the Mg sample, using solid contact Mg^{2+} ISME electrode as measuring tip, and Ag/AgCl/3 M KCl reference with a homemade SECM. Height of lateral scans was 100 μm , resolution was 5 μm , lateral distance was 5 mm with the Mg/Al sample in the centre. Retracting curves were recorded at $t = 10, 20, 30, 40, 50, 60$ minutes after introduction of the corrosive media, step size

was 5 μm . Since ionselective electrodes of this size have high resistance compared to the low input resistance of potentiometers, to avoid loading the potentiometric sensor, a homemade high impedance voltage follower circuit was used as current buffer based on the TL082 operational amplifier (Texas Instruments). The potential was measured with a MeTeX potentiometer (MeTeX M-3630D) connected to a PC, the signal was recorded with the software provided by MeTeX. Scans were performed with the galvanic pair both coupled, and uncoupled. Corrosive media was distilled water saturated with air.

Chapter 4

Results and Discussion

I've tried three approaches to alleviate the compromise between low distortion and short scanning time in the potentiometric SECM. The problem stems from the high RC time-constant. For a sufficiently small microelectrode, the resistance R can be so high, that the time-constant is measured in seconds. To arrive at the equilibrium potential of the measuring electrode, about $4 \times RC$ time must be allowed for the cell. Such high equilibration period is not practical, since a high number of sampling points must be included in the image raster to achieve the desired high resolution, and the $4 \times RC$ equilibration period must be waited at every sampling point. This means, for an image to be recorded with a step size of s (μm), image side length of L (μm), probe translation speed of v ($\mu\text{m}/\text{s}$), and an equilibration period of t_e (s), it takes t (s) time to complete the image, calculated with the following equation:

$$t = (L/s + 1)^2 \times (s/v + t_e) \quad (4.1)$$

Using the example from the "*Introduction*", if $R = 1 \text{ G}\Omega$ and $C = 500 \text{ pF}$, then $RC = 0.5 \text{ s}$, and $t = 882 \text{ s}$, or about 16 min, since about $t_e = 4 \times RC$ is necessary to obtain the equilibrium electrode potential with good approximation. To decrease the overall scanning time, there are a number of possibilities. If L or t_e is decreased or v or s is increased, then t is decreased. But, if the scanned area or resolution cannot be decreased further, then manipulating L and s is not a viable option. The parameters left are t_e and v . To decrease t_e and maintain image quality, RC must be decreased simultaneously. This is the first approach I took, and is detailed in Section 4.1.

In the second and third approaches I exploit the properties of the potentiometric response function:

$$E_{cell}(t_e) = E_{cell}(\infty) + [E_{cell}(0) - E_{cell}(\infty)]e^{-t_e/RC} \quad (4.2)$$

where $E_{cell}(t)$ is the cell potential difference at time t_e , $E_{cell}(\infty)$ is the equilibrium cell potential difference, $E_{cell}(0)$ is the cell potential difference prior to the change. The more different $E_{cell}(0)$ and $E_{cell}(\infty)$ are, the more the difference between $E_{cell}(\infty)$ and $E_{cell}(t_e)$ will be. Distortion of an image can be measured as an average of the differences between $E_{cell}(\infty)$ and $E_{cell}(t_e)$ at each point. It can be lowered by carefully optimizing scanning patterns and algorithms, so that the probe passes through borders between regions of high and low concentrations as few times as possible. This approach is detailed in Section 4.2.

In the third approach, I use the inverse of the potentiometric response function (Eq. 4.2) as deconvolution function. Since the relationship between t_e , $E_{cell}(0)$, $E_{cell}(t_e)$ and $E_{cell}(\infty)$ is known, a prediction for the only unknown $E_{cell}(\infty)$ can be calculated. This approach is detailed in Section 4.3.

Additionally, to increase the probe translation speed v and maximize the time available for cell potential equilibration (t_e), a custom SECM was built at our department, and used in the second and third approach. Increasing v has practical limitations, for a probe moving too fast between sampling points might stir the electrolyte. Scanning speeds of commercially available SECM devices however, haven't reached this limit, and are in the range of several tens of micrometers per second at best, due to hardware or software restrictions. With the custom built microscope, translation speeds up to 1000 $\mu\text{m}/\text{s}$ are possible.

4.1 Using solid-contact electrodes as potentiometric SECM probes

Solid-contact electrodes have lower resistance, compared to their otherwise identical, liquid-contact counterparts. This is due to two reasons. The solid contact can be pushed down very close to the micropipette orifice, shortening the thickness of the highly resistive ion-selective membrane, and decreasing the overall electrode resistance. The other reason is that instead of the internal solution – which has high resistance –, a modified carbon fiber – which has low resistance – is used as the ion-to-electron transducer. If R is lower, RC is lower, and the potentiometric cell becomes faster.

4.1.1 Electrode characterization and SECM images of a model system

I constructed two Mg^{2+} -ion selective electrodes. One used a liquid contact, and the other a solid contact. Besides this difference, they were prepared identically. Basic characterisation was performed for both. Fig. 4.1A and 4.1B shows the calibration plots for the liquid, and solid contact electrode, respectively. Sensitivities towards the primary ion (Mg^{2+}) were close to nernstian and very similar, 29.12 mV and 33.44 mV for the liquid and solid contact electrode, respectively. The solid contact electrode had a slightly wider dynamic range, reaching below 10^{-5} M. Selectivity coefficients, characterization of the potassium ion-selective electrode, and further characterization of the magnesium ion-selective electrode can be found in [102].

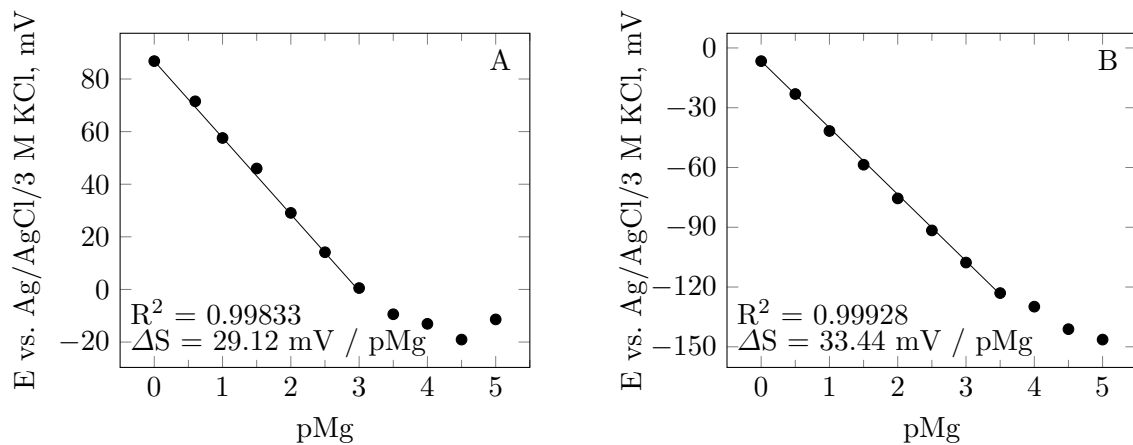


Figure 4.1: Calibration plots for the Mg^{2+} ISME in 1 mM NaCl solutions containing varying amounts of $MgCl_2$ ($pMg^{2+} = -\log_{10}[Mg^{2+}]$). (A) Liquid-contact, and (B) solid-contact.

Response characteristics were investigated by measuring the electrode resistance

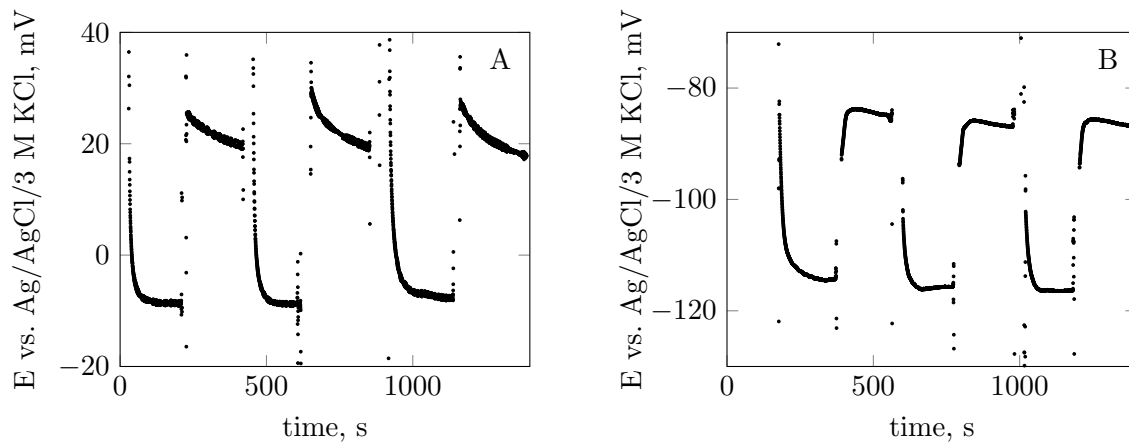


Figure 4.2: Dynamic response curves obtained for response time measurements to changes in MgCl_2 concentrations of 10^{-1} M and 10^{-2} M, in 10^{-3} M NaCl. (A) liquid-contact, and (B) solid-contact Mg^{2+} ISME.

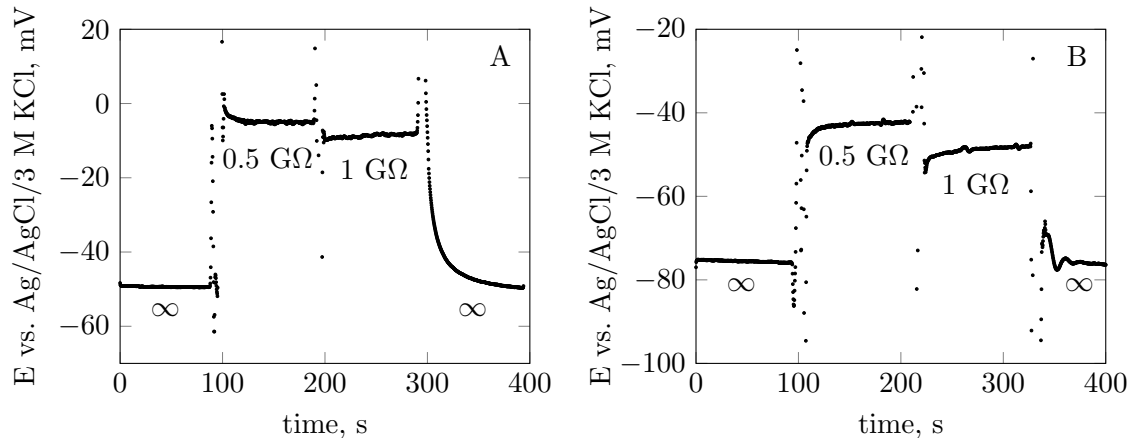


Figure 4.3: Response of ISME to shorting resistors for the voltage divider method: (A) Liquid-contact, and (B) solid-contact.

R , and the τ_{95} response time. The two parameters are related: $1 - e^{-3RC/RC} = 1 - e^{-3} \approx 0.95$. This means, that $3 \times RC \approx \tau_{95}$, because in $3 \times RC$, equilibrium electrode potential is reached by about 95%. Calculated from the voltage divider measurements (Fig. 4.2, Table 4.2), electrode resistance was $4.8 \text{ G}\Omega$ and $0.56 \text{ G}\Omega$ for the liquid, and solid contact electrodes, respectively. The measured τ_{95} parameters were 71.1 s, and 27.7 s, respectively (Fig. 4.3). Based on these values, the solid contact electrode was expected to produce less distorted images with the same scanning parameters.

To confirm it, a Mg^{2+} ion diffusion source model system was created, and the plane 100 μm above the pipette orifice was scanned with both electrodes. Fig. 4.4 shows the ISME images obtained using a liquid-contact (A), and a solid-contact (B),

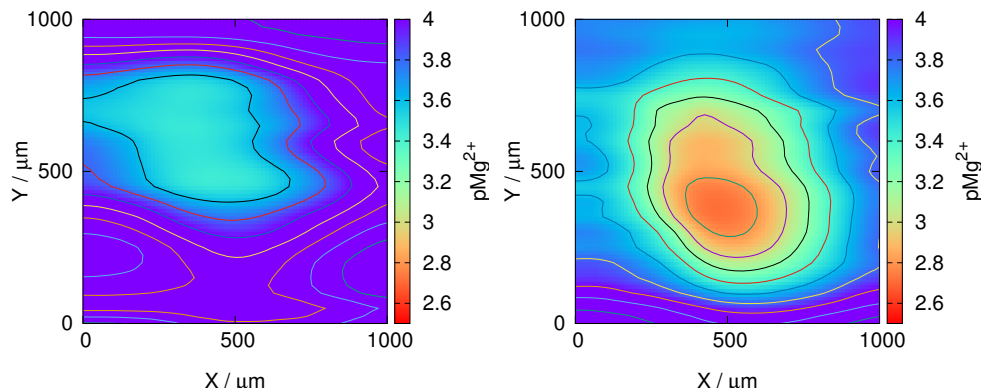


Figure 4.4: SECM images displaying the Mg^{2+} ion concentrations 100 μm above the tip of a centered pipette source. (A) liquid-contact, and (B) solid-contact. Scan rate: 12.5 $\mu\text{m}/\text{s}$.

micropipette electrode. Both 2D ISME maps were recorded at a scan rate of 12.5 $\mu\text{m}/\text{s}$. The same pipette holding the 0.1 M MgCl_2 agar solution was used in the measurements plotted in Figs. 4.4A and 4.4B. Visual inspection of the two images clearly shows significant image distortion in the X-direction with the liquid-contact ISME due its slower response as expected based on its higher resistance. It can also be observed in the image scanned with the solid-contact electrode, although to a much less extent. The overlayed isoconcentric countour lines are more circular, and not as elongated in the X-direction as in the case of the image prepared with the conventional electrode. Another important feature to note in the images is the difference in the highest magnesium ion concentration observed with the two electrodes. With the solid-contact microelectrode it's about $10^{-2.5}$ M. On the other hand, with the conventional liquid-contact electrode, highest observed magnesium ion concentration is only about $10^{-3.4}$ M. One possible reason for this is that the cell equipped with the liquid-contact electrode cannot keep up with the changes of the magnesium ion concentration at the micropipette orifice. That is, it passes over the area with the highest concentration so quickly, that by the time the cell would reach the potential corresponding to that concentration, the probe is already at another location, with a lower concentration. Potential starts dropping, while it approaches the new equilibrium potential.

4.1.2 Applications

4.1.2.1 Investigation of galvanic and homogeneous corrosion of magnesium

In paper (II), we used the Mg^{2+} ion-selective electrodes to image Mg^{2+} ion concentration above the corroding samples and compared the results. Based on the

Table 4.1: Resistance measurements for the two kinds of Mg^{2+} ion-selective micropipette electrodes conducted in 1 mM $MgCl_2$ 1 mM NaCl solution.

Parameter	ISME	
	Liquid-contact	Solid-contact
E_{OCP} / mV	-49.5	-75.5
R / GΩ	1	1
U_R / mV	-8.53	-48.41
R_{ISME} / GΩ	4.80	0.56

pipette source model target experiment and the resistivity measurements, it was expected that the cell equipped with the solid-contact electrode would yield less distorted images. Fig. 4.5 shows the four scans. Inspecting the images about the uncoupled magnesium (Fig. 4.5A1-A2), it is clear that the image scanned with the liquid-contact electrode is more distorted. The individual scanlines are blurred in the X direction, just like in the previous experiment with the pipette source. The same can be said about the images of the galvanically coupled magnesium. The one scanned with the solid-contact electrode is less distorted. Also, higher peak values can be observed, corresponding to magnesium dissolution. These anodic spots are resolved much better by the solid-contact electrode.

4.1.2.2 Estimation of corrosion current based on vertical SECM scans

Mg^{2+} ion concentration profiles above the Mg sample were recorded by SECM scans. Vertical Mg^{2+} ion concentration distribution was determined at different instants in time of the corrosion process, with, and without coupling the Mg/Al and Fe samples. About ten times more Mg^{2+} is being formed with coupling. Mg^{2+} concentration was increasing with time above the sample while coupled, on the other hand, it was decreasing after 10 minutes while not coupled (Fig. 4.6A). Based on the method of Scott and White [103], using the Mg^{2+} concentration profiles, Mg^{2+} flow rate from the Mg piece was possible to estimate:

$$\Omega = 4DC_s a \quad (4.3)$$

where Ω is the amount of Mg^{2+} released from the disc shaped Mg/Al surface, D is the diffusion coefficient of Mg^{2+} , C_s is the surface concentration of Mg^{2+} (at the height $z = 0$ μm), a is the radius of the Mg/Al sample. As the only unknown variable in the equation above, Ω could be calculated. Substituting the value of $D = 7.06 \times 10^{-8} \text{ dm}^2 \cdot \text{s}^{-1}$ [104], $C_s = 3.29 \times 10^{-2} \text{ M}$, $a = 0.0038 \text{ dm}$, the result is $\Omega = 3.53 \times 10^{-11} \text{ mol} \cdot \text{s}^{-1}$.

Corrosion current between the Mg/Al sample and four Fe samples with different

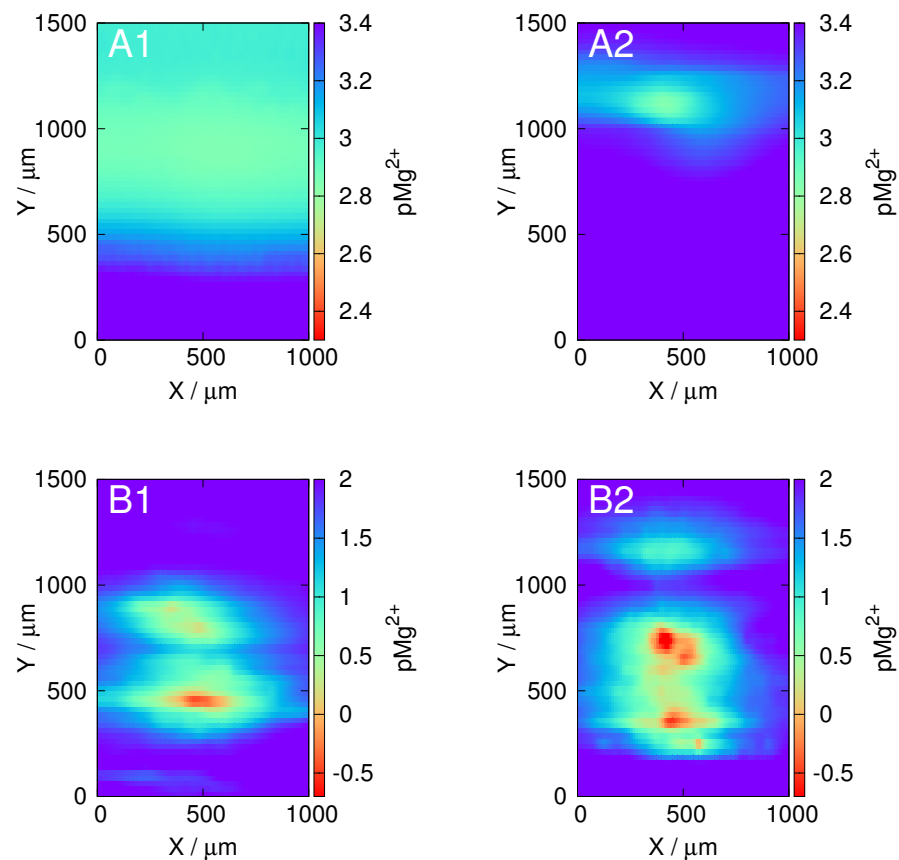


Figure 4.5: SECM scans above the magnesium sample (A) uncoupled, and (B) galvanically coupled to the iron sample, while the cell was equipped with the conventional (1) liquid contact, and the new, (2) solid contact micropipette. Scans were performed with the Sensolytics SECM, with impedance matching provided by the TL082 based voltage follower. Reference electrode was Ag/AgCl/3M KCl. Height of scan was 100 μm , scanrate was 12.5 $\mu\text{m}/\text{s}$.

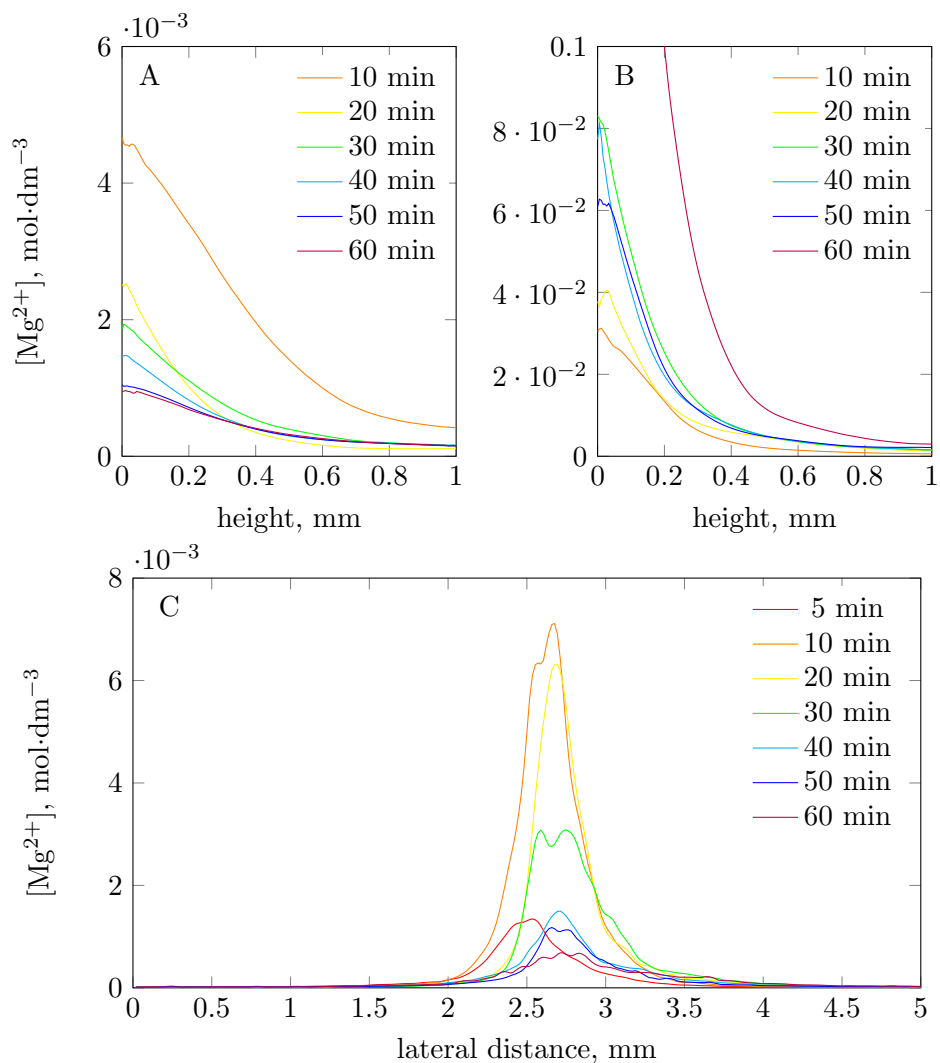


Figure 4.6: Retracting and lateral SECM linescans above the AZ63 magnesium-aluminium-zinc alloy sample initiated at different instances in time. Scan rate: 10 $\mu\text{m}/\text{s}$.

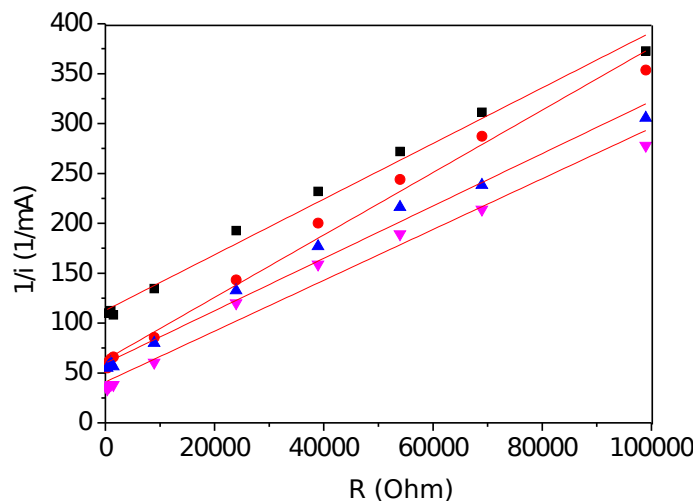


Figure 4.7: $1/i$ plots used for the determination of corrosion current between the AZ63 magnesium-aluminium-zinc alloy and various iron samples of different diameters. Diameter of the iron cathodes; black rectangle: $d = 0.59$ mm, red circle: $d = 0.76$ mm, blue triangle $d = 1.2$ mm, purple upside-down triangle: $d = 2.3$ mm.

diameters was also measured directly. As expected, current gets higher with increasing diameter. Corrosion current was $8.87 \mu\text{A}$, $15.83 \mu\text{A}$, $16.72 \mu\text{A}$, $24.4 \mu\text{A}$ with Fe sample diameters of 0.59 mm, 0.76 mm, 1.2 mm, 2.3 mm, respectively (Fig. 4.7). Using Faraday's law of electrolysis, this means, that $8.20 \times 10^{-11} \text{ mol Mg}^{2+}$ is being dissolved in every second from the Mg/Al sample ($\Omega_{0.76\text{mm}} = 8.20 \times 10^{-11} \text{ mol/s}$). This result is in fairly good agreement with the SECM measurement ($\Omega = 3.53 \times 10^{-11} \text{ mol/s}$). Ion flow rates from Mg/Al samples coupled with Fe samples of different diameters are proportional with the surface area of the sample; $\Omega_{0.59\text{mm}} = 4.60 \times 10^{-11} \text{ mol/s}$, $\Omega_{1.2\text{mm}} = 4.66 \times 10^{-11} \text{ mol/s}$, $\Omega_{2.3\text{mm}} = 1.26 \times 10^{-10} \text{ mol/s}$.

4.2 Optimization of scanning algorithms

4.2.1 SECM simulations

To obtain high quality images in scanning probe microscopy, a certain amount of scanning time is required, depending on the number of sampling points, and the scanning speed. Usually, there is a compromise between scanning speed and image quality. This is most critical in the potentiometric scanning electrochemical microscopy, which is severely limited by the relatively long response time of the ultramicro-electrode probes. That is, scanning speed can be increased only at the expense of image quality.

In a great majority of the SECM studies, the subjects are circularly symmetric systems. In this section, I present a method to increase SECM imaging speed of such systems, while improving image quality at the same time. It is achieved by using new, polar coordinate-based scanning patterns, exploiting the symmetry of the studied system, and using imaging time more economically. This technique significantly improves the imaging of circularly symmetric targets.

Numerical simulations and SECM scans using the traditional, and the new scanning algorithms have been performed. The resulting images have been compared with the expected, ideal image.

First, SECM scanning simulations were performed and the resulting images were compared (Figure 4.8). It was expected that the new, polar coordinate-based scanning algorithms would yield less distorted images than the traditional, raster-based algorithms. Not only the two new algorithms finish faster, but result images with lower distortion (Table 4.2). Mean squared error is 9.63×10^{-3} and 2.95×10^{-3} for the images scanned with the web and the arc algorithms, respectively. In comparison, mean squared error for the images scanned with traditional meander, fast-comb, and comb algorithms are 2.75×10^{-2} , 2.07×10^{-2} , and 2.75×10^{-2} , respectively.

4.2.2 Experimental SECM images

Next, the experimental SECM scans were performed, with the same scanning algorithms as the simulations were. The results (Figure 4.9) confirmed our presumption, that using the two new algorithms, images have less distortion, with higher similarity to the expected image.

Considering scanning time also, which are 440, 520, and 881 seconds for the meander, fast-comb, and comb algorithms, and 109, and 340 seconds for the web, and arc patterns respectively, it can be said, that the new scanning algorithms proposed in this paper shorten scanning time, and significantly improve imaging quality of circularly symmetric systems. There are two additional advantageous properties of

the new algorithms. First, data is gathered in order of decreasing relevance, from closest to the target, to farthest from the target, without the corners of the rectangular raster patterns, which are of less importance, because of the larger distance from the target. Second, with the new algorithms, there is only positive imaging distortion (Figure 3.13I, J). The observed potential, for a perfect hemispherical concentration distribution, in theory, cannot be lower above the center than the maximum value. It also cannot be higher, since the probe starts scanning in the center, where $E_{cell}(t) \approx E_{cell}(\infty)$ (Equation 4.2). But positive distortion can occur as the probe leaves the close vicinity of the target, advancing towards coordinates with lower concentration. This has an importance when accurate quantitative information is required about the concentration distribution above the target, such as in estimating fluxes by fitting simulation to measured images [45, 105].

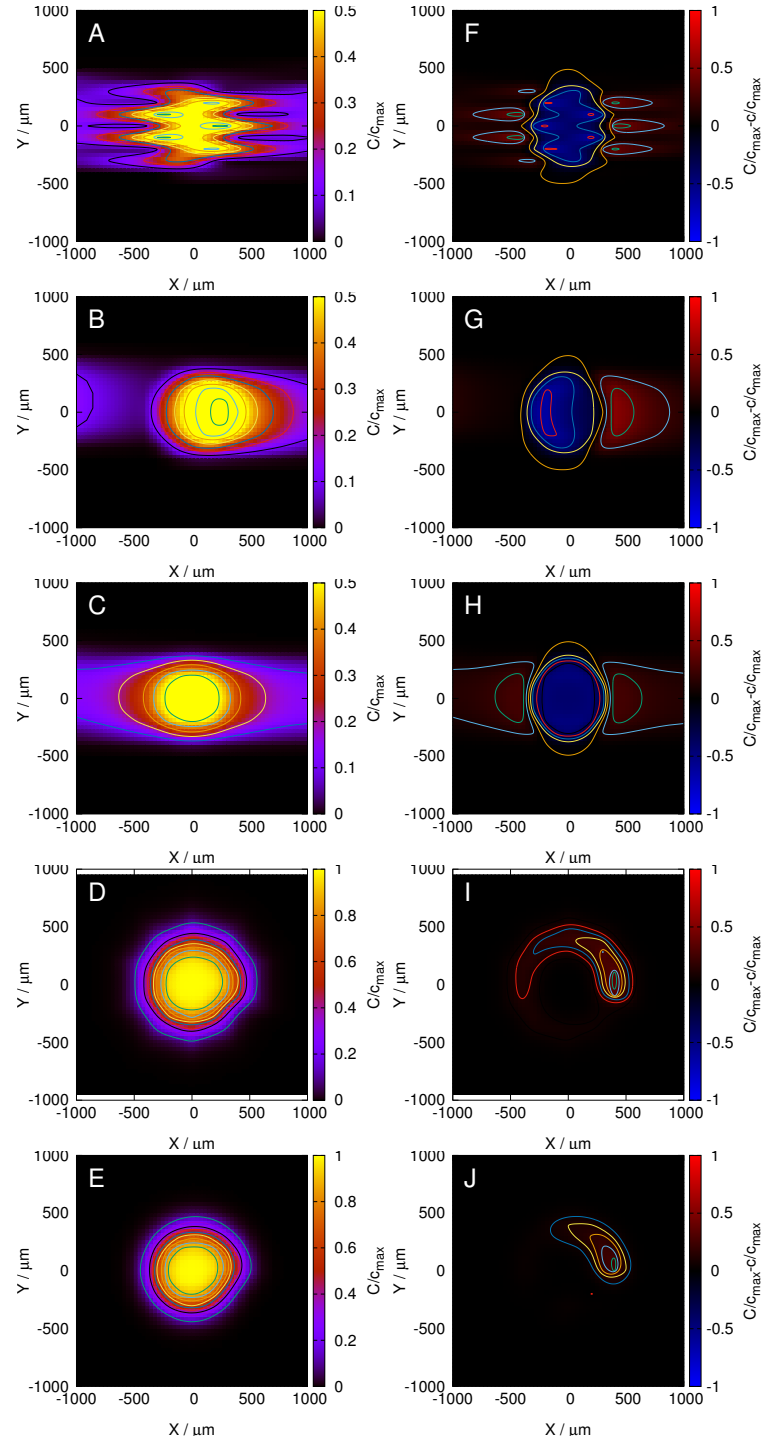
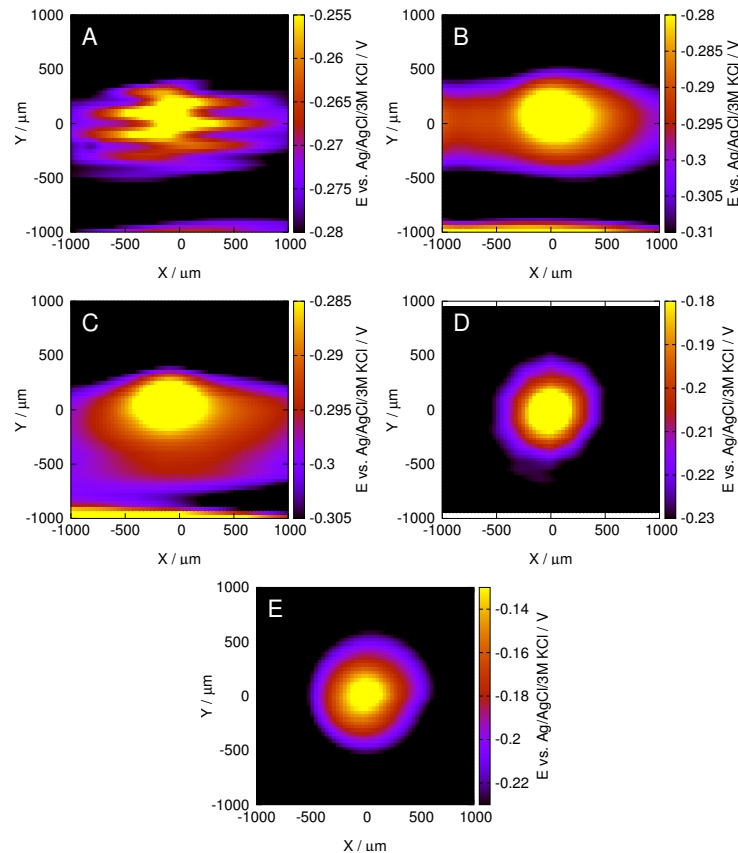


Figure 4.8: (A-E) Simulated SECM scans 100 μm above the disc source with the meander, fast comb, comb, web, and the arc scanning algorithms, respectively. All images were normalized to the maximum concentration of the expected image (c_{max}). (F-J) Deviation from the expected concentration image using the meander, fast comb, comb, web, and the arc scanning algorithms, respectively. „C” is the input (expected concentration profile), „c” is the output (observed concentration profile) matrix for the scan simulation.

Table 4.2: Comparison of the scanning algorithms.

Algorithm	Number of sampling points	Total scan time (s)	Mean squared error
Meander	441	440	2.75×10^{-2}
Fast comb	441	520	2.07×10^{-2}
Comb	441	881	2.75×10^{-2}
Web	110	109	9.63×10^{-3}
Arc	341	340	2.95×10^{-3}

**Figure 4.9:** Experimental SECM scans 100 μm above the disc source with the (A) meander, (B) fast comb, (C) comb, (D) web, and (E) the arc scanning algorithms. Measuring electrode was a pH-sensitive antimony micro-electrode. Potential was measured against an Ag/AgCl/3M KCl reference electrode.

4.3 Signal processing in potentiometric SECM

4.3.1 Deconvolution of measurements performed with metal/metal-oxide microelectrodes

In order to image rapidly changing systems with the Scanning Electrochemical Microscope, high scan rate must be used, otherwise by the time the scan is completed, major changes in the studied system would have occurred. But if the scan rate is too high, there is not enough time for the detector to reach equilibrium before the signal is recorded at a given data acquisition point, and the image will be distorted. This is a problem especially in potentiometric SECM, where the long response time of the potentiometric cell using ultramicro electrode probes imposes a limit on the maximum scan rate. In this section I demonstrate that high scan rates combined with signal processing can be used in potentiometric SECM to keep scan time to a minimum, and still obtain high quality results by deconvoluting the raw, distorted image. Model systems were studied with high scan rate, then the images were deconvoluted using the inverse of the potentiometric response function to calculate the equilibrium value for each data acquisition point from the respective observed values.

Deconvolution of measurements obtained with the metal/metal-oxide electrodes (antimony/antimony-oxide, and tungsten/tungsten-oxide) are attempted. First, a simple step response, then 1D linescans, and finally 2D raster images were deconvoluted, using four different electrodes; pH sensing microelectrodes made from antimony and tungsten, and ion selective microelectrodes for magnesium and potassium ions. This method has been already proposed in 1981 to determine the response time of potentiometric cells, based on the initial portion of the response curve, since it holds the same information. However, the authors of the paper about that method didn't go any further with their proposition. As Lindner and his coauthors write in [106]:

„This new definition [of response time] has several advantages in contrast to the earlier propositions and accepted definitions: it does not require the knowledge of the equilibrium potential value (E_∞); it holds the same sort of information as the time constant of a theoretical equation; it can be used in the case of response time curves consisting of different sections, e.g., even for rapid kinetic studies when $t \approx 0$ (6), and in practice it helps the analysts in determining when potential readings are to be taken. Accordingly to eliminate subjective errors in readings, one can regard the potential value corresponding to a limiting slope (dE/dt) as the steady-state

or equilibrium value. This idea is realized in some pH meters produced by Radelkis (Hungary) in which a so-called slope controller is built in (16).¹

4.3.1.1 Minimal working example: deconvolution of a step response

The „minimal working example” method, originally used in programming, is a way of tracking down problems, and finding the cause of certain behaviour. The most important feature of a minimal working example is that it is as simple as possible, such that it is just sufficient to demonstrate the problem, but without any additional complexity which would make resolution harder. In this case, the minimal working example is a simple step function: the activity of the primary ion is changed suddenly, while the response of the potentiometric cell is recorded. The input of the system is a step function, the output is the recorded signal, an exponential decay function. If there is no additional distortion, and the transfer function is simply Eq. 3.3, the square step should be restored.

To measure the time-constant of the potentiometric cell employing the antimony microelectrode, the transient response curve was recorded while the pH = 4 buffer solution was changed to pH = 6. Then, Eq. 4.2 was fitted on the curve (Fig. 4.10). Based on the fit, time constant of the cell is $\tau = 3.76$ s, and $e^{-0.5\text{ s}/3.76\text{ s}} = 0.8755$, which means, only 12% of the total change occurs in 0.5 s ($1 - 0.8755 = 0.1245$).

The deconvolution of the very same recording was performed with several different time-constants, including that obtained from the response curve. Fig. 4.11 shows the results of those deconvolutions. As expected, the recording becomes most similar to the step function when the measured RC time-constant is used. When a higher value was substituted into Eq. 3.3, the recorded potential was underestimated, and the deconvolution recovered more than necessary. If a lower value was used, the cell was assumed to be faster than it actually was, and the deconvoluted potential values did not reach the equilibrium values. To see the effect of using a time constant other than the one that was obtained from the fit, statistics was performed on the deconvoluted data. Mean squared error was calculated by first taking the difference between the input function and the deconvoluted function at every time instance. Then the square of those differences was averaged. The input function was defined as

$$E_{cell}(t) = \begin{cases} -183.18 \text{ mV}, & \text{if } t < 50 \text{ s} \\ -280.20 \text{ mV}, & \text{if } t \geq 50 \text{ s} \end{cases} \quad (4.4)$$

¹(6) refers to [107] and (16) refers to [108]

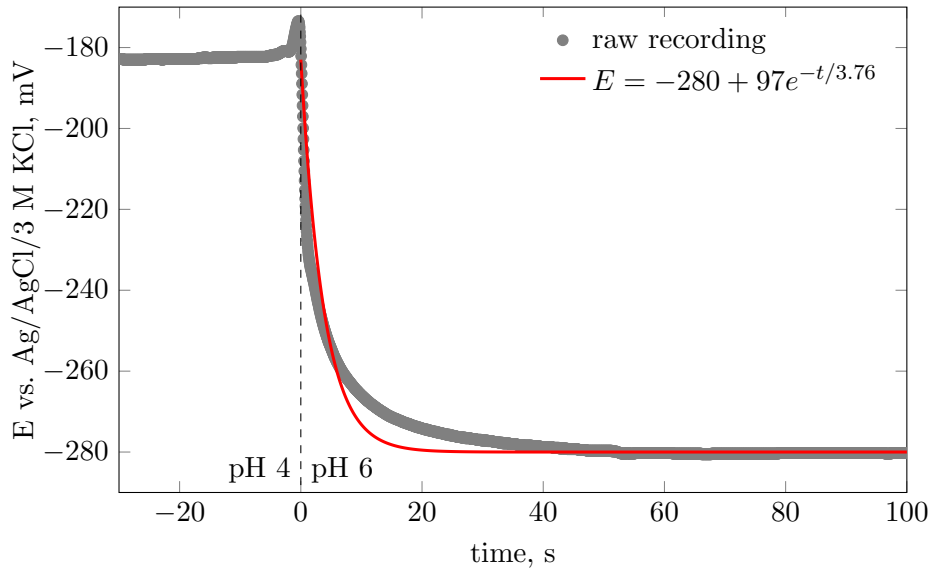


Figure 4.10: Transient response of the antimony microelectrode to analyte activity step. The measuring and reference electrodes were dipped into buffer solutions with pH = 4 before the measurements started, and pH = 6 at t = 0 s, respectively. Eq. 4.2 was fitted (red line) on the measurement (gray marks) from the pH step to the end of the curve when potential reaches equilibrium in the pH = 6 buffer.

The values for initial ($E_{cell}(0) = -183.18$ mV) and equilibrium ($E_{cell}(\infty) = -280.20$ mV) potentials were obtained by averaging certain portions of the recorded signal: the average from 0 to 49 s is -183.18 mV, and the average from 60 to 80 s is -280.20 mV. 4.4 should be obtained experimentally if the potentiometric cell was infinitely fast, and RC would be 0.

Table 4.3 shows the results of the statistical evaluation. Mean squared error rapidly increases when instead of the measured time constant, smaller or larger values were used in the deconvolution.

Table 4.3: Comparison of the deconvoluted time-potential recordings with different assumed time-constants, including the measured value (highlighted in bold).

$e^{-0.5/RC}$	$RC(s)$	Mean squared error
raw recording (0)	raw recording (0)	53.43
0.7	1.4	22.03
0.75	1.74	15.88
0.8	2.24	9.01
0.8755	3.76	3.83
0.9	4.75	16.99
0.95	9.75	781.94

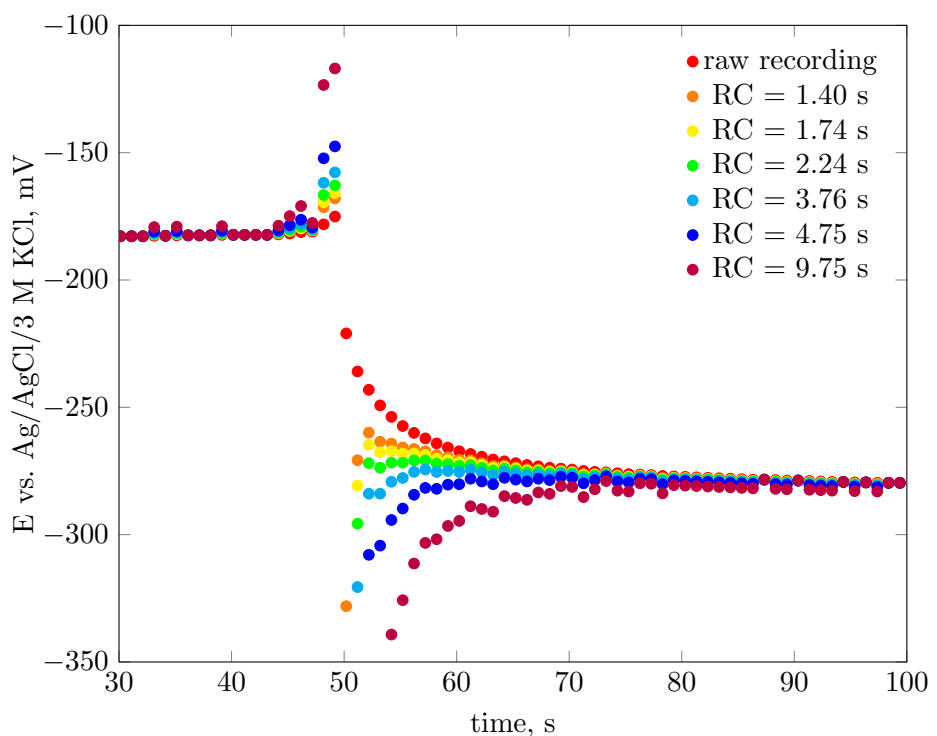


Figure 4.11: Transient response of the antimony microelectrode to analyte activity step (red), and deconvolutions performed with different assumed RC time-constants (orange-purple). The measured time-constant was $\tau = 3.76$ s (cyan). The measuring and reference electrodes were dipped into buffer solutions with $pH = 4$ and $pH = 6$ respectively.

4.3.1.2 Investigation of possible surface processes

There are two interesting properties of the fit in Fig. 4.10. to be noted. First, the fitted curve is slightly different than the recorded response. The initial part of the measurement seems to be changing faster than it is expected from an RC circuit with a time-constant of 3.76 s, while the second part (from around 7 s) has a lower rate of change compared to the model. This means, that the transfer function is more complicated than Eq. 3.3, and the process cannot be properly described by simple potentiometric step response function. The effect of this behaviour can be observed in the first few data points of the deconvoluted measurement: there is a small overshoot compared to the equilibrium potential, even in the one that was deconvoluted with the measured RC . It was observed in all of the measurements, and the error was certainly carried through to all of the deconvoluted images, when the original measurement was performed with the antimony microelectrode.

The second discrepancy is that the RC determined in the previous section implies a very high resistance ($\text{G}\Omega$ range). It is possible to estimate the resistance of the antimony microelectrode from the specific resistance and the geometry of the antimony wire. Diameter, as mentioned in the chapter „Materials and Methods”, was 30 μm , length of the antimony wire was around 5 cm. Specific resistance of antimony is 417 $\text{n}\Omega\text{m}$ (at 20 °C) [104]. Then, resistance could be calculated as $R = 417 \text{ n}\Omega\text{m} \times 0.05 \text{ m} / ((15 \mu\text{m})^2 \times \pi) = 29.50 \Omega$. It must be noted however, that the measured resistance is a property of the whole cell, not just the microelectrode. Resistance of the reference electrode and the solution are included. Nevertheless, the difference between the estimated and the measured values is still too high. The very significant deviation from the expected value just calculated can be explained by a discontinuity defect in the antimony electrode, although it is unlikely, since all of the antimony electrodes appeared to have such a high resistance.

To verify that there was no discontinuity in the antimony microelectrodes, their resistance was measured directly by attaching one probe of a high precision multimeter to the microelectrode, while submersing the other probe and the tip of the microelectrode into a beaker containing mercury. Several electrodes has been tested this way, and their resistance never exceeded 20 Ω . The typical value was around 12 Ω , comparable to what was calculated from the electrode geometry and specific resistance of antimony.

Then, resistance of the whole cell was measured with the voltage divider method. Open circuit potential was -219.9 mV , while potential difference while the terminals were shorted through a $200 \text{ k}\Omega$ precision resistor was -105.0 mV . Resistance based on this result is $218.86 \text{ k}\Omega$, which is the sum of the resistances of the microelectrode, the reference electrode, and the solution. This resistance is still not large enough to

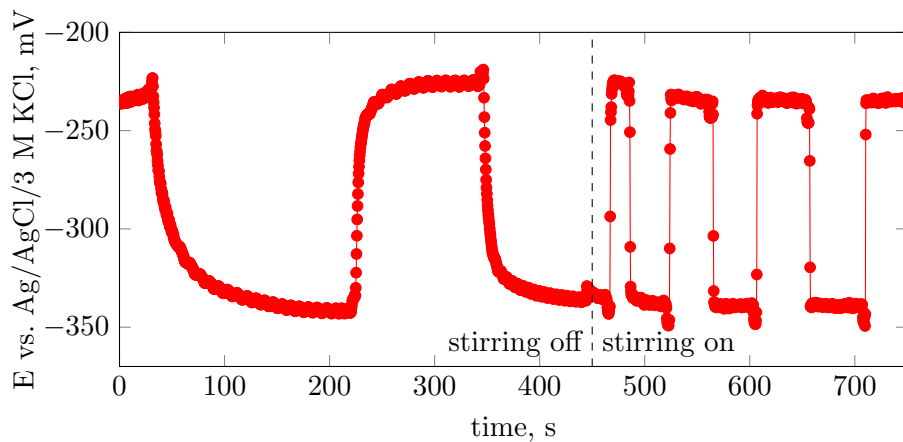


Figure 4.12: The effect of stirring on the antimony microelectrode. The buffer solutions were quickly changed back and forth between pH = 4 ($E \approx -240$ mV) and pH = 7 ($E \approx -340$ mV). Stirring was turned on at $t = 450$ s. To realize a quick change of the buffer solution without interrupting the potentiometric circuit, the „*hanging drop method*“ was used. For this experiment, the Arduino-based home-made DAQ was used.

explain an RC time constant of 3.76 s, since then the capacitance should be 17.2 μF , but it was in fact 11.15 nF (see section 4.3.2.1.).

Another way it could be explained is that there is a strongly adhered laminar layer (Prandtl-layer) on the surface of the electrode, and the exchange of this layer in a new solution is the slowest process as it is discussed by Lindner et al. in [109]. To test this hypothesis, step response measurements were carried out in unstirred and stirred buffers. The measuring electrode in this case was a large ($d = 1$ mm) antimony disc electrode, with a silver/silver-chloride quasi-reference electrode separated by 1 mm of epoxy resin. Because the antimony surface is much larger than in the case of a microelectrode, a more delayed response can be expected in the unstirred case, if there is indeed an adhered layer on the surface. By stirring the buffers when they are exchanged, the time constant should be the much lower RC time constant, with $R = 218.86 \Omega$.

Indeed, the response is much more delayed than in the case of a microelectrode, which can be observed in the response curves. The cell employing the microelectrode had an almost 100% response in about 1 minute (Fig. 4.10), while with the macro-electrode \sim 100% response was reached in about 200 s (first part of the curve in Fig. 4.12.). After stirring was turned on, the cell responded almost instantaneously (Fig. 4.12) to analyte activity step (that is depicted by the second part of the curve, after 450 s). Unfortunately, the magnetic stirrer introduced so much noise, that the time constant couldn't be determined from this measurement. In another experiment, a filter was applied to decrease noise, but, as an RC filter, it added a time constant of

its own to the measurement, and thus it could not be evaluated.

Despite this discrepancy, with deconvolution, a sharp step function could be obtained from the potential-time measurement, which was very similar to the step function caused by the sudden change in activity of the hydrogen ions. This means, that whatever the cause of the difference between the calculated and estimated resistance is, it distorts the measurement in a very similar way to the RC distortion. Based on the stirring experiments, this is most likely a surface process. Perhaps the antimony-oxide on the surface of the antimony microelectrode is porous, and it hinders diffusion. This behaviour wasn't studied any further in this thesis. Since the recorded step response includes every parameter affecting the delay, the fitted function already accounts for this behaviour. The deconvolution function is certainly not complete and far from perfect. However, all deconvolution in this thesis was performed in a stepwise manner; by only using one $x - y$ pair from Eq. 3.3. X coordinate was most often 0.5 s, the time that elapses between two consecutive measurements. That part of the deconvolution function seems to describe the system very well.

4.3.1.3 Linescans with the antimony microelectrode

Going further, deconvolution of the simplest SECM experiment, the deconvolution of linescans was attempted. The potentiometric cell included the same measuring and reference electrodes as in the previous sections. A model system was built to perform the linescan on. In the system, a hemispherical pH gradient was created. The measured time constant ($\tau = 3.76$ s), implies a significant amount of imaging distortion if the equilibration period is only $t_e = 0.5$ s. As mentioned in the previous section, during 0.5 s, only about 12% of the total change occurs, and the measured difference between the recorded signal at two consecutive data acquisition points is significantly less than the difference between the equilibrium potentials. Since a single linescan can be completed very quickly, for reference a linescan was performed with $t_e = 5$ s. With this equilibration interval, the recorded potential at each point can be regarded equilibrium potential, and the linescan can be used as reference for the deconvoluted linescans performed with shorter t_e . Fig. 4.13A shows the raw linescans 100 μm above the graphite anode. Indeed, with $t_e = 0.5$ s, a significant amount of distortion can be observed. When t_e was increased to 1 s, the distortion decreased. After deconvolution however, all of the linescans became similar to the equilibrium linescans, regarding both their peak value, and shape (Fig. 4.13B).

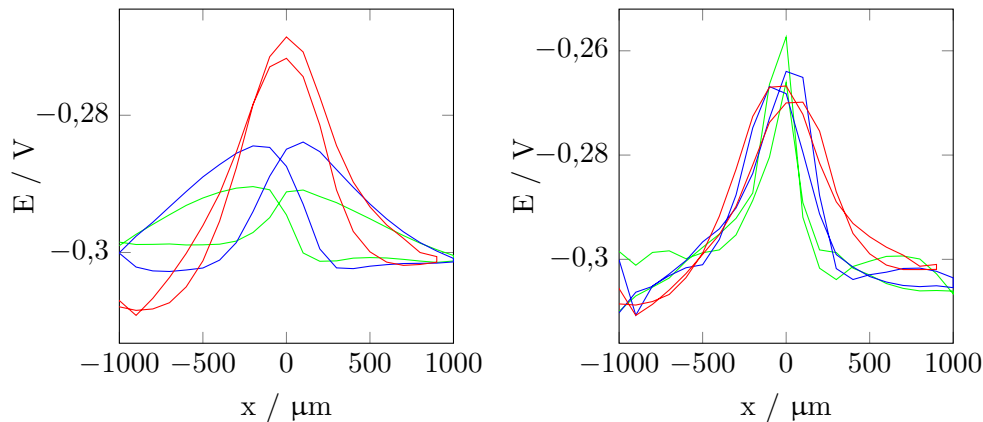


Figure 4.13: (A) Raw, and, (B) deconvoluted SECM linescans above the center of the target, at $h = 100$ mm height, using three different equilibration periods: 0.5 s, (green), 1 s, (blue), and 5 s, (red).

4.3.1.4 2D scans with the antimony microelectrode

Next, four 2D SECM scans were performed identically (Fig. 4.14A-D), with the meander scanning algorithm. The potentiometric cell and the studied system was the same as in the previous section. Again, line blur distortion in the raw images is visible along the alternating scanlines used by the meander scanning algorithm. By deconvoluting the images, the expected potential maps can be obtained (Fig. 4.14E-H).

Not only the circular shape of the target in the images is restored, but the peak value above the center of the target as well. Maximum value in the raw scans was around -300 mV, whereas in the deconvoluted image, it was about -260 mV, with a significant difference between the two.

4.3.1.5 2D scans with the tungsten microelectrodes

Additionally, 2D SECM scans were also performed with two different tungsten microelectrodes: one prepared from commercial tungsten microwire, and another from the filament of a 100 W Tungsram incandescent lighbulb. RC were determined with the same method, and were 4.62 s and 4.40 s, respectively. The studied target in this case was the zinc-copper galvanic pair. The scans were performed 100 μm above the copper target, while it was galvanically coupled to the zinc wire. Line blur distortion is also visible here in the raw images. After deconvolution the expected potential maps can be obtained (Fig. 4.15C-D). Electrode potential above the center of the target increased by about 70 mV in both cases, and the circular symmetry of the copper sample was restored in the image. Considering the sensitivity of the tungset/tungsten-oxide electrode, the difference between the pH of the solution ad-

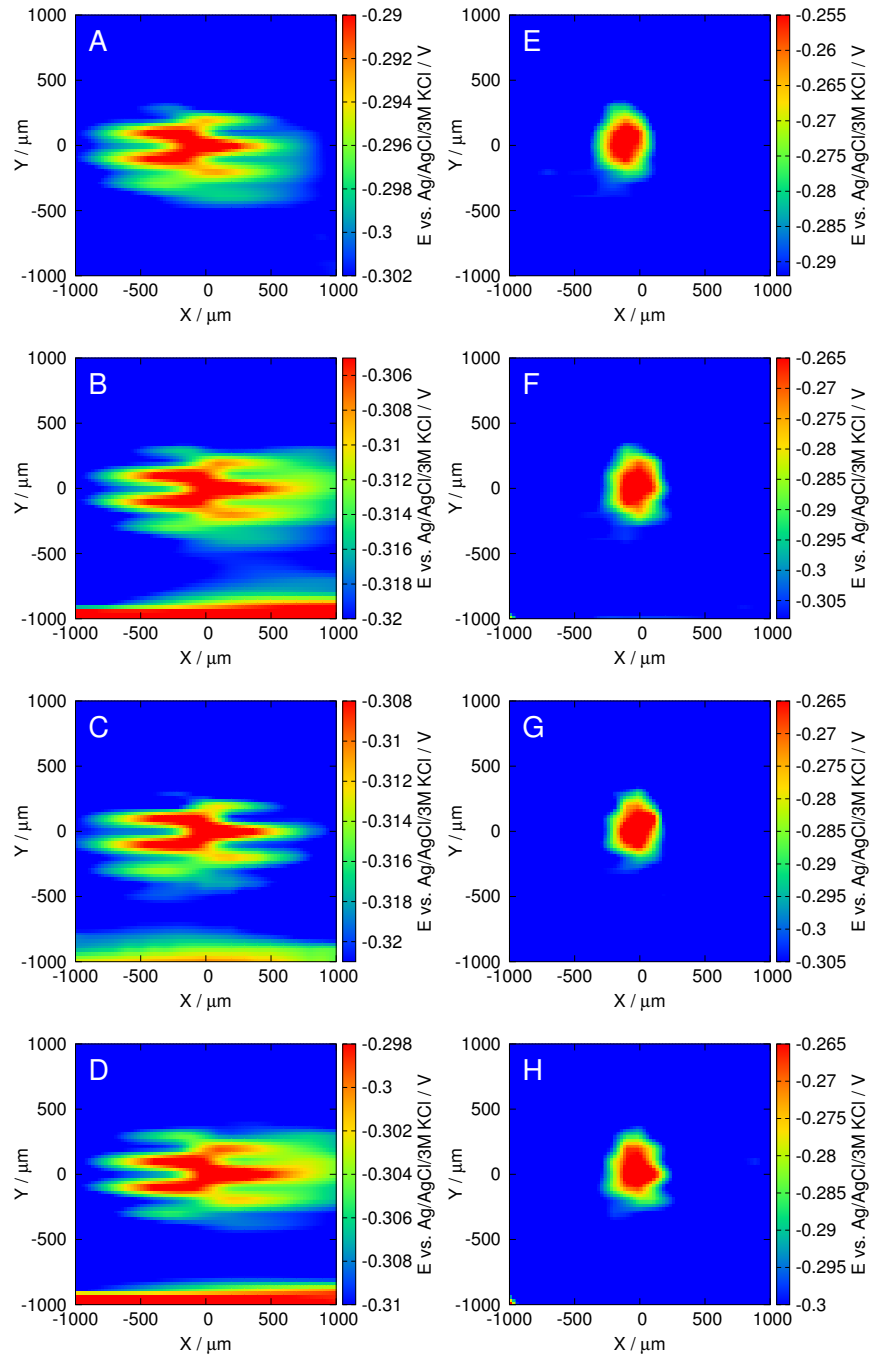


Figure 4.14: Parallel SECM images before (A-D) and after (E-H) deconvolution. Scans conducted with the antimony microelectrode. Note the different potential scales. Deconvolution restores not only the shape of the concentration profile, but the magnitude of the peak as well. The raster scan pattern was used with the meander algorithm starting in the bottom left corner of the image.

jacent to the center of the target and the bulk pH would have been underestimated by about 1.5 pH units.

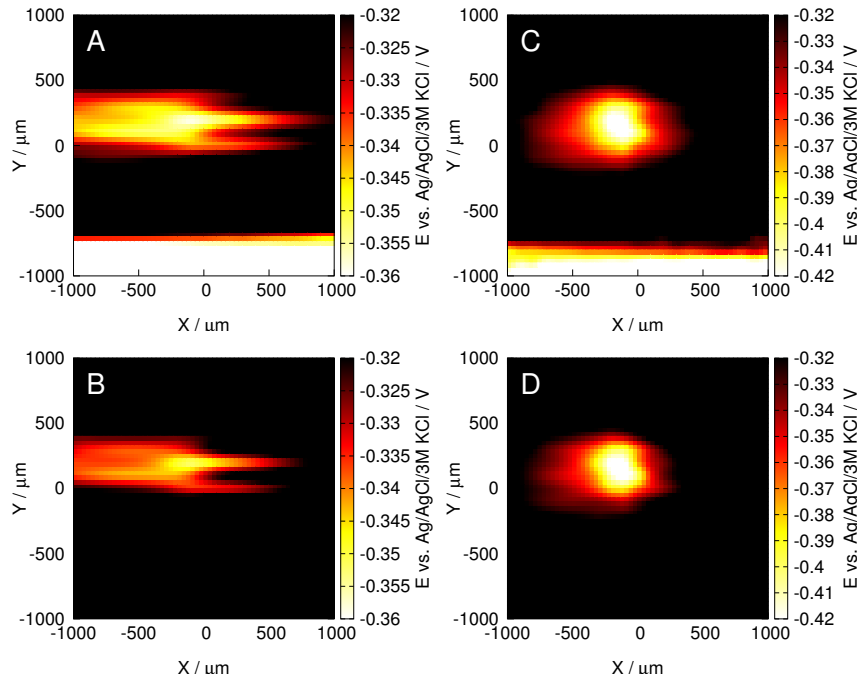


Figure 4.15: SECM image before (A-B) and after (C-D) deconvolution with microelectrodes prepared from commercial $d = 30 \mu\text{m}$ tungsten microwire (A) and tungsten filaments with the same diameter, taken from a 100 W Tungsram incandescent lightbulb (B). The raster scan pattern was used with the meander algorithm starting in the bottom left corner of the image.

4.3.2 Experiments with ion-selective micropipettes

Deconvolution was also applied to SECM scans performed with magnesium and potassium ion-selective micropipettes. In these cases however, RC was determined with another method. R and C were measured individually.

4.3.2.1 Linescans with a magnesium ion-selective micropipette

Measuring R and C . First, the Mg^{2+} ISME and the amplifier were characterized. Using the voltage divider method, electrode resistance of the micropipette was measured to be $197.31 \text{ M}\Omega$. Time constant of the cell with a $50 \text{ M}\Omega$ load inserted was 0.5577 s , therefore amplifier input capacitance (together with the capacitance of a 25 cm long coaxial cable between the electrodes and the amplifier) was 11.15 nF ($0.5577 \text{ s} / 50 \text{ M}\Omega$). Time constant of the potentiometric cell with the Mg^{2+} ion selective electrode could be obtained by multiplying R and C : $\tau = R \times C = 2.2 \text{ s}$.

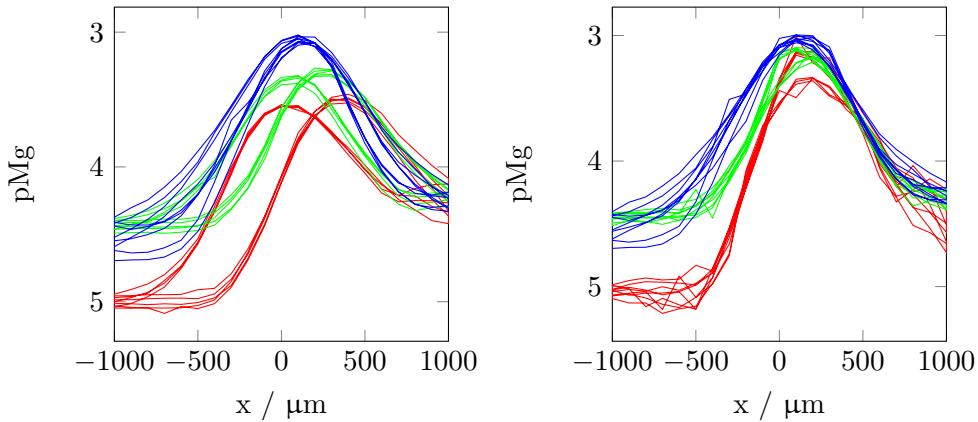


Figure 4.16: (A) Raw scan lines recorded $h = 100 \mu\text{m}$ over the center of the pipette orifice, which served as a Mg^{2+} ion diffusion source. (B) Scan lines obtained after deconvolution. t_e equilibration intervals were 4.9 s (blue), 1.9 s (green), and 0.4 s (red). Probe movement speed was 1000 $\mu\text{m}/\text{s}$, and probe movement interval was 0.1 s. 8 scan lines were recorded in each case, 4 forward, 4 reverse scans.

Sensitivity towards the primary ion was very close to nernstian, with 29.7 mV / decade.

Linescans. Next, line scans above the center of the target were performed using three different equilibration interval lengths. As expected, the shorter the time available for the cell for equilibration was, the more distorted the resulting scan became (Fig. 4.16A). Directional line blur distortion is visible along the raw scan lines recorded with shorter equilibration intervals (1.9 s, and 0.4 s). By setting t_e to 4.9 s, distortion became less visible. Based on the determined RC time constant, in 4.9 seconds, 89.22% of the total change occurs ($1 - e^{-4.9s/2.2s} = 0.8922$), and therefore the recorded signal is almost in equilibrium, and can be regarded as a reference for comparison with the concentration profiles obtained using smaller t_e parameters. With 1.9 s, and 0.4 s, only 57.87%, and 16.62% of the total change occurs respectively, causing a significant amount of distortion.

Using Eq. 3.4 and the measured RC , the scan lines could be deconvoluted, and the E_∞ values could be obtained (Fig. 4.16B). After deconvolution, almost no change can be observed in the scan line recorded with $t_e = 4.9 \text{ s}$, which indicates that the recorded values in that scan were already in equilibrium. By deconvoluting the other scan lines with smaller t_e parameters, they became very similar to the equilibrium scan lines ($t_e = 4.9 \text{ s}$). This indicates that the deconvolution restored the equilibrium scan line. With $t_e = 0.4 \text{ s}$, a similar, low distortion image can be obtained as with $t_e = 4.9 \text{ s}$, but in a fraction of the time that is required for the latter.

4.3.2.2 2D scans with the magnesium ion-selective micropipette

Going further, 2D raster scans were performed with the meander (Fig. 4.17A-D) and the fast comb (Fig. 4.18A-D) algorithms. Similarly as before, line blur distortion in the raw images is visible along the scanlines of the 2D raster. The shorter the equilibration period was, the more visible the distortion became. After deconvoluting the raw images, not only the circular shape of the target in the image is restored, but - based on the results of the linescan deconvolution - the maximum $p\text{Mg}^{2+}$ value above the center of the target as well, using the meander (Fig. 4.17E-H), and the fast comb scanning algorithms (Fig. 4.18E-H). For instance, maximum $p\text{Mg}^{2+}$ in the $t_e=0.4$ s meander raw scan is about 4.2, whereas in the deconvoluted image, it is about 3.6, with a significant difference between the two. This is important where accurate quantitative information is required about the target, such as in fitting simulated scans to measured ones to calculate mass transport rate [105].

4.3.2.3 2D scans with the potassium ion-selective micropipette

2D scans employing the most widely used potassium ion-selective micropipette were also carried out. The same cell was used as before, only the magnesium ion-selective micropipette was replaced with a potassium ion-selective micropipette. Resistance of the potassium ion-selective micropipette was measured with the same voltage divider method, and not surprisingly, the result was very similar; $R = 213.42 \text{ M}\Omega$. The time constant was $\tau = 2.38$ s. The target was the same micropipette source, except the filling gel was replaced with a 0.2 M KCl containing 4% agar-agar gel. The characteristic RC distortion is also visible in these images (Fig. 4.19A-B). After deconvolution, once again, the images resemble the radial geometry of the target.

4.3.3 Application: investigation of the corrosion of carbon steel

Corroding carbon steel was imaged as part of a collaboration with colleagues from the *University of Ibn Zohr*, Agadir. They were curious about the pH changes above the corroding sample while it was polarized anodically with different current densities applied. Since corrosion is highly localized, a single linescan above the center wasn't enough, as it might not have covered all of the local anodes, ie. the surface cannot be regarded homogeneous without proof. For this reason, the whole surface was scanned. The total surface area was about 0.2 cm^2 , and a relatively large image had to be taken for the whole sample to be included. A $6000 \mu\text{m} \times 6000 \mu\text{m}$ image was scanned with a step size of $100 \mu\text{m}$ in both directions. To make the scan as short as possible despite the large number of data acquisition

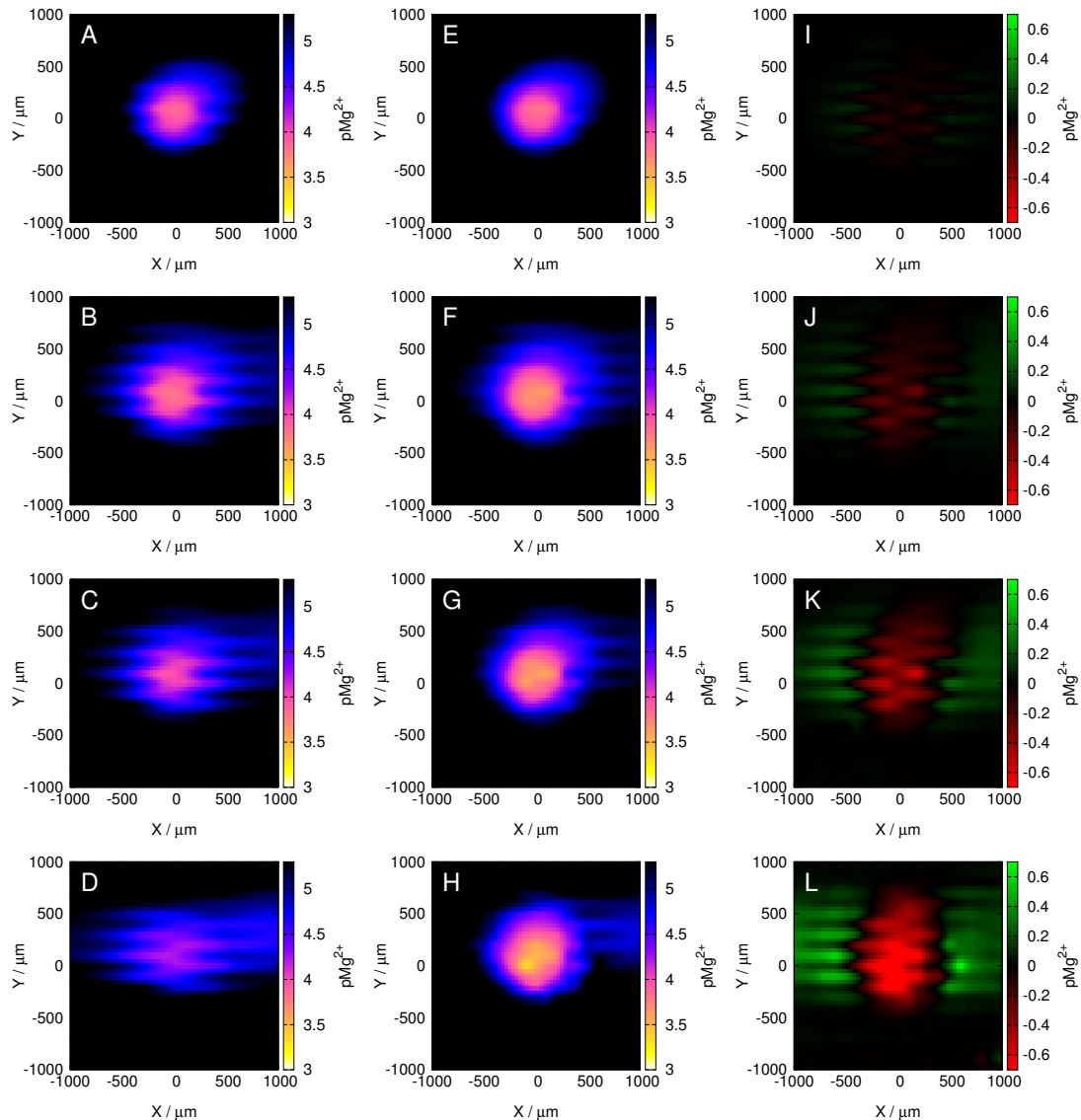


Figure 4.17: SECM images scanned with the meander algorithm, before (A-D) and after (E-H) deconvolution. Equilibration intervals from top to bottom row: $t_e = 4.9 \text{ s}, 1.9 \text{ s}, 0.9 \text{ s}, 0.4 \text{ s}$. Scanning started in the bottom left corner, scanlines were recorded horizontally from left to right. The difference between the raw and the deconvoluted images (I-L). Green: after deconvolution, pMg^{2+} increased, red: pMg^{2+} decreased in the images. That is, based on the original images, $[\text{Mg}^{2+}]$ concentration would have been over-, and underestimated at those specific coordinates, respectively. The raster scan pattern was used with the meander algorithm starting in the bottom left corner of the image.

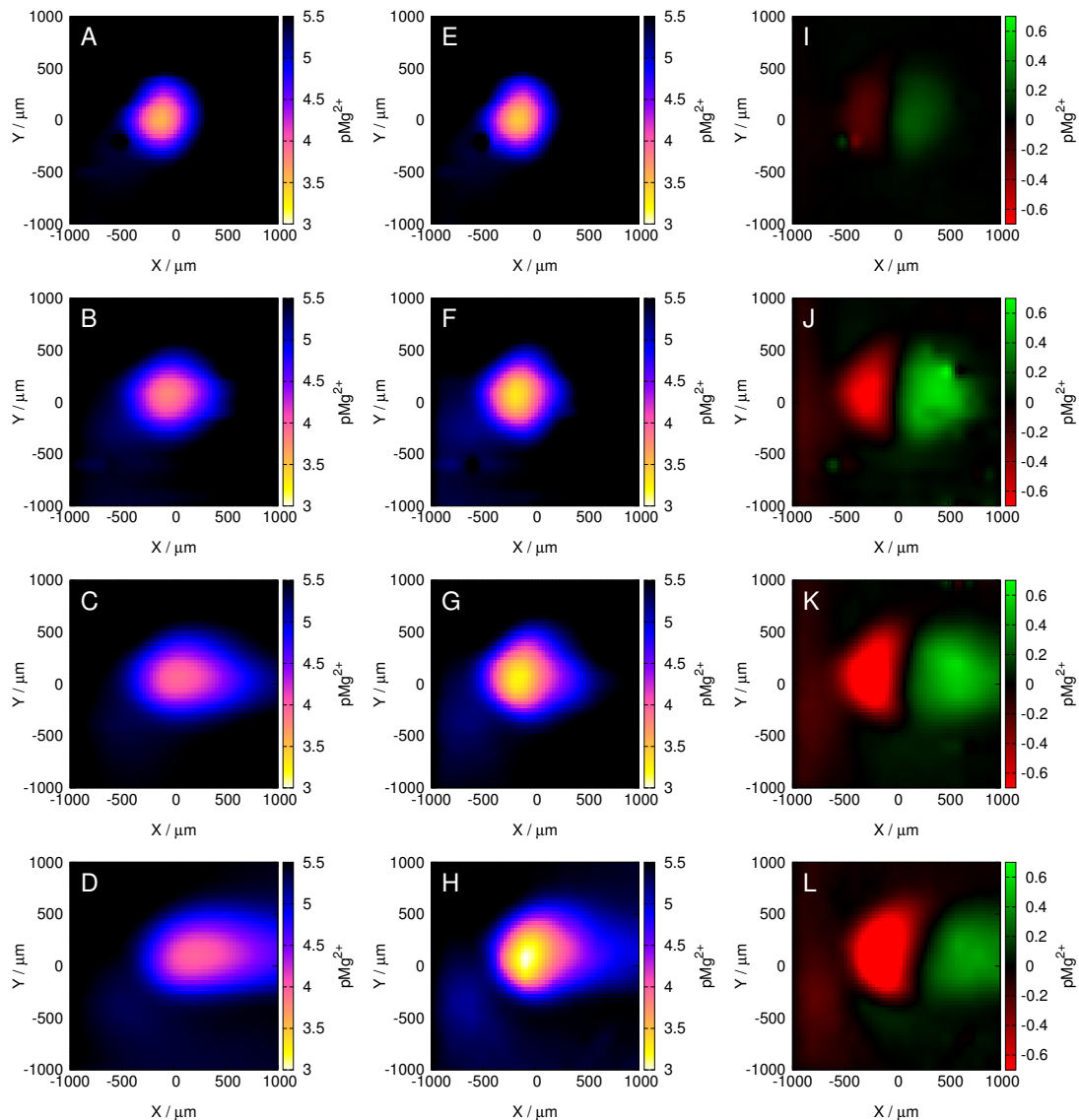


Figure 4.18: SECM images scanned with the fast comb algorithm, before (A-D) and after (E-H) deconvolution. Equilibration intervals from top to bottom row: $t_e = 4.9$ s, 1.9 s, 0.9 s, 0.4 s. Scanning started in the bottom left corner, scanlines were recorded horizontally from left to right. The difference between the raw and the deconvoluted images (I-L). Green: after deconvolution, pMg^{2+} increased, red: pMg^{2+} decreased in the images. That is, based on the original images, $[\text{Mg}^{2+}]$ concentration would have been over-, and underestimated at those specific coordinates, respectively. The raster scan pattern was used with the fast comb algorithm starting in the bottom left corner of the image.

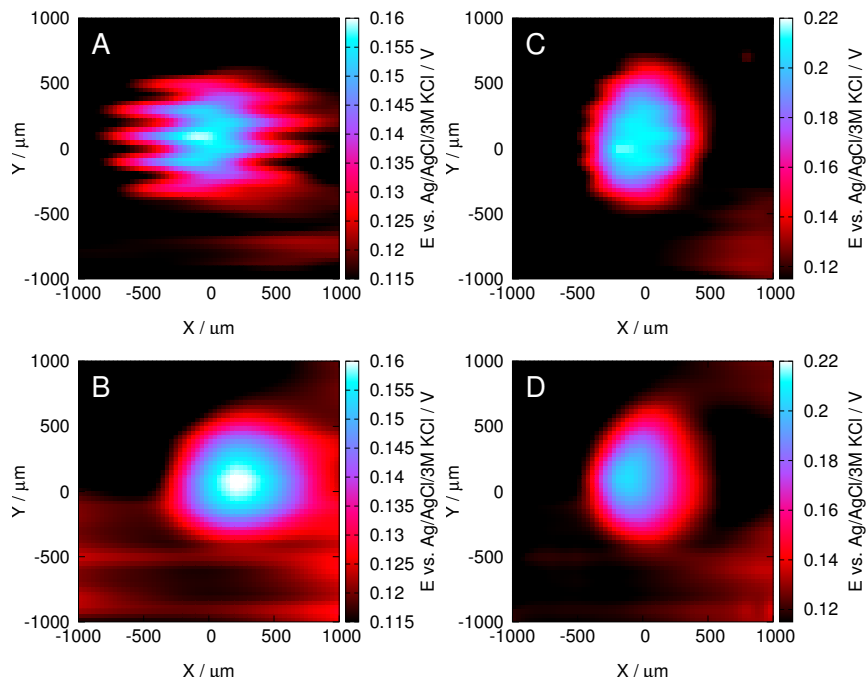


Figure 4.19: SECM image before (A-B) and after (C-D) deconvolution. Scans conducted with solid contact K^+ ion-selective micropipette. The raster scan pattern was used with the meander algorithm starting in the bottom left corner of the image.

points, a scanrate of $1000 \mu\text{m}/\text{s}$ was used. As expected, the image was distorted, and without any processing evaluation proved to be difficult. After deconvolution, conclusions about that particular experiment could be drawn. The irregular shape of the target (Fig. 4.20C) is recognisable after (Fig. 4.20B), but not before (Fig. 4.20A) the deconvolution. The difference between the original and the processed image is quite large. Potential difference between points of the bulk of the electrolyte and the electrolyte above the target was 140 mV and 200 mV before, and after the deconvolution, which is quite similar to values obtained in the previous experiments. Without any processing, pH would have been misestimated by about 1 pH unit. A different conclusion can be drawn based on the raw, and the deconvoluted image.

4.3.4 Possibility of „blind deconvolution”

„*Blind deconvolution*” is the technique of deconvoluting measured data without the complete knowledge of the transfer function that describes the convolution [110]. In the section titled „Minimal working example” I deconvoluted a simple step response with several different assumed RC time-constants, including the measured one. Even with just visual inspection of the deconvoluted data, one would choose the dataset that was obtained when the correct, measured RC was used in the de-

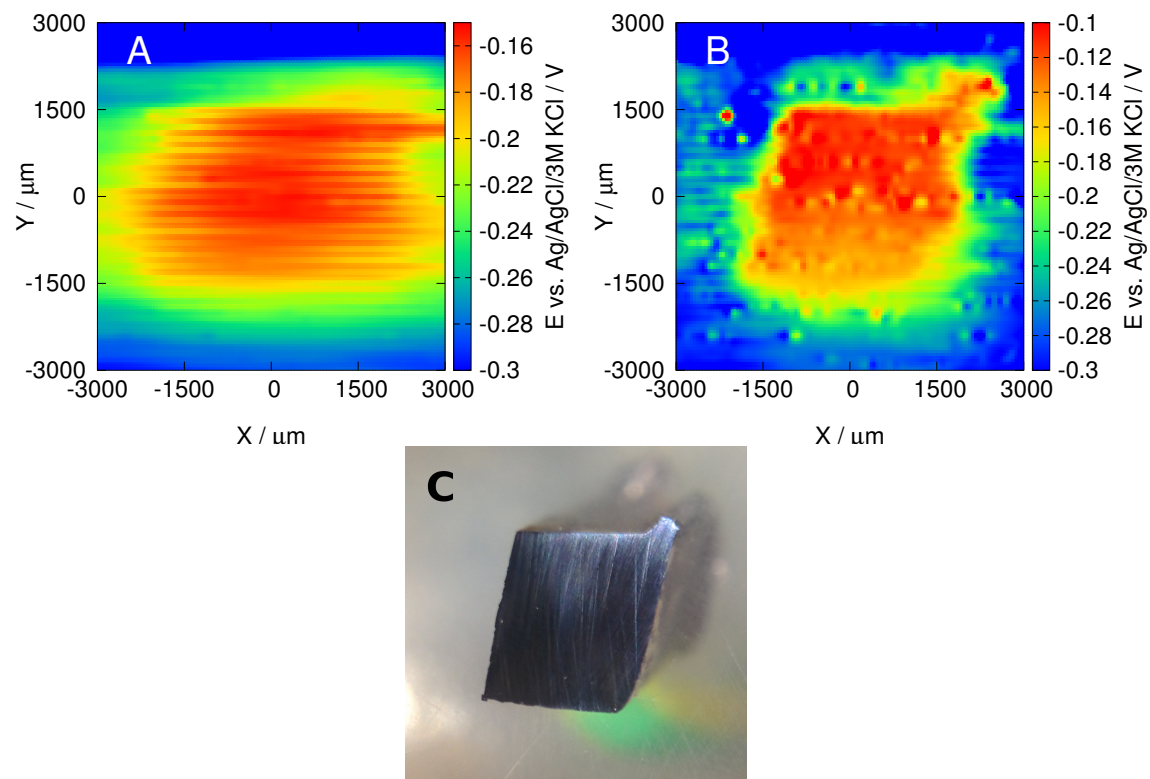


Figure 4.20: Raw (A), and deconvoluted (B) SECM image and microphoto (C) of a corroding carbon-steel sample polarized anodically with a current density of 10 mA/cm^2 . Measuring electrode was an antimony pH microelectrode. Potential was measured against an Ag/AgCl/3M KCl. Recorded $h = 100 \mu\text{m}$ above the surface with probe movement speed of $1000 \mu\text{m/s}$, equilibration interval 0.4 s .

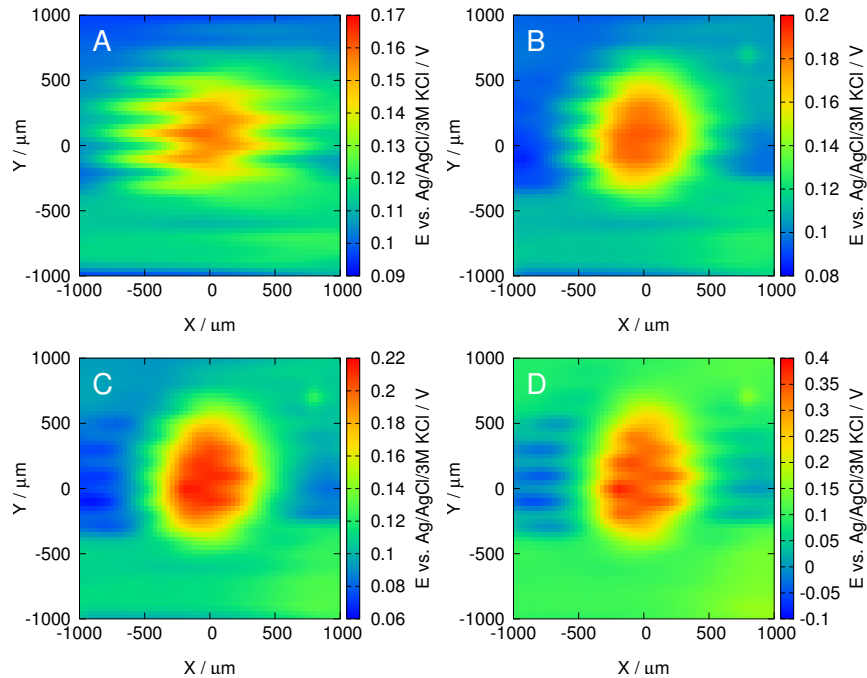


Figure 4.21: Deconvolutions of the image in Fig. 4.19A with different assumed RC time-constants, including the measured one. The measurement was done with a potassium ion-selective electrode. The measured time constant was $\tau = 2.38$ s. Figure shows the raw image (A), and deconvolutions with assumed time-constants $\tau = 1.39$ s (B), $\tau = \mathbf{2.38}$ s (C), $\tau = 7.80$ s (D).

convolution. Based on this observation, blind deconvolution of 2D images might be possible. To explore this possibility, similarly to the step response deconvolution, I deconvoluted a pH image using the deconvolution function with several different time-constant substitutions, including the measured one.

A primitive version of applying this method involves the deconvolution with different RC values (Fig. 4.21), and choosing the images with the least amount of visible RC distortion. „Evaluating” distortion is relatively easy if the scanning algorithm is known. RC distortion is especially visible in images scanned with the meander algorithm. With this algorithm, subsequent scan lines in the images are shifted by twice the amount with respect to each other than with respect to a fixed point in the image, since the scan directions of subsequent lines are opposite.

Observing the images, (B) is still distorted, the individual lines are „shifted” in the same direction as in the raw image. In (D) however, they are shifted in the opposite direction, because the assumed time-constant is too high, and there is excess deconvolution in the image. (C) seems to be the best, but the lines are a bit shifted to the opposite direction. The best result based on visual inspection would be between (B) and (C), although much closer to (C). (C) is the image which was

obtained as a result of deconvolution with the measured time-constant.

A more advanced method would be a statistical approach, where one would try to detect any correlation between the scanning algorithm – taking into account the scan direction – and the image, and choose the deconvoluted image with the least correlation.

4.4 The effect of electric field on potentiometric SECM images

During galvanic corrosion, ions are being released from the anode. The measured potential of an ion selective microelectrode is thought to depend only on the activity of the primary ion. However, an electric field is also formed as a result of the potential difference between the surfaces of the galvanic pair, which has a direct influence on the potential of the measuring microelectrode, as it is depicted in Fig. 4.22. The measured potential is the sum of these two contributions:

$$\Delta E = E_M - E_R + (\phi_M - \phi_R) \quad (4.5)$$

where ΔE is the measured potential difference, E_R is the potential of the reference electrode, and ϕ_M and ϕ_R are the local potentials in the electric field at the measuring and reference electrodes, respectively. E_M is the potential of the measuring ion-selective electrode for instance Mg^{2+} :

$$E_M = S \times \lg[Mg^{2+}] + E_M^o \quad (4.6)$$

where S is the slope of the calibration curve of the potentiometric cell with respect to the primary ion, and E_M^o is the standard potential.

The potential difference caused by the electric field can be substantially large, even exceeding that of the potential difference associated with the activity of the primary ion. For instance, in [111] local alkalinization above the cathode of the studied galvanic pair could be observed as far as 2 mm from the surface, while oxygen reduction current had already reached the bulk level at only 900 μm from the target. This contradiction was explained by a contribution from the electric field of the galvanic pair. Similar discrepancy was found in [112–114], where the Mg^{2+} detected by the ion selective microelectrode exceeded the upper limit of detection. On the other hand, in [115] electrode potential of the employed magnesium ion selective electrode reached below potentials corresponding to the lower limit of detection of the electrode. These contradictory results can be explained by a contribution of the electric field that is formed during these experiments.

In this section, I present experimental evidence of this phenomenon, and investigate the extent to which it influences the final potentiometric SECM image. For this purpose, I use the Fe-AZ63 galvanic pair studied in the previous sections. The SECM probe was a solid contact magnesium ion selective electrode.

First, a series of consecutive Z-approach curves were recorded above the corroding AZ63 sample (as shown in fig. 4.23A). The first 6 measurements were taken while

the AZ63 sample was not electrically connected to the iron sample (red lines, a-b). As expected, Mg^{2+} activity slowly increased with time as a result of spontaneous corrosion. The overall change was about 10 mV in 5 minutes. Next, the two metals were connected at the rear of the mould. As a result of establishing the galvanic connection, there was an immediate rise of about 40 mV in the measured potential of the microelectrode (transition from b to c, depicted by ΔE_1 in fig. 4.23A). Since the galvanic coupling was established while the scanning tip was located 1000 μm from the AZ63 sample, the reported change cannot possibly be attributed solely to an abrupt increase in Mg^{2+} activity. Indeed, such a 40 mV change would correspond to an increase of ca. 1.5 orders of magnitude in Mg^{2+} activity occurring in less than one second. Immediately after, six additional Z-approach curves were recorded during the galvanic coupling. The resulting accelerated dissolution of Mg^{2+} can be distinguished from the blue curves (c-d) in fig. 4.23A. Intense gas evolution could be observed on the surface of the AZ63 sample, which explains the noticeably more noisy curves recorded in this case. During this period of galvanic coupling, the potential sensed at the ISME, when situated at $h = 1000 \mu m$, increased in app. 40 mV. This rise (ΔE_2) can be totally attributed to the increase in activity of the dissolving metal, i.e.: $\Delta E = 29.5 mV \times \Delta \lg[Mg^{2+}]$. Finally, when the galvanic connection was stopped, 2 additional Z-approach curves were measured (green curves in fig. 4.23A). A sudden jump in potential (ΔE_3 , transition from d to e) can be observed, of the same magnitude as before, though in the opposite direction, as a result of electric field vanishing. The shape of the latest Z-approach curves is very similar to the initial approaching curves recorded before galvanic connection was established, though they are shifted by about 40 mV in the positive direction. This is the result of the enhanced corrosion during the second phase of the experiment; Mg^{2+} activity changed by about the same factor along the length of the scan-line. The shape of the Z-approach curves recorded during the galvanic coupling is notoriously different from those recorded during the spontaneous corrosion of the metal. This is because the contribution of the electric field, just like the contribution from Mg^{2+} , is not uniform at different distances on the scanned line. The strength of the electric field is inversely proportional to the square of the distance. The shape of the function $1/z^2$ is recognizable from these plots.

An attempt was made to distinguish the effect of the electric field from that of the Nernstian response of the ISME by subtracting curve *b* from the subsequent curve *c*. *B* is the result of the Nernstian response, while *c* features the contribution from the electric field as well. Since *c* was recorded just after *b* in a short period of time, it can be assumed that there was no significant increase of Mg^{2+} concentration during these two scans, therefore *c* is just *b*+ $\Delta\phi$. The result of the subtraction is

curve *f* in fig. 4.23A, which can be regarded as the effect of the electric field formed between the galvanic pair.

In another series of experiments, the ISME was maintained at a constant height from the metal surface, and its potential was recorded as a function of time, while the galvanic connection was established between the two metals (fig. 4.23B). Thus, the tip was first positioned 100 μm above the center of the AZ63 wire (red curve in fig. 4.23B), and for about 300 s the spontaneous corrosion of the alloy sample was recorded. Then, the galvanic connection was established, and a sharp increase in potential of about 70 mV could be observed. This change would correspond to a two orders of magnitude increase of Mg^{2+} activity in a very short period of time. When the galvanic connection was removed, a potential change of the same magnitude, though opposite direction could be observed. In order to discard the possibility that this rise could be still explained by an abrupt release of Mg^{2+} from the surface, the experiment was repeated while the tip was positioned 1000 μm above the target (blue curve in fig. 4.23B). A very similar sequence of potential changes could be observed, despite the big separation between the probe and the corroding sample. The only plausible explanation is that the abrupt change in the recorded potential is due to the electric field developed between the two metals.

Finally, in order to demonstrate the influence of the electric field on SECM imaging, measurements were made after 30 minutes of galvanic coupling by using a constant 100 μm tip-sample distance. Then the galvanic connection was ceased, and immediately another 2D scan was recorded above the Mg disk. The sequence of the two images can be seen in fig. 4.24. Apparently, in the case of galvanic coupling, a 0.1 M Mg^{2+} activity is monitored even in the bulk of the solution, whereas above the center of the disk the activity reaches the implausible 10^4 M value by using the calibration curve for calculation. In fig. 4.24B the measured values are in the linear range of the ISME, and the overall potential change is several orders of magnitude smaller than in fig. 4.24A.

The effect of the electric field in certain potentiometric SECM experiments has been demonstrated experimentally, as suspected by certain researchers in corrosion science for some time. A strong electric field is formed around galvanic coupling of dissimilar metals, that causes significant over- or underestimations of the real primary ion activity. The reason for this feature is that the electric field has a direct influence on the measured potential at the ISME.

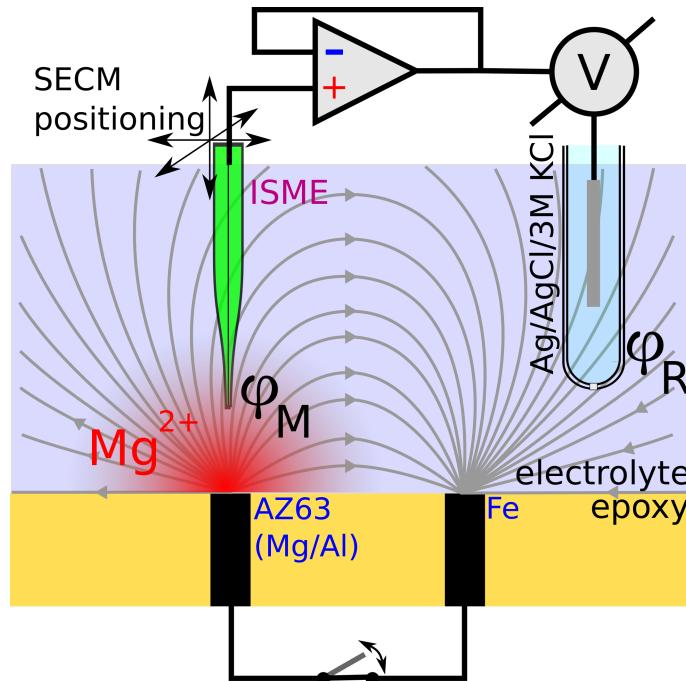


Figure 4.22: An electric field is formed between the surfaces of the galvanic couple. The potential difference between the measuring (ϕ_M) and reference (ϕ_R) electrodes is added to the Nernstian potential associated with the activity of the primary ion.

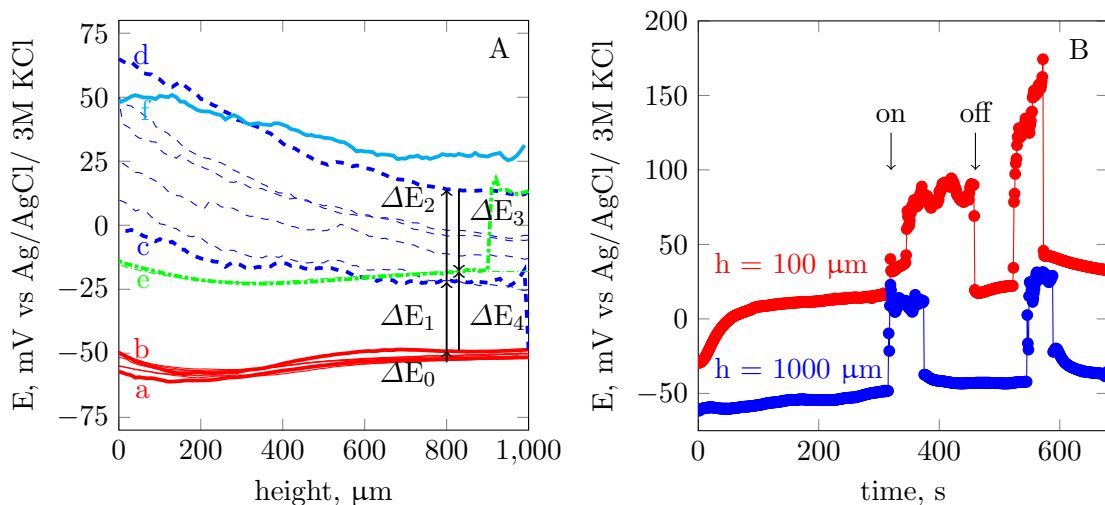


Figure 4.23: (A) Sequence of consecutive Z-approach curves recorded above the center of the AZ63 wire with a Mg^{2+} ISME. Step size: 10 μm . 500 ms settling time was allowed for the potentiometric cell at each points before measurements. Lines in chronological order: solid red = spontaneous corrosion, dashed blue = galvanic corrosion, dash dotted green = spontaneous corrosion. (B) Stationary recordings above the center of the AZ63 target with the ISME placed at: red = 100 μm , blue = 1000 μm distance from the metal. On/off denote the moment when galvanic coupling was either established or ceased. Temporal resolution was 1 Hz.

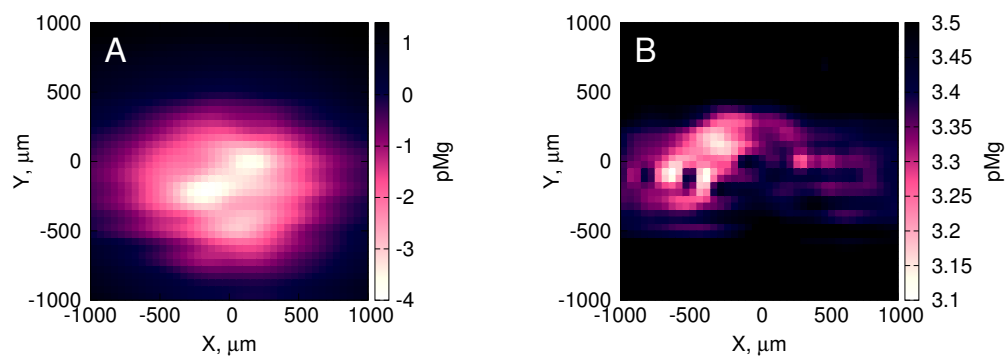


Figure 4.24: 2D Mg^{2+} ion distributions above the AZ63 wire while: (A) galvanically connected to Fe and (B) immediately after ceasing electrical connection between the two metallic materials. Tip-sample distance: 100 μm .

Chapter 5

Conclusions

The present work has been devoted to improve potentiometric Scanning Electrochemical Microscopy. Scanning is relatively slow due to the long response time of the potentiometric measuring cell. Shortened scanning time is useful when the studied system is changing. When scanned too fast however, distortion is added to the image. I've successfully sped up the technique without compromising image quality. In another effort, I've managed to separate the effect of electric field from the Nernstian potential response of the ion selective microelectrode.

The main results are summarized in the thesis points:

1. I've successfully shortened response time of the potentiometric cell by using low resistance, solid-contact microelectrodes. I've compared them to conventional, liquid contact microelectrodes by basic characterization and model system study to prove the improved performance.
2. Taking advantage of the new solid-contact electrodes, I've studied the galvanic corrosion of magnesium and the AZ63 magnesium alloy by mapping the concentration of dissolving ions. I used the new solid contact ion selective microelectrodes as SECM probes. This allowed faster scan rates.
3. I've estimated the corrosion current based on the SECM measurements, and compared the result with that obtained with another, established method; the indirect measurement of corrosion current. After applying Faraday's Law of Electrolysis, the two results could be compared. They were very similar, suggesting the applicability of SECM in obtaining quantitative results.
4. I've designed new scanning patterns and algorithms, optimized to radially symmetric targets. I've proven that with these new patterns and algorithms, image distortion is lower compared to the conventional ones, by numerical simulations and experimental SECM scans.

5. I've shown that by using deconvolution, RC distortion can be significantly lowered in the potentiometric SECM images. To prove the validity of the technique, I've compared deconvoluted images to equilibrium images scanned at a rate which allowed to record equilibrium potentials.
6. I've used deconvolution to restore potentiometric SECM images about a corroding carbon steel sample. Evaluation of this data was possible, because scanning time *and* distortion was reduced at the same time.
7. I've shown the applicability of blind deconvolution. This method can be used on measurements where the convolution function cannot be determined.
8. I've proven that the electric field present in many studied systems – galvanically corroding ones in particular – affects the measured potential. The electric field has a direct influence on the measured potential, which is then a sum of this contribution and the Nernstian response associated with ion activity. This effect can cause serious errors in interpretations in the measurements. In this case, the error was almost four orders of magnitude. By taking this effect into account, a more accurate conclusion can be drawn.

List of Figures

2.1	The pioneers of electrophysiology, the first to use microelectrodes	8
2.2	The Gold Standard of pH measurement, the Harned cell (at the Danish National Metrology Institute)	11
2.3	The first true ion-selective microelectrodes, created by Hinke	13
2.4	(A) Valinomycin, (B) bis-N,N-dicyclohexyl-malonamide, and (C) non-actin, ionophores for potassium, magnesium, and ammonium ions, respectively	16
2.5	The model of the potentiometric measurement	18
2.6	The series <i>RC</i> circuit	20
2.7	Charging and discharging the series <i>RC</i> circuit	22
2.8	A typical potentiometric SECM setup	26
2.9	The distortive effect of potentiometric SECM imaging when scanning at relatively high speed. The effective speed of the probe is too high, and therefore the time available for the potentiometric cell is too short to reach equilibrium before recording the potential difference at a given point. The image is blurred along the scan line in the direction of the scan	28
3.1	Antimony/silver pH-sensitive combined macroelectrodes	31
3.2	Antimony and tungsten microelectrodes for local pH measurements . .	32
3.3	Sketches and micrographs of the micropipette electrodes fabricated for the selective detection of Mg^{2+} ions	34
3.4	Cyclic voltammetric electropolymerization of PEDOT onto the carbon fiber to create the solid internal contact for the ion-selective microelectrodes	35
3.5	The potentiometric cell with the TL082 voltage follower	36
3.6	The home-made, Arduino based DAQ	38
3.7	Voltage divider circuit to measure electrode resistance	39
3.8	The hanging drop method	40

3.9	Illustration of the parameters used for the determination of response time.	41
3.10	Sketch and photo of the model system with the embedded glass pipette Mg ²⁺ or K ⁺ ion diffusion source, and the SECM scan setup.	43
3.11	Sketch of the moulded model targets and the SECM scan setup used for these targets.	44
3.12	The water heater sacrificial anode made of the AZ63 magnesium-aluminium-zinc alloy. The sample was prepared from such an anode by a precision lathe.	45
3.13	Scanning algorithms.	47
3.14	Microphotos for the backlash compensation measurements for the home-made SECM.	50
3.15	The Scanning Electrochemical Microscopes I used in my work.	54
3.16	Circuit for measuring corrosion current between a galvanic couple.	55
4.1	Calibration plots for the Mg ²⁺ ISME.	59
4.2	Dynamic response curves obtained for response time measurements to changes in MgCl ₂ concentrations.	60
4.3	Response of ISME to shorting resistors for the voltage divider method.	60
4.4	SECM images displaying the Mg ²⁺ ion concentrations 100 µm above the tip of a centered pipette source.	61
4.5	SECM scans above the magnesium sample with the solid- and liquid contact magnesium ion-selective micropipettes.	63
4.6	Retracting and lateral SECM linescans above the AZ63 sample initiated at different instances in time.	64
4.7	1/i plots used for the determination of corrosion current between the AZ63 magnesium-aluminium-zinc alloy and various iron samples of different diameters.	65
4.8	Simulated SECM scans 100 µm above the disc source and deviation from the original images.	68
4.9	Experimental SECM scans 100 µm above the disc source.	69
4.10	Transient response of the antimony microelectrode to analyte activity step.	72
4.12	The effect of stirring on the antimony microelectrode.	75
4.13	Raw and deconvoluted SECM linescans with the antimony microelectrode.	77
4.14	Parallel SECM images before and after the deconvolution. Scans conducted with the antimony microelectrode.	78

4.15 SECM image before and after deconvolution. Scans conducted with the tungsten microelectrodes.	79
4.16 Raw, and deconvoluted linescans conducted with the Mg ²⁺ ISME	80
4.17 SECM images scanned with the meander algorithm using the Mg ²⁺ ISME, before and after deconvolution.	82
4.18 SECM images scanned with the fast comb algorithm using the Mg ²⁺ ISME, before and after deconvolution.	83
4.19 SECM image before and after deconvolution. Scans conducted with solid contact K ⁺ ion-selective micropipette.	84
4.20 Raw, and deconvoluted SECM image and microphoto of a corroding carbon-steel sample polarized anodically.	85
4.21 Deconvolutions of the image in Fig. 4.19A with different assumed <i>RC</i> time-constants, including the measured one.	86
4.22 An electric field is formed between the surfaces of the galvanic couple. The potential difference between the measuring (ϕ_M) and reference (ϕ_R) electrodes is added to the Nernstian potential associated with the activity of the primary ion.	91
4.23 (A) Sequence of consecutive Z-approach curves recorded above the center of the AZ63 wire with a Mg ²⁺ ISME. Step size: 10 μm . 500 ms settling time was allowed for the potentiometric cell at each points before measurements. Lines in chronological order: solid red = spontaneous corrosion, dashed blue = galvanic corrosion, dash dotted green = spontaneous corrosion. (B) Stationary recordings above the center of the AZ63 target with the ISME placed at: red = 100 μm , blue = 1000 μm distance from the metal. On/off denote the moment when galvanic coupling was either established or ceased. Temporal resolution was 1 Hz.	91
4.24 2D Mg ²⁺ ion distributions above the AZ63 wire while: (A) galvanically connected to Fe and (B) immediately after ceasing electrical connection between the two metallic materials. Tip-sample distance: 100 μm	92

List of Tables

3.1	Composition of the mixture employed to produce the cocktail for the Mg ²⁺ and K ⁺ ion-selective microelectrodes.	33
4.1	Resistance measurements for the two kinds of Mg ²⁺ ion-selective micropipette electrodes.	62
4.2	Comparison of the scanning algorithms.	69
4.3	Comparison of the deconvoluted time-potential recordings with different assumed time-constants, including the measured value (highlighted in bold).	72

List of Abbreviations

SECM	Scanning Electrochemical Microscopy
SPM	Scanning Probe Microscopy
AFM	Atomic Force Microscopy
STM	Scanning Tunnelling Microscopy
d_i	internal diameter
d_o	external diameter
THF	tetrahydrofuran
PVC	poly(vinyl chloride)
PTCB	potassium tetrakis(4-chlorophenyl)-borate
oNPOE	2-nitrophenyl octyl ether
ISME	ion-selective microelectrode
EDOT	ethylenedioxothiophene
PEDOT	poly(3,4-ethylenedioxothiophene)
$\text{BMIM}^+\text{PF}_6^-$	1-butyl-3-methylimidazolium hexafluorophosphate
r	scanrate ($\mu\text{m}/\text{s}$)
s	step size (μm)
t_e	equilibration interval length (s)
$E_{cell}(\infty)$	equilibrium cell potential difference (mV, V)
$E_{cell}(0)$	cell potential difference prior to change (mV, V)
$E_{cell}(t)$	cell potential difference at time t (s)
τ	time constant (s)
RC	time constant of a series RC circuit (s)
D	diffusion coefficient
R_{ISME}	resistance of the ion-selective microelectrode (Ω)
E_{OCP}	open circuit potential of the measuring electrode (mV, V)
Ω	ion flux
c_s	surface concentration ($\text{mol} \times \text{dm}^{-3}$)
z, h	height of scan (μm)
R_o	output resistance (Ω)
R_i	input resistance (Ω)

C_i	input capacitance (F)
R_0	electrode resistance (Ω)
C_s	cable capacitance (F)
$vcc+$	positive voltage rail of the power supply
$vcc-$	negative voltage rail of the power supply
RPM	revolution per minute
emf	electromotive force
LIX (membrane)	liquid ion exchanger (membrane)
CWE	coated wire electrode

References

- [1] I. J. GRAHAM, “Membrane potentials and excitation of impaled single muscle fibers,” *Journal of Cellular and Comparative Physiology*, vol. 28, pp. 99–118, 1946.
- [2] D. Webb and J. Young, “Electrolyte content and action potential of the giant nerve fibres of loligo,” *The Journal of physiology*, vol. 98, no. 3, p. 299, 1940.
- [3] H. J. Curtis and K. S. Cole, “Membrane action potentials from the squid giant axon,” *Journal of Cellular and Comparative Physiology*, vol. 15, no. 2, pp. 147–157, 1940.
- [4] H. J. Curtis and K. S. Cole, “Membrane resting and action potentials from the squid giant axon,” *Journal of cellular and comparative physiology*, vol. 19, no. 2, pp. 135–144, 1942.
- [5] G. Ling and R. Gerard, “The normal membrane potential of frog sartorius fibers,” *Journal of cellular and comparative physiology*, vol. 34, no. 3, pp. 383–396, 1949.
- [6] A. Hodgkin and W. Nastuk, “Membrane potentials in single fibres of the frog’s sartorius muscle.,” *The Journal of physiology*, vol. 108, no. 3, pp. Proc–42, 1949.
- [7] W. Nastuk and A. L. Hodgkin, “The electrical activity of single muscle fibers,” *Journal of Cellular and comparative Physiology*, vol. 35, no. 1, pp. 39–73, 1950.
- [8] G. Ling and R. Gerard, “External potassium and the membrane potential of single muscle fibres,” 1950.
- [9] E. Neher and B. Sakmann, “Single-channel currents recorded from membrane of denervated frog muscle fibres,” *Nature*, pp. 799–802, 1976.
- [10] E. Neher, B. Sakmann, and J. H. Steinbach, “The extracellular patch clamp: a method for resolving currents through individual open channels in biological membranes,” *Pflügers Archiv*, vol. 375, no. 2, pp. 219–228, 1978.

- [11] M. Cremer, *Über die Ursache der elektromotorischen Eigenschaften der Gewebe, zugleich ein Beitrag zur Lehre von den polyphasischen Elektrolytketten.* R. Oldenbourg, 1906.
- [12] M. Cremer, *Über die direkte ableitung der aktionsströme des menschlichen herzens vom oesophagus und über das elektrokardogramm des fötus.* Lehmann, 1906.
- [13] S. P. L. Sørensen, “Über die messung und die bedeutung der wasserstoffionenkonzentration bei enzymatischen prozessen,” 1909.
- [14] H. S. Harned and A. Gancy, “The activity coefficient of hydrochloric acid in potassium chloride solutions,” *The Journal of Physical Chemistry*, vol. 62, no. 5, pp. 627–629, 1958.
- [15] R. A. Durst, *Standardization of pH measurements*, vol. 260. US Dept. of Commerce, National Bureau of Standards: for sale by the Supt. of Docs., US Govt. Print. Off., 1975.
- [16] A. Covington, M. Milton, C. Brett, F. Baucke, G. S. Wilson, R. Naumann, K. Pratt, P. Spitzer, S. Rondinini, R. Buck, *et al.*, “Measurement of ph. definition, standards, and procedures,” 2002.
- [17] R. Bates and E. Guggenheim, “Report on the standardization of ph and related terminology,” *Pure and Applied Chemistry*, vol. 1, no. 1, pp. 163–168, 1960.
- [18] F. Haber and Z. Klemensiewicz, “Über elektrische phasengrenzkräfte,” *Z. phys. Chem.*, vol. 67, pp. 385–431, 1909.
- [19] F. Haber and Z. Klemensiewicz, “Concerning electrical phase boundary forces.,” *Zeitschrift Fur Physikalische Chemie-Stochiometrie Und Verwandtschaftslehre*, vol. 67, no. 4, pp. 385–431, 1909.
- [20] P. Caldwell, “An investigation of the intracellular ph of crab muscle fibres by means of micro-glass and micro-tungsten electrodes,” *The Journal of physiology*, vol. 126, no. 1, p. 169, 1954.
- [21] G. Eisenman, D. O. Rudin, and J. U. Casby, “Glass electrode for measuring sodium ion,” *Science*, vol. 126, no. 3278, pp. 831–834, 1957.
- [22] B. v. Lengyel and E. Blum, “The behaviour of the glass electrode in connection with its chemical composition,” *Transactions of the Faraday Society*, vol. 30, pp. 461–471, 1934.

- [23] S. M. Friedman, J. D. Jamieson, J. Hinke, and C. L. Friedman, “Use of glass electrode for measuring sodium in biological systems.,” *Experimental Biology and Medicine*, vol. 99, no. 3, pp. 727–730, 1958.
- [24] S. M. Friedman, J. D. Jamieson, J. Hinke, and C. L. Friedman, “Drug-induced changes in blood pressure and in blood sodium as measured by glass electrode,” *American Journal of Physiology-Legacy Content*, vol. 196, no. 5, pp. 1049–1052, 1959.
- [25] J. Hinke, “Glass micro-electrodes for measuring intracellular activities of sodium and potassium,” 1959.
- [26] R. Beutner, “New galvanic phenomena,” *American Journal of Physiology-Legacy Content*, vol. 31, no. 6, pp. 343–351, 1913.
- [27] G. Eisenman, J. Sandblom, and J. Walker, “Membrane structure and ion permeation,” *Science*, vol. 155, no. 3765, pp. 965–974, 1967.
- [28] J. Sandblom, G. Eisenmann, and J. Walker, “Electrical phenomena associated with the transport of ions and ion pairs in liquid ion-exchange membranes. i. zero current properties,” *Journal of Physical Chemistry*, vol. 71(12), pp. 3862–3870, 1967.
- [29] J. Sandblom, G. Eisenmann, and J. Walker, “Electrical phenomena associated with the transport of ions and ion pairs in liquid ion-exchange membranes. i. nonzero current properties,” *Journal of Physical Chemistry*, vol. 71(12), pp. 3871–3878, 1967.
- [30] J. L. WALKER JR, “Ion specific liquid ion exchanger microelectrodes,” *Analytical chemistry*, vol. 43, no. 3, pp. 89A–93A, 1971.
- [31] B. Nicolsky, “Theory of the glass electrode. i,” *Acta Physiochem USSR*, vol. 7, p. 597, 1937.
- [32] Z. Stefanac and W. Simon, “Highly selective cation electrode systems based on in-vitro behavior of macrotetrodolides in membranes,” *Chimica*, vol. 20, pp. 436–440, 1966.
- [33] Z. Štefanac and W. Simon, “Ion specific electrochemical behavior of macrotetrodolides in membranes,” *Microchemical Journal*, vol. 12, no. 1, pp. 125–132, 1967.
- [34] D. Ammann, P. Chao, and W. Simon, “Valinomycin-based k+ selective microelectrodes with low electrical membrane resistance,” *Neuroscience letters*, vol. 74, no. 2, pp. 221–226, 1987.

- [35] M. Oehme and W. Simon, “Microelectrode for potassium ions based on a neutral carrier and comparison of its characteristics with a cation exchanger sensor,” *Analytica chimica acta*, vol. 86, pp. 21–25, 1976.
- [36] P. Wuhrmann, H. Ineichen, U. Riesen-Willi, and M. Lezzi, “Change in nuclear potassium electrochemical activity and puffing of potassium-sensitive salivary chromosome regions during chironomus development,” *Proceedings of the National Academy of Sciences*, vol. 76, no. 2, pp. 806–808, 1979.
- [37] K. Kimura, T. Maeda, H. Tamura, and T. Shono, “Potassium-selective pvc membrane electrodes based on bis-and poly (crown ether) s,” *Journal of Electroanalytical Chemistry and Interfacial Electrochemistry*, vol. 95, no. 1, pp. 91–101, 1979.
- [38] J. W. Severinghaus and A. F. Bradley, “Electrodes for blood po₂ and pco₂ determination,” *Journal of applied physiology*, vol. 13, no. 3, pp. 515–520, 1958.
- [39] L. C. Clark, R. Wolf, D. Granger, and Z. Taylor, “Continuous recording of blood oxygen tensions by polarography,” *Journal of applied physiology*, vol. 6, no. 3, pp. 189–193, 1953.
- [40] W.-J. Cai and C. E. Reimers, “The development of ph and pco₂ microelectrodes for studying the carbonate chemistry of pore waters near the sediment-water interface,” *Limnology and Oceanography*, vol. 38, no. 8, pp. 1762–1773, 1993.
- [41] D. De Beer, A. Glud, E. Epping, and M. Kuhl, “A fast-responding co₂ microelectrode for profiling sediments, microbial mats, and biofilms,” *Limnology and Oceanography*, vol. 42, no. 7, pp. 1590–1600, 1997.
- [42] P. Zhao and W.-J. Cai, “An improved potentiometric p co₂ microelectrode,” *Analytical Chemistry*, vol. 69, no. 24, pp. 5052–5058, 1997.
- [43] S. Hanstein, D. de Beer, and H. H. Felle, “Miniaturised carbon dioxide sensor designed for measurements within plant leaves,” *Sensors and Actuators B: Chemical*, vol. 81, no. 1, pp. 107–114, 2001.
- [44] H. Beyenal, C. C. Davis, and Z. Lewandowski, “An improved severinghaus-type carbon dioxide microelectrode for use in biofilms,” *Sensors and Actuators B: Chemical*, vol. 97, no. 2, pp. 202–210, 2004.
- [45] A. Kiss, L. Kiss, B. Kovács, and G. Nagy, “Air gap microcell for scanning electrochemical microscopic imaging of carbon dioxide output. model calculation

and gas phase secm measurements for estimation of carbon dioxide producing activity of microbial sources,” *Electroanalysis*, vol. 23, no. 10, pp. 2320–2326, 2011.

- [46] B. Nikolskii and E. Materova, “Solid contact in membrane ion-selective electrodes,” *Ion-Sel Electrode Rev*, vol. 7, no. 3, 1985.
- [47] R. Cattrall and H. Freiser, “Coated wire ion-selective electrodes,” *Analytical Chemistry*, vol. 43, no. 13, pp. 1905–1906, 1971.
- [48] J. Bobacka, A. Ivaska, and A. Lewenstam, “Potentiometric ion sensors based on conducting polymers,” *Electroanalysis*, vol. 15, no. 5-6, pp. 366–374, 2003.
- [49] J. Bobacka, T. Lindfors, A. Lewenstam, and A. Ivaska, “All-solid-state ion sensors using conducting polymers as ion-to-electron transducers,” *American laboratory*, vol. 36, no. 3, pp. 13–20, 2004.
- [50] J. Bobacka, “Conducting polymer-based solid-state ion-selective electrodes,” *Electroanalysis*, vol. 18, no. 1, pp. 7–18, 2006.
- [51] A. Michalska, “Optimizing the analytical performance and construction of ion-selective electrodes with conducting polymer-based ion-to-electron transducers,” *Analytical and bioanalytical chemistry*, vol. 384, no. 2, pp. 391–406, 2006.
- [52] X. X. Sun, X. Zhang, and H. Y. Aboul-Enein, “Construction and characterization of potentiometric sensor for the determination of oxytetracycline hydrochloride,” *Il Farmaco*, vol. 59, no. 4, pp. 307–314, 2004.
- [53] J. Bobacka, M. McCarrick, A. Lewenstam, and A. Ivaska, “All solid-state poly (vinyl chloride) membrane ion-selective electrodes with poly (3-octylthiophene) solid internal contact,” *Analyst*, vol. 119, no. 9, pp. 1985–1991, 1994.
- [54] R. Paciorek, P. Bieganowski, and M. Maj-Żurawska, “Miniature planar chloride electrodes,” *Sensors and Actuators B: Chemical*, vol. 108, no. 1, pp. 840–844, 2005.
- [55] G. Gyetvai, S. Sundblom, L. Nagy, A. Ivaska, and G. Nagy, “Solid contact micropipette ion selective electrode for potentiometric secm,” *Electroanalysis*, vol. 19, no. 10, pp. 1116–1122, 2007.
- [56] Á. Varga, L. Nagy, J. Izquierdo, I. Bitter, R. M. Souto, and G. Nagy, “Development of solid contact micropipette zn-ion selective electrode for corrosion studies,” *Analytical Letters*, vol. 44, no. 18, pp. 2876–2886, 2011.

- [57] J. Izquierdo, L. Nagy, Á. Varga, I. Bitter, G. Nagy, and R. M. Souto, “Scanning electrochemical microscopy for the investigation of corrosion processes: measurement of Zn^{2+} spatial distribution with ion selective microelectrodes,” *Electrochimica Acta*, vol. 59, pp. 398–403, 2012.
- [58] S. P. Kounaves, M. G. Buehler, M. H. Hecht, and S. West, “Determination of geochemistry on mars using an array of electrochemical sensors,” in *ACS Symposium Series*, vol. 811, pp. 306–319, Washington, DC; American Chemical Society; 1999, 2002.
- [59] M. Södergård, B. Csóka, G. Nagy, and A. Ivaska, “Lowering the detection limit of solvent polymeric ion-selective membrane electrodes. an experimental study with calcium-selective micropipette electrodes,” *Analytical letters*, vol. 36, no. 14, pp. 2909–2923, 2003.
- [60] A. Malon, T. Vigassy, E. Bakker, and E. Pretsch, “Potentiometry at trace levels in confined samples: ion-selective electrodes with subfemtomole detection limits,” *Journal of the American Chemical Society*, vol. 128, no. 25, pp. 8154–8155, 2006.
- [61] J. Sutter, A. Radu, S. Peper, E. Bakker, and E. Pretsch, “Solid-contact polymeric membrane electrodes with detection limits in the subnanomolar range,” *Analytica chimica acta*, vol. 523, no. 1, pp. 53–59, 2004.
- [62] A. Uhl and W. Kestranek, “The electrometric titration of acids and bases with the antimony indicator electrodes,” *Monatsh. Chem.*, vol. 44, pp. 29–34, 1923.
- [63] J. Halliwell, M. Whitaker, and D. OGDEN, “Using microelectrodes,” *Microelectrode techniques. The Company of Biologists Limited, Cambridge, ppl*, vol. 12, 1987.
- [64] W. Hill and P. Horowitz, “The art of electronics,” 2015.
- [65] E. Lindner, K. Tóth, and E. Pungor, “Definition and determination of response time of ion selective electrodes,” *Pure and Applied Chemistry*, vol. 58, no. 3, pp. 469–479, 1986.
- [66] G. Binnig, H. Rohrer, C. Gerber, and E. Weibel, “Surface studies by scanning tunneling microscopy,” *Physical review letters*, vol. 49, no. 1, p. 57, 1982.
- [67] G. Binnig, H. Rohrer, C. Gerber, and E. Weibel, “Physica (utrecht) 107b+ c (1981) 1335; 109 and 110b (1982) 2075,” *Appl. Phys. Lett.*, vol. 40, p. 178, 1982.

- [68] G. Binnig, H. Rohrer, C. Gerber, and E. Weibel, “Tunneling through a controllable vacuum gap,” *Applied Physics Letters*, vol. 40, no. 2, pp. 178–180, 1982.
- [69] E. Abbe, “Beiträge zur theorie des mikroskops und der mikroskopischen wahrnehmung,” *Archiv für mikroskopische Anatomie*, vol. 9, no. 1, pp. 413–418, 1873.
- [70] G. Binnig, C. F. Quate, and C. Gerber, “Atomic force microscope,” *Physical review letters*, vol. 56, no. 9, p. 930, 1986.
- [71] G. Binnig, “Atomic force microscope and method for imaging surfaces with atomic resolution,” Feb. 9 1988. US Patent 4,724,318.
- [72] U. Hartmann, “Magnetic force microscopy: Some remarks from the micromagnetic point of view,” *Journal of applied physics*, vol. 64, no. 3, pp. 1561–1564, 1988.
- [73] P. Hansma, B. Drake, O. Marti, S. Gould, and C. Prater, “The scanning ion-conductance microscope,” *Science*, vol. 243, no. 4891, pp. 641–643, 1989.
- [74] W. Kaiser and L. Bell, “Direct investigation of subsurface interface electronic structure by ballistic-electron-emission microscopy,” in *Electronic Structure of Metal-Semiconductor Contacts*, pp. 252–255, Springer, 1990.
- [75] J. Weaver and D. W. Abraham, “High resolution atomic force microscopy potentiometry,” *Journal of Vacuum Science & Technology B*, vol. 9, no. 3, pp. 1559–1561, 1991.
- [76] M. Nonnenmacher, M. o’Boyle, and H. Wickramasinghe, “Kelvin probe force microscopy,” *Applied physics letters*, vol. 58, no. 25, pp. 2921–2923, 1991.
- [77] A. M. Chang, H. D. Hallen, L. Harriott, H. Hess, H. Kao, J. Kwo, R. Miller, R. Wolfe, J. Van der Ziel, and T. Chang, “Scanning hall probe microscopy,” *Applied Physics Letters*, vol. 61, no. 16, pp. 1974–1976, 1992.
- [78] J. Xu, K. Läuger, K. Dransfeld, and I. Wilson, “Thermal sensors for investigation of heat transfer in scanning probe microscopy,” *Review of scientific instruments*, vol. 65, no. 7, pp. 2262–2266, 1994.
- [79] T. Trenkler, P. De Wolf, W. Vandervorst, and L. Hellemans, “Nanopotentiometry: Local potential measurements in complementary metal–oxide–semiconductor transistors using atomic force microscopy,” *Journal of Vacuum Science & Technology B*, vol. 16, no. 1, pp. 367–372, 1998.

- [80] A. J. Bard, F. R. F. Fan, J. Kwak, and O. Lev, “Scanning electrochemical microscopy. introduction and principles,” *Analytical Chemistry*, vol. 61, no. 2, pp. 132–138, 1989.
- [81] A. J. Bard, F.-R. F. Fan, and M. V. Mirkin, “Scanning electrochemical microscopy,” *Electroanalytical chemistry*, vol. 18, pp. 243–373, 1994.
- [82] A. J. Bard and M. V. Mirkin, *Scanning electrochemical microscopy*. CRC Press, 2012.
- [83] R. C. Engstrom, M. Weber, D. J. Wunder, R. Burgess, and S. Winquist, “Measurements within the diffusion layer using a microelectrode probe,” *Analytical Chemistry*, vol. 58, no. 4, pp. 844–848, 1986.
- [84] R. C. Engstrom and C. M. Pharr, “Scanning electrochemical microscopy,” *Analytical Chemistry*, vol. 61, no. 19, pp. 1099A–1104A, 1989.
- [85] B. R. Horrocks, M. V. Mirkin, D. T. Pierce, A. J. Bard, G. Nagy, and K. Toth, “Scanning electrochemical microscopy. 19. ion-selective potentiometric microscopy,” *Analytical Chemistry*, vol. 65, no. 9, pp. 1213–1224, 1993.
- [86] A. Bastos, M. Taryba, O. Karavai, M. Zheludkevich, S. Lamaka, and M. Ferreira, “Micropotentiometric mapping of local distributions of Zn^{2+} relevant to corrosion studies,” *Electrochemistry Communications*, vol. 12, no. 3, pp. 394–397, 2010.
- [87] S. Lamaka, O. Karavai, A. Bastos, M. Zheludkevich, and M. Ferreira, “Monitoring local spatial distribution of Mg^{2+} , pH and ionic currents,” *Electrochemistry Communications*, vol. 10, no. 2, pp. 259–262, 2008.
- [88] S. V. Lamaka, M. G. Taryba, M. L. Zheludkevich, and M. G. Ferreira, “Novel solid-contact ion-selective microelectrodes for localized potentiometric measurements,” *Electroanalysis*, vol. 21, no. 22, pp. 2447–2453, 2009.
- [89] O. Karavai, A. Bastos, M. Zheludkevich, M. Taryba, S. Lamaka, and M. Ferreira, “Localized electrochemical study of corrosion inhibition in microdefects on coated az31 magnesium alloy,” *Electrochimica Acta*, vol. 55, no. 19, pp. 5401–5406, 2010.
- [90] M. Schrader, S. Hell, and H. Van der Voort, “Potential of confocal microscopes to resolve in the 50–100 nm range,” *Applied physics letters*, vol. 69, no. 24, pp. 3644–3646, 1996.

- [91] P. Eaton and P. West, *Atomic force microscopy*. Oxford University Press, 2010.
- [92] W. Lo and J. Spence, “Investigation of stm image artifacts by in-situ reflection electron microscopy,” *Ultramicroscopy*, vol. 48, no. 4, pp. 433–444, 1993.
- [93] Q. Chen and S. A. Kumar, “Deconvolution of atomic force microscopy data for cellular and molecular imaging,” 2006.
- [94] D. Osiro, R. Bernardes Filho, O. B. G. Assis, L. A. d. C. Jorge, and L. A. Colnago, “Measuring bacterial cells size with afm,” *Brazilian Journal of Microbiology*, vol. 43, no. 1, pp. 341–347, 2012.
- [95] A. Bukharaev, N. Berdunov, D. Ovchinnikov, and K. Salikhov, “Three-dimensional probe and surface reconstruction for atomic force microscopy using a deconvolution algorithm,” *in practice*, vol. 5, p. 21, 1998.
- [96] R. Robinson, “Increasing the scanning speed of scanning tunnelling microscopes,” *Journal of Microscopy*, vol. 152, no. 2, pp. 387–397, 1988.
- [97] C. Lee, D. O. Wipf, A. J. Bard, K. Bartels, and A. C. Bovik, “Scanning electrochemical microscopy. 11. improvement of image resolution by digital processing techniques,” *Analytical Chemistry*, vol. 63, no. 21, pp. 2442–2447, 1991.
- [98] K. Tóth, E. Lindner, M. Horváth, J. Jeney, E. Pungor, I. Bitter, B. Ágai, and L. Töke, “Analytical performances of lipophilic diamides based alkaline earth ion-selective electrodes,” *Electroanalysis*, vol. 5, no. 9-10, pp. 781–790, 1993.
- [99] J. Rowberg, “I2cdev library collection,” <https://github.com/jrowberg/i2cdevlib/blob/master/Ar> 2013.
- [100] A. D. McNaught and A. D. McNaught, *Compendium of chemical terminology*, vol. 1669. Blackwell Science Oxford, 1997.
- [101] D. Britz, “Digital simulation in electrochemistry, 1988.”
- [102] M. Calugareanu, G. Nagy, A. M. Josceanu, and L. Nagy, “Ion selective electrodes for microalgal biotechnology,” *REVISTA DE CHIMIE*, vol. 64, no. 2, pp. 205–209, 2013.
- [103] E. R. Scott, H. S. White, and J. B. Phipps, “Iontophoretic transport through porous membranes using scanning electrochemical microscopy: application to in vitro studies of ion fluxes through skin,” *Analytical chemistry*, vol. 65, no. 11, pp. 1537–1545, 1993.

- [104] D. R. Lide, “Crc handbook of physics and chemistry,” 2001.
- [105] R. E. Gyurcsányi, G. Jágerszki, G. Kiss, and K. Tóth, “Chemical imaging of biological systems with the scanning electrochemical microscope,” *Bioelectrochemistry*, vol. 63, no. 1, pp. 207–215, 2004.
- [106] E. Lindner, K. Toth, and E. Pungor, “Definition of the response time of ion-selective electrodes and potentiometric cells,” *Analytical Chemistry*, vol. 56, no. 4, pp. 808–810, 1984.
- [107] E. Lindner, K. Toth, and E. Pungor, “Response time studies for precipitate-based ion-selective electrodes in the range of the lower detection limit,” *Analytical Chemistry*, vol. 54, no. 1, pp. 72–76, 1982.
- [108] L. E. J. Havas, J.; Kecske *Hung. Sci. Instrum.*, vol. 57, p. 27, 1981.
- [109] E. Lindner, K. Toth, and E. Pungor, “Response time curves of ion-selective electrodes,” *Analytical Chemistry*, vol. 48, no. 7, pp. 1071–1078, 1976.
- [110] E. Y. Lam and J. W. Goodman, “Iterative statistical approach to blind image deconvolution,” *JOSA A*, vol. 17, no. 7, pp. 1177–1184, 2000.
- [111] J. Izquierdo, L. Nagy, I. Bitter, R. M. Souto, and G. Nagy, “Potentiometric scanning electrochemical microscopy for the local characterization of the electrochemical behaviour of magnesium-based materials,” *Electrochimica Acta*, vol. 87, pp. 283–293, 2013.
- [112] R. M. Souto, A. Kiss, J. Izquierdo, L. Nagy, I. Bitter, and G. Nagy, “Spatially-resolved imaging of concentration distributions on corroding magnesium-based materials exposed to aqueous environments by secm,” *Electrochemistry Communications*, vol. 26, pp. 25–28, 2013.
- [113] R. Souto, J. Izquierdo, J. Santana, A. Kiss, L. Nagy, and G. Nagy, “Progress in scanning electrochemical microscopy by coupling potentiometric and amperometric measurement modes,” *Current Microscopy Contributions to Advances in Science and Technology, Formatec Research Center, Badajoz*, pp. 1407–1415, 2012.
- [114] J. Izquierdo, A. Kiss, J. J. Santana, L. Nagy, I. Bitter, H. S. Isaacs, G. Nagy, and R. M. Souto, “Development of mg²⁺ ion-selective microelectrodes for potentiometric scanning electrochemical microscopy monitoring of galvanic corrosion processes,” *Journal of The Electrochemical Society*, vol. 160, no. 9, pp. C451–C459, 2013.

- [115] J. Izquierdo, B. M. Fernández-Pérez, D. Filotás, Z. Őri, A. Kiss, R. T. Martín-Gómez, L. Nagy, G. Nagy, and R. M. Souto, “Imaging of concentration distributions and hydrogen evolution on corroding magnesium exposed to aqueous environments using scanning electrochemical microscopy,” *Electroanalysis*, 2016.

Appendix

5.1 Diffusion and SECM scan simulation

```
program diffusion

implicit none

integer :: x_size, y_size, z_size
integer :: res, height
integer :: time_res

! 0.000703 mm^2/s = 703um^2/s for resolution of 1umx1um and 1s
! = 0.00000703 cm^2/s for resolution of 1umx1um and 1s
! CRC Handbook of chemistry and physics 87th 2006–2007.pdf page 848
! 1/2 Zn2+ -ra vonatkozik.

real :: const=0.017575 !for resolution of 20umx20um and 0.1s
! real :: const=0.02812 !for resolution of 50umx50um and 0.1s

integer :: h,i,j,k,x,y,m,switch,cells
real, dimension(0:101,0:101,0:101) :: a, b
real, dimension(1:100,1:100,1:100) :: flux
integer, dimension(1:100,1:100,1:100) :: mask
real :: pi=3.1415926535897932384626433832795
real maximum

real e0, x_real, y_real
real, dimension(0:100,0:100) :: sim
integer direction, divisions
real alpha, circumference, r_real
integer r, n
direction=-1
```

```

maximum=0.000000000000000
height=50

a=0.
b=0.
mask=1

do i=1, 100
  do j=1, 100
    if ( ((i-50)**2+(j-50)**2) < 20**2 ) then
      !20 itt a source sugara = 400um
      flux(i,j,1)=0.1
    endif
  end do
end do

open(1, file='flux_at_1um.txt')
do i=0, 100
  do j=0, 100
    write(1, *) i*20, j*20, flux(i,j,1)
  end do
end do
close(1)

open(1, file='flux_at_1um_final_res.txt')
do i=0, 100, 5
  do j=0, 100, 5
    write(1, *) i*20, j*20, flux(i,j,1)
  end do
end do
close(1)

do k=1, 100
  do i=1, 100
    mask(i, 1, k)=0
    mask(i, 100, k)=0
  end do
end do

```

```

do k=1, 100
  do j=1, 100
    mask(1, j, k)=0
    mask(100, j, k)=0
  end do
end do
do j=1, 100
  do i=1, 100
    mask(i, j, 100)=0
  end do
end do
end do

b=a
switch=0
! x=i, y=j, z=k, h=time
do h=1, 500 ! M A I N L O O P

  ! All real cells computed. Not cycled: borders, which are all zeros.
  do k=1, 100
    do j=1, 100
      do i=1, 100
        if (mask(i, j, k)==1) then
          cells=6
          if ((k==1) .or. (k==100)) then
            cells=cells-1
          endif
          if ((j==1) .or. (j==100)) then
            cells=cells-1
          endif
          if ((i==1) .or. (i==100)) then
            cells=cells-1
          endif
          b(i, j, k)=a(i, j, k)+const*(a(i, j+1, k)+a(i-1, j, k)+a(i+1, j, k) &
          +a(i, j-1, k)+a(i, j, k-1)+a(i, j, k+1)-cells*a(i, j, k))
        endif
      end do
    end do
  end do

```

```

end do

do j=1, 100
  do i=1, 100
    b(i,j,1)=b(i,j,1)+flux(i,j,1)
  end do
end do

a=b
print *,h

end do

do i=0, 100
  do j=0, 100
    if (a(i,j,height)>maximum) then
      maximum=a(i,j,height)
    endif
  end do
end do
print *,maximum
do i=0, 100
  do j=0, 100
    a(i,j,height)=a(i,j,height)/maximum
  end do
end do

! OUT PUT
open(1,file='real_100um_fullres.txt')
do i=0, 100
  do j=0, 100
    write(1, *) i*20, j*20, a(i,j,height)
  end do
end do
close(1)

open(1,file='real_100um_finalres.txt')
do i=0, 100, 5

```

```

do j=0, 100, 5
  write(1, *) i*20, j*20, a(i,j,height)
end do
end do
close(1)

! SECM scanning simulation
! FAST COMB
sim=0
e0=a(0,0,height)
open(1,file='fast_comb.txt')
do y=0, 100, 5
  do x=0, 100, 5
    sim(x,y) = a(x,y,height) + (e0-a(x,y,height))*0.8
    e0=sim(x,y)
    write(1, *) x*20, y*20, sim(x,y)
  end do
  do x=100, 0, 5
    e0 = a(x,y,height) + (e0-a(x,y,height))*0.9
  end do
end do
close(1)

! MEANDER
sim=0
e0=a(0,0,height)
open(1,file='meander.txt')
do y=0, 100, 5
  direction=direction*(-1)
  if (direction==1) then
    do x=0, 100, 5
      sim(x,y) = a(x,y,height) + (e0-a(x,y,height))*0.8
      e0=sim(x,y)
      write(1, *) x*20, y*20, sim(x,y)
    end do
  else
    do x=100, 0, -5
      sim(x,y) = a(x,y,height) + (e0-a(x,y,height))*0.8
    end do
  end if
end do

```

```

e0=sim(x,y)
write(1, *) x*20, y*20, sim(x,y)
end do
endif
end do
close(1)

! COMB
sim=0
e0=a(0,0,height)
open(1,file='comb.txt')
open(2,file='comb-pattern.txt')
do y=0, 100, 5
  do x=0, 100, 5
    sim(x,y) = a(x,y,height) + (e0-a(x,y,height))*0.8
    e0=sim(x,y)
    ! write(1, *) x*20, y*20, sim(x,y)
    write(2, *) x*20, y*20, sim(x,y)
  end do
  do x=100, 0, -5
    sim(x,y) = (sim(x,y) + a(x,y,height) + (e0-a(x,y,height))*0.8)/2
    e0=a(x,y,height) + (e0-a(x,y,height))*0.8
    write(1, *) x*20, y*20, sim(x,y)
    write(2, *) x*20, y*20, sim(x,y)
  end do
end do
close(1)
close(2)

! WEB
x_real=0
y_real=0
e0=a(50,50,height)
open(1,file='spider-net.txt')
do r=0, 10
  do alpha=0, 2*pi-pi/10, 2*pi/10
    x_real=100*r*cos(alpha)
    y_real=100*r*sin(alpha)
  
```

```

x=nint((x_real+1000)/20)
y=nint((y_real+1000)/20)
!sim(x,y) = a(x,y,height) + (e0-a(x,y,height))*0.8
e0=a(x,y,height)+(e0-a(x,y,height))*0.8
write(1, *) nint(x_real), nint(y_real), e0
print *, x_real, y_real
end do
end do
close(1)

! ARC
x_real=0
y_real=0
e0=a(50,50,height)
open(1, file='stonehenge.txt')
write(1, *) 0, 0, e0
do r=0, 10
  circumference=2*r*100*pi
  divisions=circumference/100
  do alpha=0, 2*pi-2*pi/divisions, 2*pi/divisions
    x_real=100*r*cos(alpha)
    y_real=100*r*sin(alpha)
    x=nint((x_real+1000)/20)
    y=nint((y_real+1000)/20)
    !sim(x,y) = a(x,y,height) + (e0-a(x,y,height))*0.8
    e0=a(x,y,height)+(e0-a(x,y,height))*0.8
    write(1, *) nint(x_real), nint(y_real), e0
    print *, x_real, y_real
  end do
end do
close(1)

end program diffusion

```

5.2 Deconvolution program in Fortran

```

program deconvolution
implicit none

```

```

integer :: i, j, stat
real rc, e0, conv
real t

rc=0.85
open(1, file='data.txt')
open(2, file='data_deconvoluted.txt')
read(1, *) i, j, e0
do
    read(1, *, iostat=stat) i, j, conv
    if (stat /= 0) exit
    write(2, *) i, j, ((conv - e0*rc)/(1-rc))
    e0=conv
end do
close(1)
close(2)

end program deconvolution

```

This document was created with the L^AT_EX 2 _{ε} document preparation package on a Debian GNU/Linux 9.x system, edited in Vim. Text and math typeset in Computer Modern. The diagrams were rendered with Gnuplot and L^AT_EX 2 _{ε} 's own renderer, Tikz. The sketches were drawn with CorelDraw X4 and Inkscape. With the exception of Figs. 2.1, 2.2, 2.3, 2.4A,C, 3.15A,B,D, all figures have been rendered / drawn / photographed by the author.